

Acta Technologica Agriculturae 2  
Nitra, Slovaca Universitas Agriculturae Nitriae, 2021, pp. 55–60

## DEVELOPMENT OF A PILOT SOIL-WATER BALANCE MODEL FOR DETERMINATION OF PROBABILITY OF A WORKING DAY FOR RICE HARVESTING

Mahdi KHANI\*, Seyyed Hossein PAYMAN, Nader PIRMORADIAN

University of Guilan, Rash, Iran

The probability of a working day is the ratio of workable days to the total available days in a working season for the intended operation. Soil moisture is the most important limiting factor in terms of rice harvesting. Therefore, to determine the PWD for this operation, a model was developed to estimate the soil moisture based on soil-water balance. To calibrate and validate the model, the soil moisture was monitored in the paddy field of the University of Guilan during the rice harvest seasons in 2017 and 2018. The calibration process was performed by applying a decreasing ratio, i.e. the senescence factor ( $\alpha$ ), at a daily evapotranspiration rate compared to that of previous day. At the validation stage, the simulated soil moisture contents were compared with measured values, which indicated a good model accuracy (NRMSE = 6.53%) of the soil moisture estimation. Therefore, this model can be used for the rice harvesting operation feasibility evaluation and PWD calculation.

**Keywords:** soil moisture; trafficability; evapotranspiration; agricultural planning

Accurate information on the time available for operations is essential for planning agricultural operations and determining the required working capacity of agricultural machinery. Each agricultural operation is usually limited to a specific timeframe, but factors such as adverse environmental conditions can cause the loss of days in the working season. The ratio of working days to total days during the working season is known as the probability of a working day (PWD). This parameter is used in calculation of minimum and optimum capacities of needed machines, and timeliness cost of operations. To determine the PWD or number of workdays, it is important to determine the feasibility of operations during a specific period. Therefore, the feasibility of operations is examined separately for each day and period. In rice harvesting, the ripening of rice grains determines the time for operation beginning. The end time is also determined by ear drying and increased seed fall. On certain days during this period, it is impossible to perform the harvest due to unsuitable conditions. Huang et al. (2017) identified harvest time as one of the most important factors in grain loss.

Factors that may prevent rice harvest include soil moisture and panicle moisture. Modern rice combine harvesters can harvest and thresh panicles with relatively high moisture content. Therefore, the only parameter considered to influence the feasibility of rice harvesting operations is soil moisture. In this regard, the harvester should be able to enter the field and move through the field easily; i.e., the field must be trafficable. Trafficability is the capacity of soil to support and withstand traffic with negligible soil structural damage and no adverse effects on crop yield (Rounsevell and Jones, 1993).

Moisture content at field capacity (Cooper et al., 1997; Simalenga and Have, 1992; Rutledge and McHardy, 1968) and plastic limit (Dexter and Bird, 2001) are the most common soil moisture thresholds used to examine the feasibility of operations. However, a certain limit cannot be specified for all conditions and soils, because the interaction between soil and machine depends on machine characteristics including machine mass (McPhee et al., 2020), and size and pressure of tire (Antille et al., 2013; Stevens et al., 2016), as well as soil properties including texture, organic matter content and bulk density. Carranza et al. (2019) stated that root growth can also affect soil trafficability. Therefore, the best way to determine the trafficability limit is experimental investigation.

The primary method to determine the PWD is to survey the real situation in order to directly examine the possibility of performance of operations for several years. Despite its high accuracy, this method is very costly and time-consuming, and the results can only be applied to the climate, soil, and particular crop under consideration.

The most common method is to estimate the conditions for assessing the feasibility of operations in the previous years. In this method, field conditions in the working season are estimated using the meteorological data and other required data from previous years. Then, the feasibility of operations is judged by comparing the estimated conditions and workability criteria. Soil moisture is one of the most important limiting factors in most agricultural operations. This parameter is estimated using soil-water balance models. This method has been used for tillage (Abdulsalam et al., 2017; Cooper et al., 1997; Khani et al., 2011; Simalenga and Have, 1992), as well as planting and harvesting of corn (Jahun et al., 2014).

**Contact address:** Mahdi Khani, University of Guilan, Faculty of Agricultural Sciences, Department of Agricultural Mechanization Engineering, Rash, Iran; e-mail: [mahdikhani@guilan.ac.ir](mailto:mahdikhani@guilan.ac.ir)

World rice production amounts to approx. 618 million tons per year (Rahimi-Ajdadi et al., 2018), but no research has investigated the workdays of the rice crop. In rice farming, harvesting is the most sensitive period in terms of operation time. Improper knowledge about the available time leads to inappropriate timing of operations and considerable economic losses. Existing soil-water balance models are generally developed to estimate the water requirement of plants during the growing season and are not suitable for estimation of the soil moisture during harvest season. In particular, the gradual senescence of rice plants can be a source of error in the evapotranspiration calculation. Even after developing a suitable model, it should be calibrated to improve the estimation accuracy. In this study, a model was developed for estimating the soil moisture during the rice harvesting period and calculating the PWD by comparing the moisture content estimated with a trafficability limit. Then, the model efficiency and the reliability of its output data were evaluated by a validation test.

**Material and methods**

**Model structure**

According to the mass conservation law, the amount of water entering the soil profile is equal to the algebraic sum of released and stored water. The moisture output and input to the soil profile can be calculated using meteorological and soil properties data. In this manner, new moisture content can be attributed to the soil by adding the initial soil moisture. This cycle continues repeatedly, and soil moisture is determined throughout the days under consideration. The general structure of the model is as follows:

$$\theta_{i+1} = \theta_i + P_i - D_i - R_i - ET_i \quad (1)$$

where:

- $\theta_i$  – soil water content at the beginning of a given time step
- $P_i$  – rainfall (or irrigation)
- $D_i$  – drainage
- $R_i$  – runoff
- $ET_i$  – evapotranspiration at the given time step

$\theta_{i+1}$  – soil water content at the end of this time step or at the beginning of the next time step

Appropriate workdays are determined after calculating the soil moisture and comparing it with the

moisture limit. The PWD for a period is obtained by dividing the number of workdays by total amount of period days. The general model flowchart is shown in Fig. 1.

To calculate the evapotranspiration, this parameter is first obtained for the

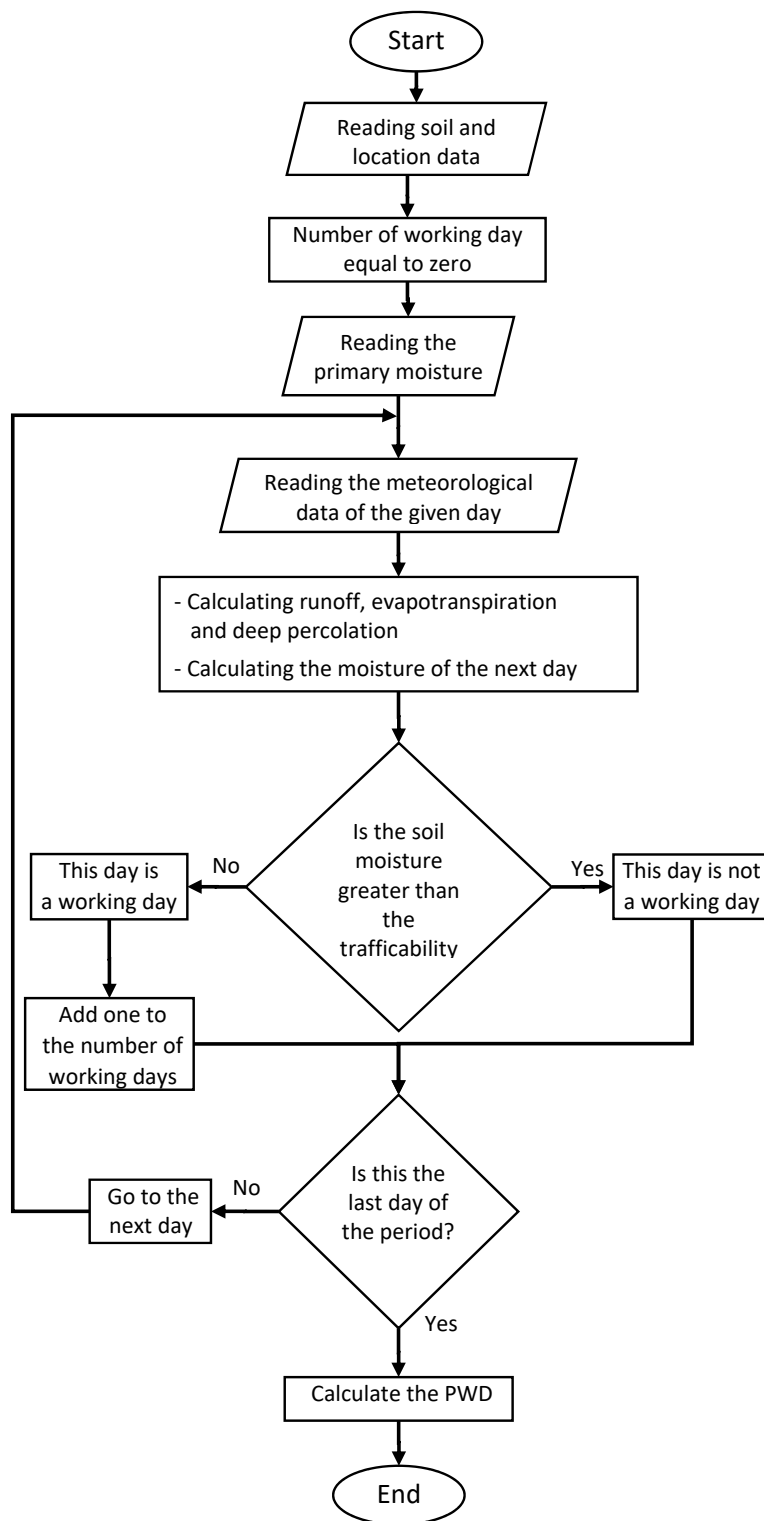


Fig. 1 General model flowchart

reference plant (grass) under standard conditions using the Penman-Monteith equation (Allen et al., 1998) (Eq. 2):

$$ET_0 = \frac{0.408\Delta(R_n - G) + \gamma \frac{C_n}{T + 273} u_2 (e_s - e_a)}{\Delta + \gamma(1 + C_d u_2)} \quad (2)$$

where:

$ET_0$  – reference evapotranspiration (mm·day<sup>-1</sup> for daily time step)

$R_n$  – net radiation at the crop surface (MJ·m<sup>-2</sup>·day<sup>-1</sup>)

$G$  – soil heat flux density (MJ·m<sup>-2</sup>·day<sup>-1</sup>)

$T$  – mean daily air temperature at 2 m height (°C)

$u_2$  – wind speed at 2 m height (m·s<sup>-1</sup>)

$e_s$  – saturation vapour pressure (kPa)

$e_a$  – actual vapour pressure (kPa)

$e_s - e_a$  – saturation vapour pressure deficit (kPa)

$\Delta$  – slope vapour pressure curve (kPa·°C<sup>-1</sup>)

$\gamma$  – psychrometric constant (kPa·°C<sup>-1</sup>)  
the  $C_n$  and  $C_d$  constants for daily values are 900 and 0.34, respectively

Information on the calculation of parameters of this equation is given in Allen et al. (1998). To obtain the potential evapotranspiration ( $ET_p$ ) of the plant under consideration, the reference evapotranspiration ( $ET_0$ ) must be multiplied by the corresponding crop coefficient ( $K_c$ ) (Eq. 3). The value of this coefficient is determined based on the type of plant and its growth stage. A value of 0.6 was considered for this coefficient, since rice is in the late stage of growth at the time of harvest (Allen et al., 1998).

$$ET_p = K_c \cdot ET_0 \quad (3)$$

As long as soil moisture is sufficient, atmospheric parameters determine the evapotranspiration rate. When the plant starts to lose access to the readily available water, the actual amount of evapotranspiration will be less than its potential value. To convert  $ET_p$  into actual evapotranspiration ( $ET_a$ ), a correction factor – the stress coefficient ( $K_s$ ) – is used:

$$ET_a = K_s \cdot ET_p \quad (4)$$

The stress factor is obtained as follows:

$$K_s = \frac{TAW - D_r}{TAW - RAW} \quad (5)$$

where:

$TAW$  – total available water in the root zone (obtained by multiplying the difference in moisture content at the field capacity (FC) and permanent wilting point (PWP) in the effective root depth)

$RAW$  – readily available water, which is considered to be 0.4 (Allen et al., 1998) of  $TAW$  due to the shallow root of rice in the paddy field

$D_r$  – root zone depletion. These parameters are expressed in millimetres of water. The Eq. 5 is applicable after the depletion of  $RAW$ ; prior to this point, the  $K_s$  is assumed to be equal to 1

The runoff was calculated using the curve number (CN) method (Eq. 6) introduced by the US Soil Conservation Service (SCS, 1972):

$$R = \frac{(P - 0.2S)^2}{P - 0.8S} \quad \text{for } P \geq 0.2S \quad (6)$$

where:

$R$  – runoff (mm)

$P$  – precipitation (mm)

$$S = \frac{25,400}{CN} - 254 \quad (7)$$

where:

$S$  – potential maximum retention (mm)

The  $CN$  value (i.e., 0 to 100) depends on soil characteristics, crop cover, and hydrological conditions.

When the soil moisture in surface layer exceeds the FC, moisture transfer to soil lower layers occurs due to deep percolation. Due to the presence of hardpan, a constant rate is considered for deep percolation in paddy soils. In this model, the percolation rate is considered a model input that can be obtained from different references according to the soil texture, e.g. Razavipour et al. (2005) measured this parameter in different types of soils in the Guilan province. The rate of deep percolation in this study was determined based on their work.

Subsequently, the soil moisture can be obtained by having the initial soil moisture content using the soil-water balance equation. This process continues from the beginning to the end of the simulation, and soil moisture is calculated throughout the days of the considered period. The trafficability limit as the model input is determined by the user. If soil moisture is less than the trafficability limit, that day will be considered as a workable day; otherwise, the operation is not possible. In this study, the moisture content, in which the farmer could bring a combine harvester to the field for the first time (44.8 vol.% for the validation field) and start harvesting, was considered to be a trafficability limit.

The model was coded in VBA (Visual Basic for Applications) – the MS-Office suite programming language. Input data are introduced into the Excel spreadsheet and output data are also displayed in the same software.

### Model calibration

The time period considered in this study is the last days of rice plant lifetime when the plant evapotranspiration capacity decreases due to the leaf senescence onset. Since the effects of plant leaf senescence on its transpiration have not been well discussed by scientists, this issue was taken into account in model calibration process. To calibrate the model, a comparison was made between simulated and measured soil moisture values.

In this regard, firstly, the process of soil moisture changes in rice harvest season was simulated using the model for a plot of land at the Faculty of Agricultural Sciences, University of Guilan. Next, soil samples were collected to determine the soil characteristics, such as texture, bulk density, and moisture content at FC, and PWP.

Meteorological data in 2017 were obtained from the Rasht Agricultural Synoptic Station in the vicinity of the field under study. The soil bulk density, moisture content at FC, and soil texture were measured by a sampling cylinder, a pressure plate apparatus, and hydrometer method, respectively. The moisture content at PWP was estimated by the percentage of soil particles and bulk density using the Rosetta software.

The rice (Var. Hashemi) was harvested on August 20. On July 24, the first moisture data were collected in the field to determine the initial moisture content at the stimulation onset.

The simulated results and measured data were compared statistically using normalized root-mean-square error (NRMSE).

At the ripening period onset and with senescence of certain plant leaves, its transpiration capacity and subsequently the field potential for evapotranspiration decrease each day relative to the previous day by a coefficient. To incorporate this effect in the model, daily  $ET_p$  was calculated as follows:

$$ET_{pr}(i) = ET_p(i) \times (1 - \alpha)^{i-1} \tag{8}$$

where:

- $ET_p(i)$  – potential evapotranspiration on the  $i^{th}$  day regardless of plant senescence
- $ET_{pr}(i)$  – potential evapotranspiration on the  $i^{th}$  day taking into account the plant senescence
- $i$  – number of given days
- $\alpha$  – ratio of decreasing of evapotranspiration each day to its value in the previous day ( $0 \leq \alpha \leq 0.1$ )

Therefore, rather than obtaining  $ET_a$  directly from  $ET_{pr}$ , the effects of plant senescence are first considered on  $ET_{pr}$ , followed by obtaining  $ET_a$  (which depends on soil moisture conditions) from the modified potential evapotranspiration ( $ET_{pr}$ ).

Different values of  $\alpha$  (1–10%) were considered for calibration. Subsequently, the  $\alpha$  value showing the highest agreement between the simulated and measured data (minimum NRMSE value) was considered an appropriate value of plant senescence factor for the studied conditions.

### Model validation

The model performance should be ensured for practical use. To this end, a validation test was also performed to compare simulation results with measured data at a time and location different from the calibration test. The test was carried out at another field of the University of Guilan during the rice harvest period in 2018. For these purposes, five samples per day were collected as experimental replicates. The samples were taken only from the depth of 15 cm. Sampling started on 25 July 2018 and continued until 24 August 2018.

To statistically compare the results and determine the model inputs, the same procedure used in calibration test was also employed in this test. The default senescence factor ( $\alpha$ ) applied to this test was determined according to the calibration test results.

## Results and discussion

### Soil test

The soil texture test results and measurement of its hydraulic parameters for the studied fields during calibration and validation steps are shown in Table 1.

**Table 1** Soil properties of fields used in the calibration and validation tests

Validation field	Calibration field	Soil properties
57.2	45.2	clay (%)
30.2	46.3	silt (%)
12.6	8.5	sand (%)
clay	silty clay	soil texture
1.5	1.5	deep percolation rate (mm·day <sup>-1</sup> )
1.12	1.13	bulk density (g·cm <sup>-3</sup> )
36.7	37.6	gravimetric moisture at FC (%)
19.5	16.4	gravimetric moisture at PWP (%)

### Calibration

Correlation values between the estimated and measured moisture for different values of the senescence factor during calibration test are shown in Fig. 2. Taking into account that the senescence factor yields a more reasonable estimate of the evapotranspiration rate as the most important component of soil-water balance, it improves the correlation between the simulated and measured data. As shown in Fig. 2, the moisture estimation accuracy enhances with increasing  $\alpha$  (senescence factor) until the highest correlation is achieved between the measured and estimated data. Excessive increase in  $\alpha$  leads to the underestimation of evapotranspiration and reduces the moisture estimation quality. The highest agreement (NRMSE = 5.38%) between simulated and measured data was obtained with an  $\alpha$  of 0.05. As a result, an  $\alpha$  of 5% was selected for the basis of this model in order to correct the evapotranspiration calculation and estimate the soil moisture content. In the following conduction, the validation test and PWD calculations were performed accordingly.

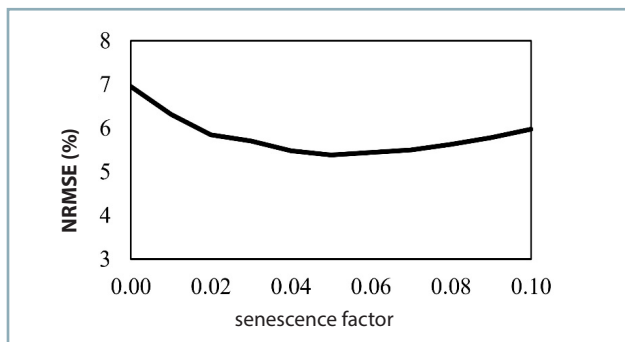


**Fig. 2** NRMSE values obtained by taking into account different values for the senescence factor ( $\alpha$ ) in the calibration test

### Validation

The validation test (with an  $\alpha$  of 0.05) yielded an NRMSE value of 6.53%, indicating the acceptable model performance in estimating the soil moisture.

Fig. 3 shows the trend of moisture changes in simulated and measured conditions in non-calibrated (without senescence factor) and calibrated modes.

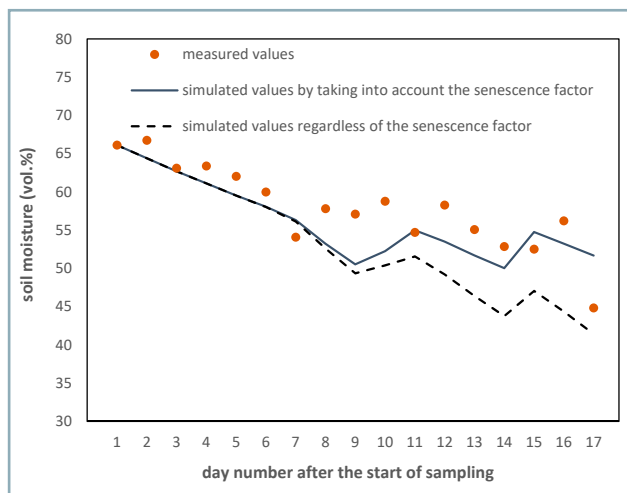


**Fig. 3** Comparison of simulated and measured moisture in the validation test

According to Fig. 3, the simulated and measured data are much consistent at the beginning of period, but the difference between results grows in the final days. The main reason for this seems to be the senescence of certain plant leaves and decreased transpiration. However, evaporation from the soil surface was not affected by this process.

The model calibration and considerations of the dropped leaf transpiration capacity due to leaf senescence led to an increased agreement between the measured and simulated data, particularly in the final days prior to rice harvest. There are several moisture changes with upward trend due to rainfall on certain days.

Considering the different times and locations of calibration and validation tests, this model can be also used in other rice fields with similar conditions to those of these tests, and there is no need to repeat the calibration test for each field.

A good model performance in validation test due to the modifications in calibration test does not mean a constant senescence factor under all conditions. The calibration test must be rerun if the model is to be used for different climates and possibly different rice varieties. It can, however, be deduced that it is possible to use the senescence factor obtained here to accurately calculate the evapotranspiration of rice plant and soil moisture. As a result, a realistic estimate of the feasibility of rice harvesting operations can be obtained under majority of conditions similar to those presented here.

Instead of comparing the measured and simulated soil moistures, Rotz and Harrigan (2005) and Yousif et al. (2014) compared the number of observed workdays with the estimated ones to evaluate their models.

The advantage of this method is that it simultaneously includes the accuracy of moisture estimation and the accuracy of determining the moisture threshold. However, it may lead to a misunderstanding about the model reliability.

There may be a significant difference between the simulated and actual soil moisture on a given day, but due to the selected moisture threshold, the model simulation result and field observations are the same in terms of operation feasibility.

Furthermore, soil moisture underestimation in particular parts of a working period can be offset by overestimation in other parts of the period, since this method takes into account only the total number of working days in the entire working period, suggesting that this method can exaggerate the accuracy of the model.

### Conclusion

The model developed has an acceptable performance to determine the PWD. Therefore, it can be used in many rice fields that do not significantly differ from the studied field in terms of climatic conditions. It is recommended to conduct further studies on the climate change impact on the time available for operations. The methods proposed for PWD determination implicitly assume that average weather conditions in forthcoming years are similar to those of previous years. Nonetheless, climate change caused by greenhouse gas emissions may affect the accuracy of calculations for the number of workdays. However, certain efforts have been made to investigate the effect of climate change on the PWD (Cooper et al., 1997). Nevertheless, more state-of-the-art and extensive studies are required to determine the degree of changes and their effects on available working time.

It is recommended to study the plant senescence process using more accurate and generalizable methods. The plant dropped transpiration in the final period of plant establishment can be estimated more accurately if more comprehensive and accurate equations are obtained from the yellowing process of plant leaves. In such a manner, it would be possible to expand the model application scope.

With yellowing of the rice plant, the field soil drying process drastically decreases through evapotranspiration. Accordingly, in years with concerns about limited available workdays, field planning should be in such a way that the last irrigation can be done earlier. In this case, the evaporative capacity of the plant is used before drying its leaves, thereby accelerating the process of soil moisture reduction.

Models for PWD determination are developed for a particular plant and operation and are rarely used for other conditions. Therefore, the development of a comprehensive model that can estimate the PWD in majority of conditions can be one of the primary objectives of future studies. In this regard, it is recommended to develop an efficient model that can work for different plants (with or without hardpan), bare soil, row crops, etc.

### Acknowledgements

The authors would like to acknowledge the Faculty of Agricultural Science, University of Guilan, for their support and contribution to this study.

## References

- ABDULSALAM, M. – ISIAKA, M. – DALHA, I. B. – DALHAT, M. K. 2017. Performance evaluation of computer-based suitable field workdays model. In *Bayero Journal of Engineering and Technology*, vol. 12, no. 1, pp. 52–66.
- ALLEN, R. G. – PEREIRA, L. S. – RAES, D. – SMITH, M. 1998. Crop evapotranspiration: Guidelines for computing crop water requirements. In *FAO Irrigation and Drainage Paper No 56*. Food and Agriculture Organization, Land and Water. Rome, Italy.
- ANTILLE, D. L. – ANDSORGE, D. – DRESSER, M. L. – GODWIN, R. J. 2013. Soil displacement and soil bulk density changes as affected by tire size. In *Transactions of the ASABE*, vol. 56, no. 5, pp. 1683–1693.
- CARRANZA, C. – BENNINGA, H. J. – VELDE, R. V. D. – PLOEG, M. V. D. 2019. Monitoring agricultural field trafficability using Sentinel-1. In *Agricultural Water Management*, vol. 224, 105698.
- COOPER, G. – McGECHAN, M. B. – VINTEN, A. J. A. 1997. The influence of a changed climate on soil workability and available workdays in Scotland. In *Journal of Agricultural Engineering Research*, vol. 68, no. 3, pp. 253–269.
- DEXTER, A. R. – BIRD, N. R. A. 2001. Methods for predicting the optimum and the range of soil water contents for tillage based on the water retention curve. In *Soil & Tillage Research*, vol. 57, pp. 203–212.
- HUANG, T. – LI, B. – SHEN, D. – CAO, J. – MAO, B. 2017. Analysis of the grain loss in harvest based on logistic regression. In *Procedia Computer Science*, vol. 122, pp. 698–705.
- JAHUN, B. G. – IYA, S. A. – ABUBAKAR, Y. 2014. Estimation of suitable field workday of planting and harvesting operations of maize production in Bauchi State Nigeria. In *European Journal of Food Science and Technology*, vol. 2, no. 1, pp. 8–18.
- KHANI, M. – KEYHANI, A. – PARSINEJAD, M. – ALIMARDANI, R. 2011. Verification and sensitivity analysis of a model for determination of probability of a working day for tillage. In *International Agrophysics*, vol. 25, no. 1, pp. 27–35.
- McPHEE, J. E. – ANTILLE, D. L. – TULLBERG, J. N. – DOYLE, R. B. – BOERSMA, M. 2020. Managing soil compaction – A choice of low-mass autonomous vehicles or controlled traffic? In *Biosystems Engineering*, vol. 195, pp. 227–241.
- RAHIMI-AJDADI, F. – ASLI-ARDEH, A. A. E. – AHMADI-ARA, A. 2018. Effect of varying parboiling conditions on head rice yield for common paddy varieties in Iran. In *Acta Technologica Agriculturae*, vol. 21, no. 1, pp. 1–7.
- RAZAVIPOUR, T. – YAZDANI, M. R. – MOUSAVI, S. F. 2005. Measuring water deep percolation in different soil textures of paddy fields in the growing season of rice. In *Journal of Agricultural Natural Resources Science of Khazar*, vol. 3, no. 4, pp. 1–9. (in Farsi with English abstract)
- ROTZ, C. A. – HARRIGAN, T. M. 2005. Predicting suitable days for field machinery operations in a whole farm simulation. In *Applied Engineering in Agriculture*, vol. 21, no. 4, pp. 563–571.
- ROUNSEVELL, M. D. A. – JONES, R. J. A. 1993. A soil and agroclimatic model for estimating machinery workdays: the basic model and climatic sensitivity. In *Soil & Tillage Research*, vol. 26, no. 3, pp. 179–191.
- RUTLEDGE, P. L. – McHARDY, F. V. 1968. The influence of the weather on field tractability in Alberta. In *Canadian Agricultural Engineering*, vol. 10, no. 2, pp. 70–73.
- SIMALENGA, T. E. – HAVE, H. 1992. Estimation of soil tillage workdays in a semi-arid area. In *Journal of Agricultural Engineering Research*, vol. 51, pp. 81–89.
- STEVENS, M. T. – MCKINDLEY, G. B. – VAHEDIFAR, F. 2016. A comparison of ground vehicle mobility analysis based on soil moisture time series datasets from WindSat, LIS, and *in situ* sensors. In *Journal of Terramechanics*, vol. 65, pp. 49–59.
- USDA-SCS. 1972. *Soil Conservation Service National Engineering Handbook*. United States Department of Agriculture.
- YOUSIF, A. E. A. – DAHAB, M. H. – RAMLAWI, H. R. EI. – FARID ELTOUM, A. E. 2014. A computer system for prediction of farm machinery workable days in rain-fed areas of Sudan. In *International Journal of Engineering & Scientific Research*, vol. 2, no. 11, pp. 17–23.



Acta Technologica Agriculturae 2  
Nitra, Slovaca Universitas Agriculturae Nitriae, 2021, pp. 61–66

## A 4-DOF SCARA ROBOTIC ARM FOR VARIOUS FARM APPLICATIONS: DESIGNING, KINEMATIC MODELLING, AND PARAMETERIZATION

Ali ROSHANIANFARD<sup>1\*</sup>, Du MENGMEG<sup>2</sup>, Samira NEMATZADEH<sup>1</sup>

<sup>1</sup>University of Mohaghegh Ardabili, Ardabil, Iran

<sup>2</sup>Henan University of Science and Technology, Luoyang, Henan, China

The agriculture industry has faced various challenges nowadays. This research is the first part of a project that presents the designing process, kinematic modelling, and parameterization of a 4-DOF SCARA-type robotic arm specifically designed for work in an agricultural field in terms of seeding, watering, fertilizing, weeding, harvesting, and transporting. The designing of parameters, such as optimum degrees of freedom and component configuration, was done. The kinematic model was calculated using the Denavit-Hartenberg method. The structure of robot was developed for inertia reduction, smooth motion, and torque minimization. The results show that the working space, maximum front access, and side access of developed robotic arm were 11.4 m<sup>2</sup>, 2.9 m, and 2.4 m, respectively. The results indicate that the robot has sufficient surface coverage for defined farm work.

**Keywords:** smart; crop; robot; tractor; autonomous

The future will be challenge-full for the agriculture industry. The world population is estimated to reach 9.7 billion by 2050; therefore, the food quality and quantity should be doubled (FAO, 2009, 2017). Natural disasters and global warming will influence the total factor productivity of the agriculture industry. The water shortage and pollution, same as rainfall pattern change, will limit the watering methods (Oktem, 2008). The labour shortage will be one of the critical issues worldwide soon (Marinoudi et al., 2019). Less than one percent of the US population will deal with farming by 2050 (Accenture, 2017). The average age of farmers reached 66, 58, and 53 years in Japan, the USA, and Iran, respectively. Farmers also struggle with labour employment costs, including insurance, taxes, and salary (Dorward, 2013).

Digital farming as an interdisciplinary field between robotic and agriculture sciences has many solutions for the mentioned concerns. The digital farming comprises two main parts: precision farming (measuring parameters for data generation), and smart farming (using the generated data for different applications). Many valuable studies were done in this field, i.e. social science on digital and smart agriculture (Klerkx et al., 2019), digital innovation in smart farming (Ayre et al., 2019), innovation in digital farming (Bronson, 2019), and digital farming and ICT (Shibusawa, 2018). It is obvious that farm robots will assist future farmers in many aspects. Multiple researchers have focused on developing a new robotic system to plant, protect, and harvest a variety of crops, such as apple (Lv et al., 2019), orange (Garner et al., 2006), tomato (Li et al., 2019), strawberry (Xiong et al., 2019; Aliasgarian et al., 2015), kiwifruit (Williams et al., 2019), grape (Luo et al., 2018), heavy-weight crops (Roshanianfard et al., 2018;

Kamata et al., 2018; Roshanianfard and Noguchi, 2017, 2018b; Roshanianfard, 2018), and pumpkin (Roshanianfard and Noguchi, 2016, 2018a).

The manipulation system and robotic arm as the main component of a robotic system play a significant role in the smart operation. Most of the developed systems were installed on a prototype platform which meets many limitations in real farms. Several researchers installed controlling systems on commercialized platforms, such as tractors (Wang and Noguchi, 2019), combines (Zhang et al., 2013), boats (Liu et al., 2017), all-terrain-vehicles, utility vehicles (UTVs), and drones for farm applications (Roshanianfard et al., 2019; Kashkarov et al., 2018). However, the development of robotic arms and manipulation systems for the aforementioned platforms still requires extensive research. Furthermore, it is worth mentioning that the majority of commercialized robotic arms have not been developed for agriculture in dusty, dirty, and humid environments. They require indoor and isolated working environment.

In this regard, the development of a specifically designed robotic arm, which would be installed on the autonomous tractors working in real agricultural field is a new area (Cviklovič et al., 2016). The research objective is to design a robotic arm that can handle the unpredictable farm situation such as rain, wind, dust, mud, and vibration with an optimized number of degrees of freedom (DOF). Therefore, it can be concluded that the novelty of designed robotic arm is in:

1. its adaptability to real agricultural farm conditions because of its specifically designed components (joints, links, and controlling unit), resilient against vibration, dust, and humidity;

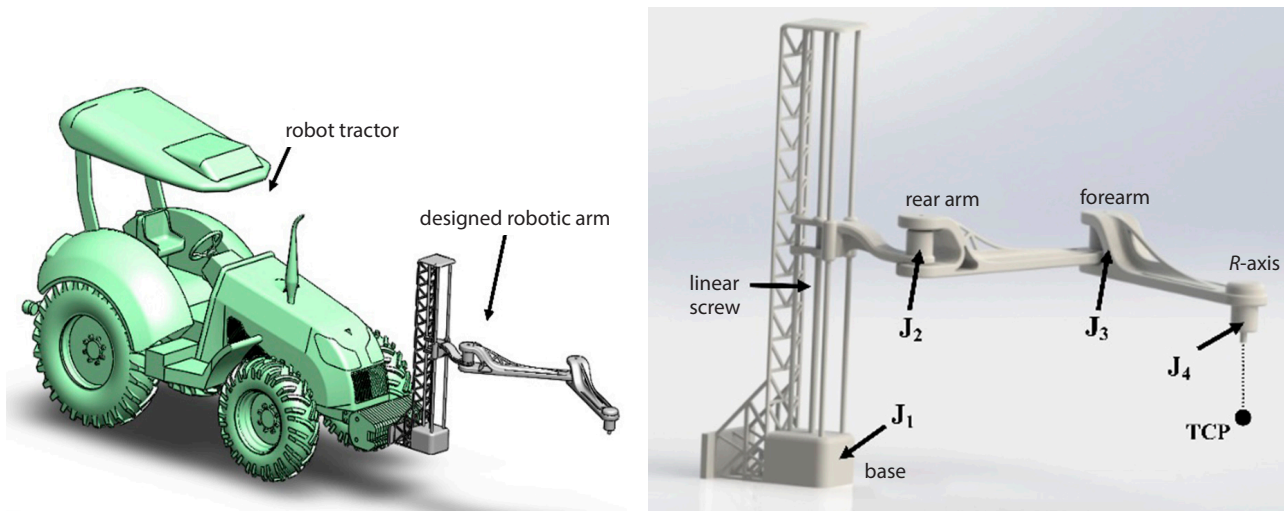


Fig. 1 Robotic system for real agricultural field (left), and designed robotic arm (right)

2. specifically simplified quick algorithm for collaboration with an autonomous tractor with minimum delay;
3. its sufficient payload per weight compared with industrial robotic arms.

### Material and methods

#### Designed system

Based on the mentioned concerns in farming, a 4-DOF SCARA type robotic arm was designed, as shown in Fig. 1. The 3D CAD design was done using Solidworks (Dassault Systèmes, France). First, several configurations and structures of robotic arms were searched and evaluated from different points of view, including the number of joints, working space, access length, orientation of endpoint, and strength of elements. Multiple simulations were performed in order to reach an optimized structure. As the objective of this research was developing a robotic arm for farm use, a vertical orientation through the Z-axis along the front and lateral access was required. The simplicity of orientation can make the structure manufacturing process and algorithm development much easier. The designed robotic arm is equipped with a linear screw to move in the Z-direction. This axis will be used when the robot transports a crop or when it wants to change the structure height. The robotic arm also has three joints for the rear arm, forearm, and rotation of end-effector (EE). These

three joints move the EE in the X- and Y-directions. The material applied for the body was aluminium (AL5052), because the light aluminium alloy used shows good weldability by gas, arc, and resistance. The structure design and all simulations were conducted for 20 kg of payload and 1.5 of the factor of safety (FOS).

#### Configuration and coordination

The agricultural farms and horticultural environments are complicated, unstructured, and dirty environments. This is especially true for robotic arms with multiple sensitive components, such as servo motors, amplifiers, cables, and control units. Because of that, it is important to develop a robotic arm with simple and repairable components. Moreover, it is important to shield all electronic and

electrical parts; design stainless joint and component; and use specifically selected ball bearing and bearings. This simplicity in structure makes the algorithm development much easier. Therefore, after DOF selection process, a SCARA type robotic arm with a 4-DOF was designed, as shown in Fig. 1. This robotic arm has 4 joints:  $J_1, J_2, J_3, J_4$ . Each joint was designed for a different task. The  $J_1$ , connected to a long screw, can control the position of endpoint in Z-axis. The  $J_2$  and  $J_3$  move the rear arm and forearm, respectively, and control the endpoint in X- and Y-directions. Ultimately, the  $J_4$  was set specifically for rotating the attached EE. The designed robot can manoeuvre in a 3D environment smoothly and it can perform the majority of agriculture operations, i.e. seeding, watering, fertilizing, weeding, and harvesting, etc. The coordination of joints and

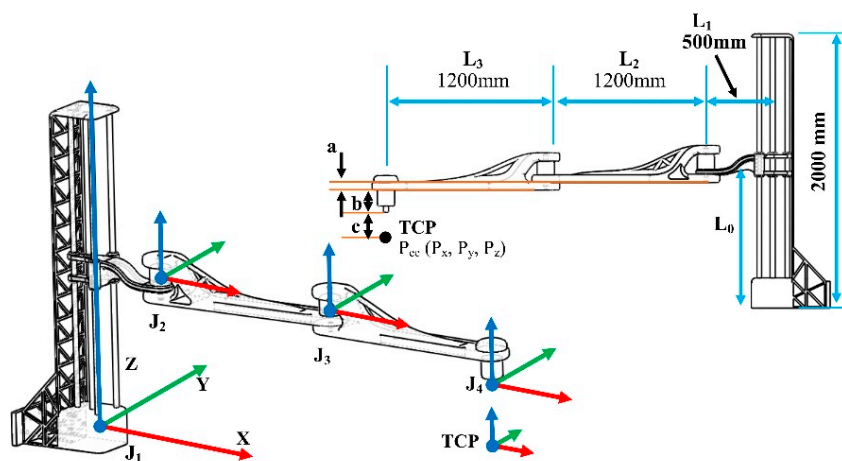


Fig. 2 Coordination of robotic arm (left), parameter description (right)

home coordination were adjusted based on the right-handed coordinate system, as shown in Fig. 2. The rotations in  $X$ -,  $Y$ -, and  $Z$ -direction were named roll ( $r_x$ ), pitch ( $r_y$ ), and yaw ( $r_z$ ), respectively.

### Kinematics of robot

#### Forward kinematics

After numerous calculations using different methods, the Denavit-Hartenberg (D-H) method was selected because of its simplicity and quick response. Using the D-H method allows for setting the rotation angles  $J_1, J_2, J_3, J_4$  and tool offsets as input; and for obtaining a position in  $X$ -,  $Y$ -, and  $Z$ -directions ( $P_x, P_y$ , and  $P_z$ , respectively), orientation ( $r_x, r_y, r_z$ ) of tool centre point (TCP) and angle of each joint as outputs. As the motion in the  $Z$ -axis depends only on the rotation of  $J_1$ , the  $L_o$  can be calculated as follows:

$$L_o = l \left( n + \frac{\theta_1}{360} \right) = l \cdot n + \beta \cdot \theta_1 \quad (1)$$

$$n = \left\lfloor \frac{P_z}{l} \right\rfloor \text{ and } \beta = \frac{l}{360} \quad (2)$$

where:

$L_o$  – length of displacement in the  $Z$ -direction

$l$  – screw lead

$n$  – number of  $J_1$  rotations

$\theta_i$  – joint- $i$  rotation angle

Then:

$$P_z = l \left( n + \frac{\theta_1}{360} \right) \quad (3)$$

Therefore, the position of TCP in the 3D environment can be resulted as:

$$P_x = L_1 + L_2 \cos \theta_2 + L_3 \cos (\theta_2 + \theta_3) \quad (4)$$

$$P_y = L_2 \sin \theta_2 + L_3 \sin (\theta_2 + \theta_3) \quad (5)$$

$$P_z = L_o - a - b - c \quad (6)$$

where:

$P_i$  – position of endpoint in the  $i$ -direction

$a, b, c$  – offset between the  $J_2$  and  $J_3$ , the  $J_3$  and  $J_4$ , and the  $J_4$  and EE

$\theta_n$  – angle of joint- $n$ . The rest of the parameters is illustrated in Fig. 2

#### Inverse kinematics

The forward kinematic calculation is a progressive task that is performed to find the position of EE from a variation of joint angles. To develop a robotic arm, one of the time-consuming and hard tasks is to find the desired joint angle if the EE's position is input. This section presents the inverse kinematics calculation of designed robotic arm.

Let set the position and orientation in the  $X$ -,  $Y$ -, and  $Z$ -directions as  $P_x, P_y$ , and  $P_z$ , respectively, and  $r_x, r_y$ , and  $r_z$  of TCP as inputs, and rotation angle of joints  $J_1, J_2, J_3$ , and  $J_4$ , and tool

offsets as outputs. Based on Eqs 4–6, it is possible to calculate each angle continuously. The  $\theta_1$  is calculable using Eq. 6:

$$\theta_1 = \left( \frac{P_z + a + b + c}{\beta} \right) - 2n\pi = (P_z - a - b - c) \cdot \left( \frac{2\pi}{l} \right) - l \cdot n \quad (7)$$

To calculate the  $\theta_3$  by means of Eqs 4 and 5, there is:

$$L_2 \cos \theta_2 + L_3 \cos (\theta_2 + \theta_3) = P_x - L_1 = A \quad (8)$$

$$L_2 \sin \theta_2 + L_3 \sin (\theta_2 + \theta_3) = P_y = B \quad (9)$$

By (Eq. 4)<sup>2</sup> + (Eq. 5)<sup>2</sup>, then:

$$(L_2 \cos \theta_2 + L_3 \cos (\theta_2 + \theta_3))^2 + (L_2 \sin \theta_2 + L_3 \sin (\theta_2 + \theta_3))^2 = A^2 + B^2 \quad (10)$$

Subsequently:

$$\cos \theta_3 = \frac{A^2 + B^2 - L_2^2 - L_3^2}{2L_2L_3} \quad (11)$$

From Eq. 11:

$$\sin \theta_3 = \sqrt{1 - \left( \frac{A^2 + B^2 - L_2^2 - L_3^2}{2L_2L_3} \right)^2} \quad (12)$$

Using Eqs 11 and 12:

$$\theta_3 = \arctan 2 \left( \pm \sqrt{1 - \left( \frac{A^2 + B^2 - L_2^2 - L_3^2}{2L_2L_3} \right)^2} \cdot \frac{A^2 + B^2 - L_2^2 - L_3^2}{2L_2L_3} \right) \quad (13)$$

To calculate  $\theta_2$  by means of  $\cos \theta_2 \cdot$  Eq. 8 +  $\sin \theta_2 \cdot$  Eq. 9, there is:

$$A \cdot \cos \theta_2 + B \cdot \sin \theta_2 = L_2 + L_3 \cdot \cos \theta_3 \quad (14)$$

Using  $-\sin \theta_2 \cdot$  Eq. 8 +  $\cos \theta_2 \cdot$  Eq. 9, there is:

$$-A \cdot \sin \theta_2 + B \cdot \cos \theta_2 = L_3 \cdot \sin \theta_3 \quad (15)$$

Using  $A \cdot$  Eq. 15 +  $B \cdot$  Eq. 16, there is:

$$\cos \theta_2 = \frac{A(L_2 + L_3 \cdot \cos \theta_3) + B \cdot L_3 \cdot \sin \theta_3}{A^2 + B^2} \quad (16)$$

From Eq. 16:

$$\sin \theta_2 = \pm \sqrt{1 - \left( \frac{A(L_2 + L_3 \cdot \cos \theta_3) + B \cdot L_3 \cdot \sin \theta_3}{A^2 + B^2} \right)^2} \quad (17)$$

Since the range of rear arm is  $(-90^\circ, +90^\circ)$ , then the  $\cos \theta_2$  can be calculated using Eqs 17 and 18:

$$\theta_2 = \arctan 2 \left( \sqrt{1 - \left( \frac{A(L_2 + L_3 \cdot \cos \theta_3) + B \cdot L_3 \cdot \sin \theta_3}{A^2 + B^2} \right)^2}, \frac{A(L_2 + L_3 \cdot \cos \theta_3) + B \cdot L_3 \cdot \sin \theta_3}{A^2 + B^2} \right) \text{ when } P_y \geq 0 \quad (18)$$

$$\theta_2 = \arctan 2 \left( \sqrt{1 - \left( \frac{A(L_2 + L_3 \cdot \cos \theta_3) + B \cdot L_3 \cdot \sin \theta_3}{A^2 + B^2} \right)^2}, \frac{A(L_2 + L_3 \cdot \cos \theta_3) + B \cdot L_3 \cdot \sin \theta_3}{A^2 + B^2} \right) \text{ when } P_y < 0$$

The orientation of EE is always toward the Z-direction, and the angle of  $J_4$  does not affect the orientation of TCP. It can only affect the rotation of EE during grasping.

## Results and discussion

### DOF selection and economic optimization

Roshanianfard et al. (2020) presented a method for finding an optimized number of DOF for a robotic arm. Based on that methodology, it is necessary to evaluate an invariant structure (with constant main parameters) under different conditions. For this robot, the overall length of links ( $L = \sum_{i=0}^n L_i = 6a$ ), and the height of the installation position ( $h = 1.5a$ ) were considered constant (Fig. 3). At constant  $L$  and  $h$ , the number of joints, type of joints, and DOF were varied, and the results were compared, as shown in Fig. 4. The  $a = 20$  cm and all parameters were simplified based on this unit. All ratios were adjusted based on the designed robotic arm parameters. The length of the main link was  $6a$ , which was equally divided in order to reach the desired n-DOF.

The aim was the simulation and comparison of workspace index ( $I_v = \frac{V_n}{a^3}$ ), harvesting surface index ( $I_s = \frac{S_n}{a^2}$ ), minimum front access ( $FA_{min}$ ), and height length ( $HL$ ). As shown in Fig. 4, the workspace of 1-DOF and 2-DOF was zero, because this DOF could move at Fig. 5, the  $I_v$ ,  $I_s$ , and  $HL$  were increased when the DOF increased from 3 to 5, and the  $FA_{min}$  decreased. The  $HL$  of 3-DOF was less than required. This parameter increased between 4-DOF and 5-DOF, making the 4- and 5-DOF suitable in terms of physical point of view.

The economic and energy aspects of different DOF were the same as presented by Roshanianfard et al. (2019) research (Fig. 6). However, this evaluation took into account different expense sources, i.e. actuating cost, material cost, manufacturing expenses, mechanical parts, electronic component prices, and energy consumptions. Each parameter was calculated based on Japanese market price and then the indices (such as actuator index (price per 100,000 ¥), material index (price per 100,000 ¥), manufacturing index (price per 100,000 ¥), mechanical index (price per 100,000 ¥), electronic index (price per 100,000 ¥), energy price index (required power price per 100,000 ¥)) were measured and compared with the harvestable surface ( $S_n$ ) and  $HL$ . As the results indicated, economic and energy indices increased by DOF growth. With an increase in the DOF, the number of required actuator (servo motor), amplifier, connection cables, joint components, control components, and manufacturing time are also increased. More servo motor required more energy and connection

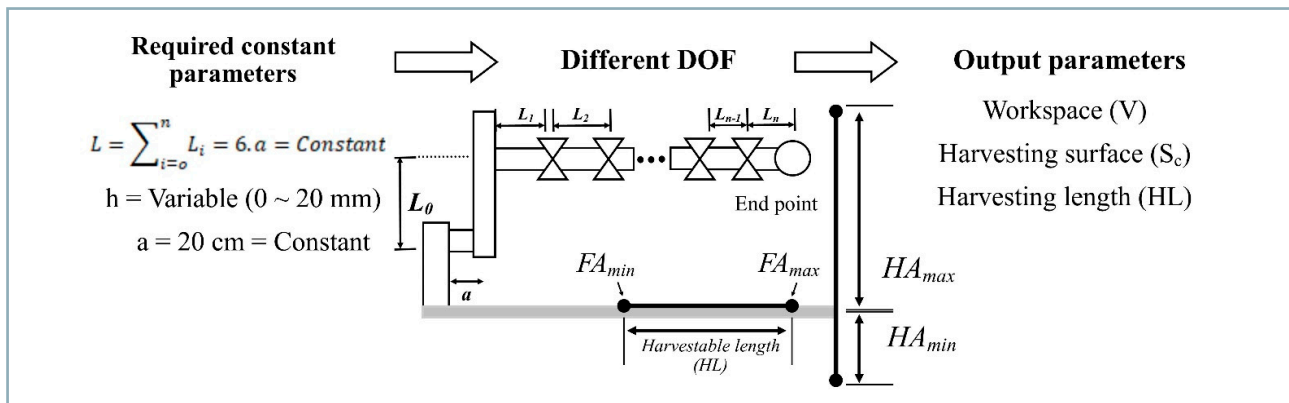


Fig. 3 DOF optimization methodology

DOF	1	2	3	4	5
Diagram					
Workspace					

Fig. 4 Comparison of different DOFs in the workspace

cable; furthermore, the controlling algorithm got also more complex. However, increasing the DOF from 4 to 5 did not increase the  $I_s$  and  $HL$  significantly. Therefore, the 5-DOF robotic cannot be an optimized structure for described application and required parameters. In considering the

constant length and different DOF, a 4-DOF could be an adequate structure that can support a maximum  $V_n$  and  $S_n$  at the minimum cost. Based on these evaluations, a 4-DOF structure was selected to develop a harvesting robotic system.

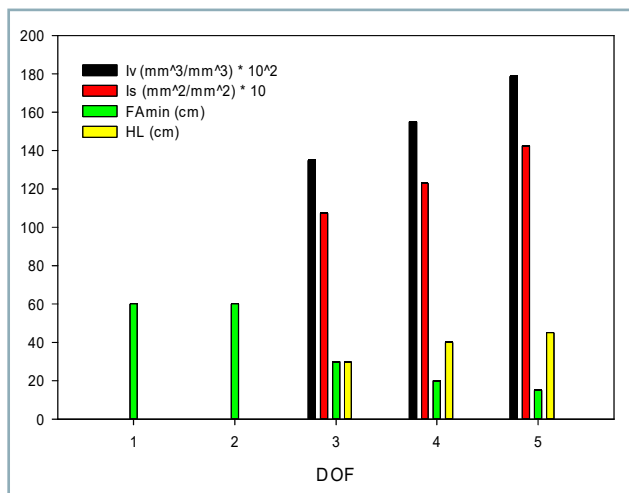


Fig. 5 Required parameters in different DOFs

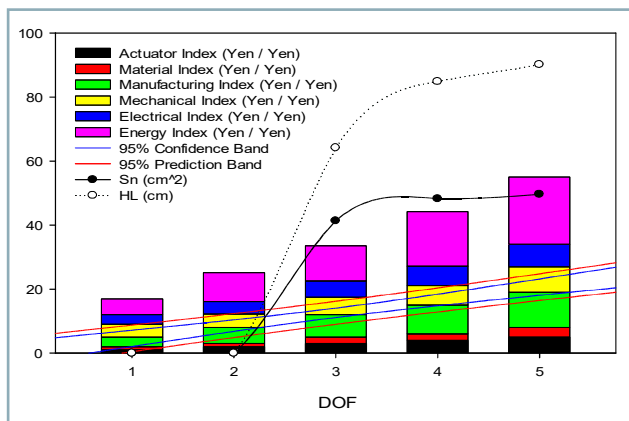


Fig. 6 Economic optimization indices

Working space

After developing the controlling algorithm, the robot working space resulted based on kinematic equations, as shown in Fig. 7. The designed robotic arm should be able to manoeuvre in the field and move aside tractors for reloading harvested crops in a truck or predetermined elevator on the right or left tractor side. Based on that, the working space should reach a long distance aside from Fig. 7, the designed robotic arm can reach 2.9 m and 2.4 m in the X- and Y-directions, respectively, the workspace area is 11.4 m<sup>2</sup>, and  $L_1, L_2$  and  $L_3$  are 500, 1,200; and 1,200; respectively. The  $L_i$  is the length of link number- $i$ . By increasing the values of  $L_1, L_2, L_3$ , it is possible to increase the working space, but it is important to consider the torque value on each joint due to the weight and distance increases. Furthermore, by increasing the length of each link, the inertia applied increases due to velocity during acceleration and deceleration.

Conclusion

In this paper, a 4-DOF SCARA type robotic arm was designed for agriculture application using the Solidworks software; this arm is capable of carrying out the farm works, such as seeding and planting of various crops using different EEs, performing a variety of farming tasks, including minimal cultivation, watering, fertilizing, spraying, and weeding; and doing selective harvesting for various crops. The forward and inverse kinematics calculation were conducted based on the designed robotic arm calculation and the controlling algorithm was written in Visual C++ using the equations. In a complementary paper, the dynamic simulations and calculations identical to the controlling algorithm will be presented.

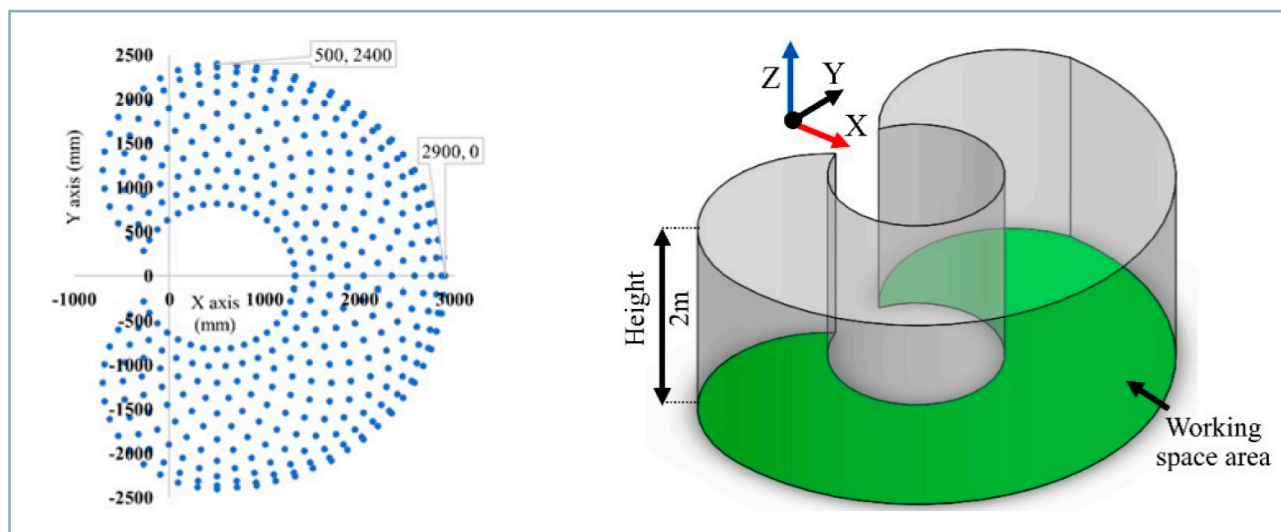


Fig. 7 Working space of designed robot, top view (left), 3D view (right)

## References

- ACCENTURE. 2017. The Future of Food: New Realities for the Industry. Available at: [https://www.accenture.com/us-en/\\_acnmedia/pdf-70/accnture-future-of-food-new-realities-for-the-industry.pdf](https://www.accenture.com/us-en/_acnmedia/pdf-70/accnture-future-of-food-new-realities-for-the-industry.pdf)
- ALIASGARIAN, S. – GHASSEMZADEH, H. R. – MOGHADDAM, M. – GHAFFARI, H. 2015. Mechanical damage of strawberry during harvest and postharvest operations. In *Acta Technologica Agriculturae*, vol. 18, no. 1, pp. 1–5.
- AYRE, M. – MC COLLUM, V. – WATERS, W. – SAMSON, P. – CURRO, A. – NETTLE, R. – PASCHEN, J. A. – KING, B. – REICHEL, N. 2019. Supporting and practising digital innovation with advisers in smart farming. In *NJAS – Wageningen Journal of Life Sciences*, vol. 90–91, no. December, pp. 100302.
- BRONSON, K. 2019. Looking through a responsible innovation lens at uneven engagements with digital farming. In *NJAS – Wageningen Journal of Life Sciences*, vol. 90–91, no. December, pp. 100294.
- CVIKLOVIČ, V. – OLEJÁR, M. – HRUBÝ, D. – PALKOVÁ, Z. – LUKÁČ, O. – HLAVÁČ, P. 2016. Navigation algorithm using fuzzy control method in mobile robotics. In *Acta Technologica Agriculturae*, vol. 19, no. 1, pp. 19–23.
- DORWARD, A. 2013. Agricultural labour productivity, food prices and sustainable development impacts and indicators. In *Food Policy*, vol. 39, pp. 40–50.
- FAO. 2012. Global Agriculture Towards 2050. Available at: [http://www.fao.org/fileadmin/templates/esa/Global\\_persepctives/world\\_ag\\_030\\_0\\_012\\_rev.pdf](http://www.fao.org/fileadmin/templates/esa/Global_persepctives/world_ag_030_0_012_rev.pdf)
- FAO. 2017. The Future of Food and Agriculture – Trends and Challenges. Rome, 163 pp.
- GARNER, J. P. – MEEHAN, C. L. – FAMULA, T. R. – MENCH, J. A. 2006. Genetic, environmental, and neighbor effects on the severity of stereotypies and feather picking in Orange-winged Amazon parrots (*Amazona amazonica*): An epidemiological study. In *Applied Animal Behaviour Science*, vol. 96, no. 1–2, pp. 153–68.
- KAMATA, T. – ROSHANIANFARD, A. – NOGUCHI, N. 2018. Heavy-weight crop harvesting robot – controlling algorithm. In *IFAC–PapersOnLine*, vol. 51, no 17, pp. 244–49.
- KASHKAROV, A. – DIORDIIEV, V. – SABO, A. – NOVIKOV, G. 2018. Semi-autonomous drone for agriculture on the tractor base. In *Acta Technologica Agriculturae*, vol. 21, no. 4, pp. 149–52.
- KLERKX, L. – JAKKU, E. – LABARTHE, P. 2019. A review of social science on digital agriculture, smart farming and agriculture 4.0: New contributions and a future research agenda. In *NJAS – Wageningen Journal of Life Sciences*, vol. 90–91, pp. 100315.
- LI, Z. – MIAO, F. – YANG, Z. – WANG, H. 2019. An anthropometric study for the anthropomorphic design of tomato-harvesting robots. In *Computers and Electronics in Agriculture*, vol. 163, no. December, pp. 104881.
- LIU, Y. – NOGUCHI, N. – ROSHANIANFARD, A. 2017. Simulation and test of an agricultural unmanned airboat maneuverability model. In *International Journal of Agricultural and Biological Engineering*, vol. 10, no. 1 pp. 88–96.
- LUO, L. – TANG, Y. – LU, Q. – CHEN, X. – ZHANG, P. – ZOU, X. 2018. A vision methodology for harvesting robot to detect cutting points on peduncles of double overlapping grape clusters in a vineyard. In *Computers in Industry*, vol. 99, pp. 130–139.
- LV, J. – WANG, Y. – XU, L. – GU, Y. – ZOU, L. – YANG, B. – MA, Z. 2019. A method to obtain the near-large fruit from apple image in orchard for single-arm apple harvesting robot. In *Scientia Horticulturae*, vol. 257, no 17, pp. 108758.
- MARINOUDI, V. – SØRENSEN, C. G. – PEARSON, S. – BOCHTIS, D. 2019. Robotics and labour in agriculture. A context consideration. In *Biosystems Engineering*, vol. 184, pp. 111–21.
- OKTEM, A. 2008. Effect of water shortage on yield, and protein and mineral compositions of drip-irrigated sweet corn in sustainable agricultural systems. In *Agricultural Water Management*, vol. 95, no. 9, pp. 1003–1010.
- ROSHANIANFARD, A. 2018. Development of a Harvesting Robot for Heavy-Weight Crop, Ph.D. Thesis, Hokkaido University.
- ROSHANIANFARD, A. – KAMATA, T. – NOGUCHI, N. 2018. Performance evaluation of harvesting robot for heavy-weight crops. In *IFAC–PapersOnLine*, vol. 51, no. 17 pp. 332–338.
- ROSHANIANFARD, A. – NOGUCHI, N. 2016. Development of a 5DOF robotic arm (RAVebots–1) applied to heavy products harvesting. In *IFAC – Papers OnLine*, vol. 49, no. 16, pp. 155–160.
- ROSHANIANFARD, A. – NOGUCHI, N. 2017. Development of heavy-weight crops robotic harvesting system (HCRHS). In *The 3<sup>rd</sup> International Conference on Control, Automation and Robotics (ICCAR 2017)*. Tokyo, Japan.
- ROSHANIANFARD, A. – NOGUCHI, N. 2018a. Characterization of pumpkin for a harvesting robot. In *IFAC – Papers OnLine*, vol. 51, no. 17, pp. 23–30.
- ROSHANIANFARD, A. – NOGUCHI, N. 2018b. Kinematics analysis and simulation of a 5DOF articulated robotic arm applied to heavy products harvesting. In *Tarim Bilimleri Dergisi*, vol. 24, no. 1, pp. 91–104.
- ROSHANIANFARD, A. – NOGUCHI, N. – OKAMOTO, H. – ISHII, K. 2020. A review of autonomous agricultural vehicles (the experience of Hokkaido University). In *Journal of Terramechanics*, vol. 91, pp. 155–183.
- ROSHANIANFARD, A. – NOGUCHI, N. – KAMATA, T. 2019. Design and performance of a robotic arm for farm use. In *International Journal of Agricultural and Biological Engineering*, vol. 12, no. 1, pp. 146–158.
- SHIBUSAWA, S. 2018. Digital farming approach changes the context. In *IFAC–PapersOnLine*, vol. 51, no. 17, pp. 67–69.
- WANG, H. – NOGUCHI, N. 2019. Navigation of a robot tractor using the centimeter level augmentation information via Quasi-Zenith Satellite System. In *Engineering in Agriculture, Environment and Food*, vol. 12, pp. 414–419.
- WILLIAMS, H. A. M. – JONES, M. H. – NEJATI, M. – SEABRIGHT, M. J. – BELL, J. – PENHALL, N. D. – BARNETT, J. J. – DUKE, M. D. – SCARFE, A. J. – AHN, H. S. – LIM, J. – MACDONALD, B. A. 2019. Robotic kiwifruit harvesting using machine vision, convolutional neural networks, and robotic arms. In *Biosystems Engineering*, vol. 181, pp. 140–156.
- XIONG, Y. – PENG, C. – GRIMSTAD, L. – FROM, P. J. – ISLER, V. 2019. Development and field evaluation of a strawberry harvesting robot with a cable-driven gripper. In *Computers and Electronics in Agriculture*, vol. 157, pp. 392–402.
- ZHANG, Z. – NOGUCHI, N. – ISHII, K. – YANG, L. – ZHANG, C. 2013. Development of a robot combine harvester for wheat and paddy harvesting. In *IFAC Proceedings Volumes*, vol. 46, no. 4, pp. 45–48.



Acta Technologica Agriculturae 2  
Nitra, Slovaca Universitas Agriculturae Nitriae, 2021, pp. 67–71

## MODELLING OF THIN-LAYER DRYING OF OSMO-PRETREATED RED BELL PEPPER

Michael Mayokun ODEWOLE<sup>1\*</sup>, Kehinde James FALUA<sup>2</sup>

<sup>1</sup>University of Ilorin, Kwara State, Nigeria

<sup>2</sup>Ekiti State College of Agriculture and Technology, Isan-Ekiti, Ekiti State, Nigeria

The paper observes a thin-layer drying behaviour of red bell pepper. The red bell pepper (192 samples) was pretreated in osmotic solution of salt of concentrations 5–20% (w/w) at osmotic solution temperatures (30–60 °C) and osmotic process durations (30–120 min) and dried at 60 °C in a locally fabricated convective dryer after preformation of osmotic dehydration pretreatment process. Experimental moisture content values obtained from the drying process were converted to moisture ratios. Seven existing thin-layer drying model equations were used for model equation fitting. The predicted and experimental (observed) moisture ratios were analysed statistically. The statistical indices and rules used to judge and select the model equation that would best describe the process were the highest values of coefficient of determination ( $R^2$ ); the lowest values of chi-square ( $\chi^2$ ), root mean square error (RMSE), and sum of squares error (SSE). Results showed that the two-term exponential model equation best described the drying behaviour of osmo-pretreated red bell pepper. The ranges of statistical indices of selected two-term exponential model equation are:  $R^2$  (0.9389–0.9751),  $\chi^2$  (0.0642–0.1503), RMSE (0.2032–0.1668), and SSE (0.6424–1.5027).

**Keywords:** osmotic dehydration; model fitting; model selection; hypertonic solution; vegetable

The red bell pepper (*Capsicum annum*) is a fruit vegetable, which is rich in terms of nutritional and medicinal properties (Wallace et al., 2020; Slavin and Lloyd, 2012). Unfortunately, approx. 20–30% of it (and other kinds of peppers) are lost yearly during the post-harvest stage (Okunoya, 1996). One of the ways of curtailing the incidence of post-harvest losses and ensuring all year-round supply of red bell pepper is to subject it to appropriate pretreatments and efficient moisture reduction via drying.

Osmotic dehydration is one of the methods for pretreating foods, especially fruits and vegetables. It is a simultaneous movement of liquid out of a product and corresponding movement of solute into the product in a counter-current manner when the product is immersed in osmotic solution (Yadav and Singh, 2014; Tortoe, 2010). Furthermore, osmotic dehydration is the partial removal of water by direct contact of a product with a hypertonic medium, i.e. high concentration of sugar or salt solutions (Ozen et al., 2002). It is one of the simpler and more economical methods of extending the shelf life of perishable products, and it preserves the colour, flavour, and texture of foods that would be affected by heat, thereby improving the nutritional, sensory and functional characteristics of foods (Singh et al., 2006).

Drying is a simultaneous heat and mass transfer process, which is achieved by the removal of enough or predetermined moisture from food and other biological materials. The objectives of drying are the prevention of decay and spoilage of food; extension of shelf life; reduction of costs of storage, handling and transportation;

and improvement of quality. There is a need for promotion of drying of fruits and vegetables in order to ensure their all-year-round supply (Kiremire et al., 2010). The best temperature range for drying fruits and vegetables was reported to be 35–75 °C (Idah et al., 2011; Phisut, 2012; Mu'azu et al., 2012).

In terms of thickness of products to be dried, drying method can be classified as either a thin layer, or deep bed. In thin-layer drying, products with approx. 15–20 cm thickness are fully exposed to drying air and drying conditions are assumed to be constant. However, in deep bed drying, product thickness exceeds 20 cm and can reach up to 45 cm (Kumar et al., 2012). Moreover, products are not exposed to the same drying conditions, which leads to formation of drying zones along the drying products. One of the relationships between the thin-layer drying and deep-bed drying is that a deep bed drying analysis is performed by taking a small part of a product undergoing deep bed drying to form a thin layer. The thin layer formed would then be subjected to numerical integration procedures along the whole dimension of the product undergoing deep bed drying. Ojediran and Raji (2010) and Raji et al. (2010) reported numerous studies on thin-layer drying of food and other agricultural products. Existing mathematical models such as Henderson and Pabis, Page, Modified Page (I and II), Thomson, Newton, and Wang and Singh have been frequently used (and are still in use) to describe the drying characteristic of certain products under thin-layer drying conditions (Ojediran and Raji, 2010). Vitázek and Havelka (2013, 2014) studied the sorption isotherms

of agricultural products with the use of Henderson model equation. Seiedlou et al. (2010), Faisal et al. (2013), Ojediran and Raji (2010, 2011), Ademiluyi and Abowei (2013), and Awogbemi and Ogunleye (2009) described the thin-layer drying modelling of different products. Most frequently, the indices used to evaluate and select the best models in terms of deviation between predicted values (by existing models) and observed (experimental) values were the coefficient of determination ( $R^2$ ), chi-square value ( $\chi^2$ ), root mean square error (RMSE), and sum of square error (SSE) statistics.

Although there exist several published works on pretreatment and drying of peppers (including red bell pepper) to different value-added products (Arslan and Ozcan, 2011; Barih et al., 2012; Osunde and Makama-Musa, 2007; Odewole and Olaniyan, 2016; Tunde-Akintunde et al., 2011; Chaethong et al., 2012; Famurewa et al., 2006); however, attention has not really been focused on the thin-layer drying behaviour of osmo-pretreated red bell pepper. Therefore, the objective of this study was to establish the thin-layer drying model(s) that would best describe the drying behaviour of osmo-pretreated red bell pepper. The established model(s) would help to have better understanding of the process in terms of reliable prediction and estimation, system and process design, analysis, and simulation for industrial scaling up of the process in the future.

## Material and methods

### Experimental materials

Red bell pepper fruits (87% wb), common salt (NaCl) and distilled water were the major materials used for the osmotic dehydration pretreatment process. The equipment used included two water baths (HH-W420, XMTD-204 model and SL Shell Lab model), Genlab electric oven, electronic weighing balance (OHAUS 3001, capacity: 3,000 g; readability: 0.1 g; stabilization time: 3 sec) and desiccators and a locally fabricated convective dryer (Odewole and Olaniyan, 2016). The dryer basically consists of drying chamber, heating chamber and blower. The external dimensions of dryer are 56 × 56 × 86 cm, while the internal dimensions are 50 × 50 × 80 cm. Its drying chamber has three perforated trays 15 cm apart. The heating chamber is of pyramidal shape and equipped with electrical heating coil of 1.8 kW, which is directly positioned in front of the blower for faster heat circulation. The blower rated power is 373 W.

### Osmotic dehydration process

The red bell pepper fruits were deseeded after washing and manually cut into pieces to a width of approx. 3 mm using a prefabricated stainless-steel knife, and this width was maintained for all samples. The cutting was performed in order to enhance the exposure of samples to the osmotic solution. After cutting, 50 g of the red bell pepper was measured with the electronic weighing balance and used as the experimental quantity. The experimental design used was 43 factorial experiment in a randomized complete block design with three replicates, which resulted in 192 experimental runs in total. All samples were subjected to osmotic dehydration pretreatment process in hypertonic

salt (NaCl) solution of four different concentrations – 5, 10, 15 and 20% (w/w), in two water baths set to four osmotic solution temperatures (30, 40, 50 and 60 °C), and left for 60-, 90-, 120- and 150-min osmotic process durations, respectively. The ratio of osmotic solution to mass of red bell pepper was 4 : 1.

### Pre-drying and drying of osmo-pretreated samples

After the osmotic dehydration pretreatment process, all pretreated samples were left under a running fan for approx. 20 min. This was conducted in order to get rid of surface water that can unnecessarily prolong the drying time. Subsequently, all osmo-pretreated samples were re-weighed using the electronic weighing balance. There was observed a reduction in mass of each sample to 40–30 g from the initial 50 g used for osmotic dehydration pretreatment. This confirmed that the osmotic dehydration took place. All samples were dried inside the fabricated convective dryer at 60 °C. The mass values of samples were recorded hourly using the electronic weighing balance until effective drying of all samples was achieved at an average moisture content of 10% (wb). The average drying time was seven hours. The data obtained (mass of samples during drying) were used to estimate the moisture content values using the procedures similar to the one in Sunmonu et al. (2018), as briefly stated below: a clean crucible was first dried in oven for approx. 30 min and then cooled in a desiccator. Cooled crucible was weighed as ( $W1$ ) using an analytical balance. Weighed quantity of about 5 g of cut red bell pepper was then introduced into the previously dried and weighed crucible and weighed as ( $W2$ ) before drying. This was placed in an electric oven, which was set to 105 °C for approx. 3 hours. The crucible with dried red bell pepper was then removed from the oven and immediately cooled in a desiccator and then weighed as ( $W3$ ). The moisture content of samples was estimated as follows:

$$M (\%) = \frac{W2 - W3}{W2 - W1} \cdot 100 \quad (1)$$

where:

- $M$  – moisture content (wet basis) at time ( $t$ )
- $W1$  – weight of clean crucible (g)
- $W2$  – weight of clean crucible plus sample (g)
- $W3$  – weight of clean crucible plus dried sample (g)
- $W2 - W3$  – total loss in weight (g)
- $W2 - W1$  – weight of sample (g)

The average room temperature and relative humidity were approx. 30 °C and 65%, respectively.

### Model fitting and model selection

The moisture content values initially obtained from the experiment after estimation were converted to moisture ratio values using Eq. 2. This was in line with the approach adopted in Ojediran and Raji (2010).

$$MR = \frac{M - M_e}{M_o - M_e} \quad (2)$$

where:

$MR$  – moisture ratio

$M$  – moisture content at time ( $t$ )

$M_o$  – initial moisture content of the sample

$M_e$  – equilibrium moisture content

The conversion of moisture content to moisture ratio was conducted to make the experimental data conform to the terms of all selected seven existing thin-layer drying model equations used for model fitting (Table 1). Each equation was linearized and solved with the use of EXCEL 2016 spread sheet in order to get all the statistical indices ( $R^2$ ,  $\chi^2$ , SSE and RMSE) needed to judge and select the equations that would best describe the thin-layer drying behaviour of the product. The data analysis was primarily based on the differences between predicted data (moisture ratio) by the models and the observed (experimental) data obtained from the experiment. Ranking and selection of the best models were carried out on the basis of highest  $R^2$  values and lowest  $\chi^2$ , SSE and RMSE values.

### Model equation solution

Selected model equation that best described the process characteristics was solved in order to simplify it. The solution was performed by first substituting the values of coefficients and constants obtained at osmotic solution temperatures 30, 40, 50 and 60 °C into the selected model equation. This was followed by manual analytical style of solving mathematical equation until simplest forms of equations were obtained.

## Results and discussion

### Model performance and selection

Performance results of all seven models at each osmotic solution temperature are presented in Tables 2, 3, 4 and 5. The existing thin-layer drying model that best described the behaviour of dried osmo-pretreated red bell pepper is the one with "1<sup>st</sup>" notation under the rank column. Considering all the osmotic solution temperatures used for the pretreatment (30, 40, 50 and 60 °C), the two-term exponential model best described the behaviour of red bell pepper at drying temperature of 60 °C. Similarly, Newton model took the second position (2<sup>nd</sup>) in terms of ranking and it is thus considered the second best. The reason for different ranking of the models can be caused by different terms and number of coefficients of the terms of each model. This might have consequential impact on the numerical values of statistical indices used for adjudging the models. Furthermore, another reason might be due to the fact that several existing models had initially certain shortcomings before they were later improved. The latter statement is in agreement with Ojediran and Raji (2010), who reported that Page model was modified to correct some of the shortcomings of Henderson and Pabis model. Ojediran and Raji (2011) used the five thin-layer drying models to study the drying pattern of castor seed (*Ricinus communis*); modified Page model was reported to be the best model equation for description of the seed drying pattern. Seiedlou et al. (2010) carried out the mathematical modelling of apple slices under

**Table 1** Seven selected existing thin-layer drying model equations

SN	Model equation	Model name	Model code
1	$MR = \exp(-kt)$	Newton	M1
2	$MR = \exp(-kt^n)$	Page	M2
3	$MR = a \exp(-kt)$	Henderson and Pabis	M3
4	$MR = 1 + at + bt^2$	Wang and Singh	M4
5	$MR = a \exp(-kt) + b$	logarithmic	M5
6	$MR = a \exp(-kt^n) + bt$	Midilli	M6
7	$MR = a \exp(-kt) + (1 - a) \exp(-kat)$	two-term exponential	M7

$MR$  – moisture ratio,  $t$  – drying time;  $a, b, n, k$  – model constants and coefficients

**Table 2** Model performance for 30 °C osmotic solution temperature

Models	$R^2$	$\chi^2$	RMSE	SSE	Coefficients				Rank
M1	0.9738	0.0781	0.1818	0.8590	$k = 0.0815$				2 <sup>nd</sup>
M2	0.9432	0.1374	0.2299	1.3739	$k = 0.0063$	$n = 1.053$			6 <sup>th</sup>
M3	0.9696	0.0986	0.1947	0.9861	$k = 0.0967$	$a = 1.0529$			4 <sup>th</sup>
M4	0.9834	0.1149	0.2102	1.1486	$a = -0.0615$	$b = 1.0413$			5 <sup>th</sup>
M5	0.9696	0.1059	0.1915	0.9531	$k = 0.0967$	$a = 1.037$	$b = 0.0099$		3 <sup>rd</sup>
M6	0.9441	0.1720	0.2300	1.3756	$k = 0.0065$	$a = 0.0868$	$b = 0.9621$	$n = 0.1066$	7 <sup>th</sup>
M7	0.9690	0.0723	0.1668	0.7231	$k = 0.1037$	$a = 0.0012$			1 <sup>st</sup>

**Table 3** Model performance for 40 °C osmotic solution temperature

Models	R <sup>2</sup>	χ <sup>2</sup>	RMSE	SSE	Coefficients			Rank
M1	0.9447	0.0659	0.1670	0.7251	k = 0.0859			2 <sup>nd</sup>
M2	0.9972	0.0936	0.1897	0.9359	k = 0.0189	n = 1.6609		5 <sup>th</sup>
M3	0.9393	0.0761	0.1711	0.7614	k = 0.0966	a = 1.0985		4 <sup>th</sup>
M4	0.9682	0.1034	0.1995	1.0343	a = -0.0611	b = 0.0009		7 <sup>th</sup>
M5	0.9393	0.0807	0.1671	0.7263	k = 0.0966	a = 1.1701	b = -0.0651	2 <sup>nd</sup>
M6	0.9969	0.1177	0.1903	0.9414	k = 0.0152	a = 0.9769	b = -0.0002	n = 1.7470
M7	0.9389	0.0642	0.1572	0.6424	k = 0.0992	a = 0.8697		1 <sup>st</sup>

**Table 4** Model performance for 50 °C osmotic solution temperature

Models	R <sup>2</sup>	χ <sup>2</sup>	RMSE	SSE	Coefficients			Rank
M1	0.9760	0.1012	0.2069	1.1134	k = 0.0711			2 <sup>nd</sup>
M2	0.9766	0.1467	0.2375	1.4669	k = 0.0218	n = 1.4862		6 <sup>th</sup>
M3	0.9751	0.1217	0.2164	1.2170	k = 0.0759	a = 1.0699		4 <sup>th</sup>
M4	0.9806	0.1390	0.2312	1.3903	a = -0.0553	b = 0.0007		5 <sup>th</sup>
M5	0.9753	0.1309	0.2129	1.1780	k = 0.0751	a = 1.1542	b = -0.0807	3 <sup>rd</sup>
M6	0.9704	0.1861	0.2393	1.4891	k = 0.0172	a = 0.9662	b = 0.0008	n = 1.5399
M7	0.9751	0.1073	0.2032	1.0731	k = 0.0772	a = 0.8976		1 <sup>st</sup>

**Table 5** Model performance for 60 °C osmotic solution temperature

Models	R <sup>2</sup>	χ <sup>2</sup>	RMSE	SSE	Coefficients			Rank
M1	0.9782	0.1427	0.2457	1.5692	k = 0.0546			2 <sup>nd</sup>
M2	0.8912	0.2758	0.3257	2.7578	k = 0.0018	n = 2.2680		7 <sup>th</sup>
M3	0.9770	0.1963	0.2747	1.9626	k = 0.0624	a = 1.1479		4 <sup>th</sup>
M4	0.9813	0.1740	0.2587	1.7404	a = -0.0478	b = 0.0006		3 <sup>rd</sup>
M5	0.9780	0.2181	0.2744	1.9632	k = 0.0557	a = 1.2936	b = -0.1501	5 <sup>th</sup>
M6	0.8615	0.3398	0.3233	2.7183	k = 0.0008	a = 0.9582	b = -0.0004	n = 2.5436
M7	0.9768	0.1503	0.2404	1.5027	k = 0.0669	a = 0.7878		1 <sup>st</sup>

convective drying; out of approx. ten model equations used, the model equation presented in Aghbashlo et al. (2009) best described the drying behaviour of product. Faisal et al. (2013) reported that Midilli model best described the drying characteristics of pretreated potato cubes dried at the maximum temperature of 80 °C, as well as thin layer drying of cassava slices in a convective dryer (Dairo et al., 2015). Furthermore, Ojediran and Raji (2010) concluded that modified Page and Page models best described the

drying characteristics of EX-BORNO and SOSAT C88 millets, respectively, at drying temperature range of 30–70 °C.

**Solution and simplification of selected model equation**

Table 6 presents different solutions of the selected two-term exponential model equation (coded M7 in Tables 2–5). The equations obtained after the solution are simplified for ease of use and for faster execution of computation.

**Table 6** Solutions of the two-term exponential model equation

Osmotic solution temperature	a	k	MR = aexp(-kt) + (1 - a)exp(-kat): M7 (two-term exponential model equation)
30 °C	0.0012	0.1037	MR = 0.0012(0.9015t) + 0.9988(0.9999t)
40 °C	0.8697	0.0992	MR = 0.8697(0.9056t) + 0.1303(0.9173t)
50 °C	0.8976	0.0772	MR = 0.8976(0.9257t) + 0.1024(0.9330t)
60 °C	0.7878	0.0669	MR = 0.7878(0.9353t) + 0.2122(0.9487t)

## Conclusion

The drying behaviour of osmo-pretreated red bell pepper using seven existing thin-layer drying models was studied. The two-term exponential model best described the drying behaviour of the product in osmotic solution temperature range of 30–60 °C and drying air temperature of 60 °C. The solved two-term exponential model equations can be used to predict and estimate the moisture ratios and drying times of red bell pepper pretreated in osmotic solution temperatures ranging from 30 °C to 60 °C. Moreover, these solutions can serve as useful tools for optimizing and simulating the food processing operations with a view to upscaling it to industrial level, as well in designing efficient dryers needed for the process. Values obtained for other models that were not selected can be also used as reference and guide for other similar studies in future.

## References

- ADEMILUYI, F. T. – ABOWEI, M. F. N. 2013. Theoretical model for predicting moisture ratio during drying of spherical particles in a rotary dryer. In *Modelling and Simulation in Engineering*, vol. 21, no. 3, pp. 1–7.
- AGHBASHLO, M. – KIANMEHR, M. H. – KHANI, S. – GHASEMI, M. 2009. Mathematical modeling of carrot thin-layer drying using new model. In *International Agrophysics*, vol. 23, no. 4, pp. 313–317.
- ARSLAN, D. – OZCAN, M. M. 2011. Dehydration of red bell pepper (*Capsicum annum* L.): change in drying behaviour, colour and antioxidant content. In *Food and Bioproduct Processing*, vol. 89, no. 1, pp. 504–513.
- AWOGBEMI, O. – OGUNLEYE, I. O. 2009. Effects of drying on the qualities of some selected vegetables. In *International Journal of Engineering and Technology*, vol. 1, no. 5, pp. 409–414.
- BAREH, G. F. – NADIR, A. S. – WAFAA, M. A. – ELZAMAZMY, F. M. 2012. Effect of solar drying on nutritional characteristics of different pepper varieties and its mixture with tomato. In *Journal of Applied Sciences Research*, vol. 8, no. 3, pp. 1415–1424.
- CHAETHONG, K. – TUNNARUT, D. – PONGSAWATMANIT, R. 2012. Quality and colour parameters of dried chilli and chilli powder pretreated by metabisulfite soaking with different times concentrations. In *Kasetsart Journal (Natural Science)*, vol. 46, no. 1, pp. 473–484.
- DAIRO, O. U. – ADERINLEWO, A. A. – ADEOSUN, O. J. – OLA, I. A. – SALAUDEEN, S. 2015. Solar drying kinetics of cassava slices in a mixed flow dryer. In *Acta Technologica Agriculturae*, vol. 18, no. 4, pp. 102–107.
- FAISAL, S. – TABASSUM, R. – KUMAR, V. 2013. Performance evaluation and process optimization of potato drying using hot air oven. In *Food Processing and Technology*, vol. 4, no. 10, pp. 1–9.
- FAMUREWA, J. A. V. – OLUWAMUKOMI, M. O. – ADENUGA, A. O. 2006. Dehydration of osmosed red bell pepper (*Capsicum annum*). In *Journal of Biological Sciences*, vol. 1, no. 1, pp. 36–39.
- IDAH, P. A. – MUSA, J. J. – OLALEYE, S. T. 2011. Effect of temperature and drying time on some nutritional quality parameters of dried tomatoes. In *AU Journal of Technology*, vol. 14, no. 1, pp. 25–32.
- KIREMIRE, B. T. – MUSINGUZI, E. – KIKAFUNDA, J. K. – LUKWAGO, F. B. 2010. Effects of vegetable drying techniques on nutrient content: A case study of South-Western Uganda. In *African Journal of Food, Agriculture, Nutrition and Development (AJFAND)*, vol. 10, no. 5, pp. 2587–2600.
- KUMAR, S. – KUMAR, V. – SAHU, R. K. 2012. *Fundamental of Agricultural Engineering*. New Delhi, India: Kalyani Publishers, 10 pp. ISBN 9789327221688
- MU'AZU, K. – BUGAJE, I. M. – MOHAMMED, I. A. 2012. Performance evaluation of forced air convection vegetable drying system. In *Journal of Basic and Applied Scientific Research*, vol. 2, no. 3, pp. 2562–2568.
- ODEWOLE, M. M. – OLANIYAN, A. M. 2016. Effect of osmotic dehydration pretreatments on drying rate and post-drying quality attributes of red bell pepper (*Capsicum annum*). In *Agricultural Engineering International: CIGR*, vol. 18, no. 1, pp. 226–235.
- OJEDIRAN, J. O. – RAJI, A. O. 2010. Thin layer drying of millet and effect of temperature on drying characteristics. In *International Food Research Journal*, vol. 17, no. 4, pp. 1095–1106.
- OJEDIRAN, J. O. – RAJI, A. O. 2011. Thin-layer drying characteristics of castor (*Ricinus communis*) seeds. In *Journal of Food Processing and Preservation*, vol. 35, no. 5, pp. 647–655.
- OKUNOYA, J. A. 1996. Controlling post-harvest losses in tomatoes and peppers. In *Journal of Tropical Postharvest Losses*, vol. 2, pp. 136–142.
- OSUNDE, Z. D. – MAKAMA-MUSA, A. L. 2007. Assessment of changes in nutritional values of locally sun-dried vegetables. In *A.U. Journal of Technology*, vol. 10, no. 4, pp. 248–253.
- OZEN, B. F. – DOCK, L. L. – OZDEMIR, M. – FLOROS, J. D. 2002. Processing factors affecting the osmotic dehydration of diced green peppers. In *International Journal of Food Science and Technology*, vol. 37, no. 5, pp. 497–502.
- PHISUT, N. 2012. Factors affecting mass transfer during osmotic dehydration of fruits. In *International Food Research Journal*, vol. 19, no. 1, pp. 7–18.
- RAJI, A. O. – FALADE, K. O. – ABIMBOLU, F. W. 2010. Effect of sucrose and binary solution on osmotic dehydration of bell pepper (chilli) (*Capsicum spp.*). In *Journal of Food Science and Technology*, vol. 47, no. 3, pp. 305–309.
- SEIILEDLOU, S. – GHASEMZADEH, H. R. – HAMDAMI, N. – TALATI, F. MOGHADDAM, M. 2010. Convective drying of apple: Mathematical modelling and determination of some quality parameters. In *International Journal of Agriculture and Biology*, vol. 12, no. 2, pp. 171–178.
- SINGH, B. – PANESAR, P. S. – NANDA, V. – GUPTA, A. K. – KENEDY, J. F. 2006. Application of response surface methodology for the osmotic dehydration of carrots. In *Journal of Food Engineering*, vol. 29, no. 6, pp. 592–614.
- SLAVIN, J. L. – LLOYD, B. 2012. Health benefits of fruits and vegetables. In *Advances in Nutrition*, vol. 3, no. 4, pp. 506–516.
- SUNMONU, M. O. – ODEWOLE, M. M. – OYELEKE, I. O. – OTITODUN, G. O. – OMOBOWALE, M. – OGUNDARE, M. O. 2018. Empirical models and process optimization for prediction of nutritional parameters of stored cowpea variety (IT96D–610K). In *Acta Technologica Agriculturae*, vol. 21, no. 4, pp. 141–148.
- TORTOE, C. 2010. A review of osmo-dehydration for food industry. In *African Journal of Food Science*, vol. 4, no. 6, pp. 303–324.
- TUNDE-AKINTUNDE, T. Y. – AKINTUNDE, B. O. – FAGBEJA, A. 2011. Effect of blanching methods on drying kinetics of bell pepper. In *African Journal of Food, Agriculture, Nutrition and Development (AJFAND)*, vol. 11, no. 7, pp. 5457–5474.
- VITÁZEK, I. – HAVELKA, J. 2013. *I-x-w* diagram of wet air and wheat grain. In *Research in Agricultural Engineering*, vol. 59 (special issue), pp. 49–53.
- VITÁZEK, I. – HAVELKA, J. 2014. Sorption isotherms of agricultural products. In *Research in Agricultural Engineering*, vol. 60 (special issue), pp. 52–56.
- WALLACE, T. C. – BAILEY, R. L. – BLUMBERG, J. B. – BURTON-FREEMAN, B. – CHEN, C. O. – CROWE-WHITE, K. M. – DREWNOWSKI, A. – HOOSHMAND, S. – JOHNSON, E. – LEWIS, R. – MURRAY, R. – SHAPSES, S. A. – WANG, D. D. 2020. Fruits, vegetables, and health: A comprehensive narrative, umbrella review of the science and recommendations for enhanced public policy to improve intake. In *Critical Reviews in Food Science and Nutrition*, vol. 60, no. 13, pp. 2174–2211.
- YADAV, A. K. – SINGH, S. K. 2014. Osmotic dehydration of fruits and vegetables: A review. In *Journal of Food Science and Technology*, vol. 51, no. 9, pp. 1654–1673.



Acta Technologica Agriculturae 2  
Nitra, Slovaca Universitas Agriculturae Nitriae, 2021, pp. 72–78

## RESEARCH AND DEVELOPMENT OF ESSENTIALS FOR SILAGE PREPARATION, TRANSPORT AND STORAGE IN FLEXIBLE CONTAINERS OF OPTIMAL VOLUME

Zhadyra SAGYNDYKOVA<sup>1,2</sup>, Vladimir NEKRASHEVICH<sup>3</sup>, Kanat KHAZIMOV<sup>1\*</sup>,  
Bekbossyn KASSYMBAYEV<sup>1</sup>, Marat KHAZIMOV<sup>1,2,4</sup>

<sup>1</sup>Kazakh National Agrarian Research University, Almaty, Kazakhstan

<sup>2</sup>Almaty University of Power Engineering and Telecommunications named after Gumarbek Daukeyev, Almaty, Kazakhstan

<sup>3</sup>Ryazan State Agrotechnological University named after prof. P.A. Kostychev, Ryazan, Ryazan Region, Russia

<sup>4</sup>al-Farabi Kazakh National University, Almaty, Kazakhstan

The research purpose was to develop the basics for silage preparation by vacuuming with the use of flexible polymer containers and estimating silage quality. The analysis of modern systems used for silage preparation and storage showed that the main disadvantages include the high storage and preparation costs, and losses of silage weight and nutrients by 3–25% after opening of storage facilities. To eliminate these disadvantages, the basics for preparing the silage by vacuuming in flexible polymer containers that can be transported and stored with optimum volume have been studied and developed. The study pursues its goals by observing the changes in density and degree of silage compaction caused by the vacuum pressure and deadweight. A comparative estimation of silage quality indices was conducted by means of chemical analysis of silage specimens. The results show graphical dependencies of changes in silage volume and density at vacuum pressure up to 60 kPa. Moreover, a comparative assessment of quality indices of silage specimens prepared by vacuuming in soft containers, and traditional method using trenches was conducted. The reliability of results for silage storing quality in a vacuum container was achieved by fivefold test repetition within 2 years. Comparison of silage quality indices obtained using vacuum technology and traditional method showed improvement in favour of the proposed method: dry matter by 2.05%; protein by a factor of 1.47; nitrogenous substances by 1.37; starch by 1.56; calcium by 1.83; phosphorus by 2; digestible protein by 1.24; feed unit by 1.31; exchange energy by 1.16, which was achieved thanks to the elimination of succus leakage.

**Keywords:** flexible vacuum container; heavy load bags; matrix; degree of compaction

One of the most important types of feed in the diet of farm livestock is silage. It approx. amounts to 40% of the nutritional value (Kalashnikov, 2003; Khokhrin, 2002). Globally, the main crop for silage production is corn (Boyarsky, 2011a). The silage production accounts for approx. 70% of the total cattle forage in Western Europe (Jones, 1998).

Nowadays, various forage storage facilities are used for the preparation and storage of silage, including silo trench (or pit), silo bunker, silo tower, and silo bags. However, all existing technologies utilize mechanical means under stationary conditions using expensive equipment to compact the silage mass (Boyarsky, 2001b; Holmes and Muck, 2000; Revich and Nekrasevich, 2013; McAllister and Hristov, 1995; Karpenko, 1974; Sagyndykova et al., 2019a, 2019b).

Analysis of the feed ensiling using the aforementioned facilities shows a number of significant drawbacks, i.e. high costs of construction of trenches and towers, large losses of silage mass and nutrients (reaching 3–25%), silage mass acidification (Asplund, 1994; Erdman, 1993; Harrison et al., 1994; Keller et al., 1998; Limin Kung et al., 2018; Ferraretto et al., 2018; Kažimírová et al., 2020).

The top priority in silage production is to rapidly reduce oxygen level and increase acidity so that lactic acid bacteria are able to grow in order to stabilize and preserve the forage. In 2–3 days after ensiling, cell juices become available as a food source to silage bacteria. By this time, the oxygen should have been eliminated, and silage pH should have declined to a level at which the lactic acid bacteria can grow (pH = 5.5–5.7). The lactic acid bacteria start to propagate, producing lactic acid (C<sub>3</sub>H<sub>6</sub>O<sub>3</sub>) and certain amount of acetic acid (C<sub>2</sub>H<sub>4</sub>O<sub>2</sub>), which results in increased silage acidity. After approx. six weeks later, silage should reach a final pH value (3.8–4.0 in corn silage) according to Ward and Ondarza (2009), Ralh and Ondarza (2008), and Limin Kung et al. (2018). Furthermore, these researchers reviewed the evaluation of forage fermentation, which produce higher amounts of lactic acid, typically resulting in the lowest dry matter losses.

The construction of expensive structures, such as silo trenches and silo towers, is not effective on a small farm scale due to a long payback period (Orsik and Revyakin, 2008; Yemelyanov et al., 2019). Therefore, the search for efficient

**Contact address:** Kanat Khazimov, Kazakh National Agrarian University, 8 Abai avenue, Medeu district, Almaty, 050010/A25D4X5, Kazakhstan; e-mail: [kanat-86@mail.ru](mailto:kanat-86@mail.ru)

methods for forage preparation, including silage mass, is relevant.

In addition to this, readily available materials made of polyethylene films used in solar drying equipment (Khazimov et al., 2018a) and in growing vegetables (Khazimov et al., 2018b, 2019) appeared on the market, which were observed to have a wider range of application. Polyethylene films can be also used as wrapping materials in feed preparation (Korotkevich, 1990; Woolford, 1989; Toková et al., 2020).

In the last two decades, the study of vacuum effect on the ensiling process using polymer material has begun (Johnson et al., 2005; Patent RU 2625480; Patent RU 193970). The corn is ground by a forage harvester and the resulting green mass is loaded into soft containers made of airtight polyethylene film, which are installed in transport bags (Big-Bag type). The Big-Bags are placed inside truck-mounted cassettes with rigid solid walls (Patent RK 33415; Sagyndykova et al., 2019a, 2019b; Nekrashevich et al., 2015, 2017; Malarev et al., 2020). The filler of a flexible container with silage is sealed using a heat sealer. Air is pumped out of the flexible container via a flap valve using a vacuum pump. Flexible containers are vacuumed until the juice will flow out. Subsequently, such containers are extracted from a matrix by a manipulator and loaded into transportation unit and delivered to a storage facility.

Feed is stored in flexible containers inside Big-Bags folded on each other under airless conditions. In two to three storage days, the gas produced by a fermentation process inside containers should be pumped out. After 40 days, feed in the flexible containers can be used to feed livestock (Sagyndykova et al., 2019a, 2019b).

The research purpose was to develop the essentials for silage preparation in flexible polymer containers by vacuuming and assess the silage quality (Sagyndykova et al., 2019a, 2019b). The tasks that were solved include theoretical and experimental justification of parameters of flexible containers used for preparation, transport, and storage of silage, as well as comparative study of qualitative composition of silage prepared using proposed and

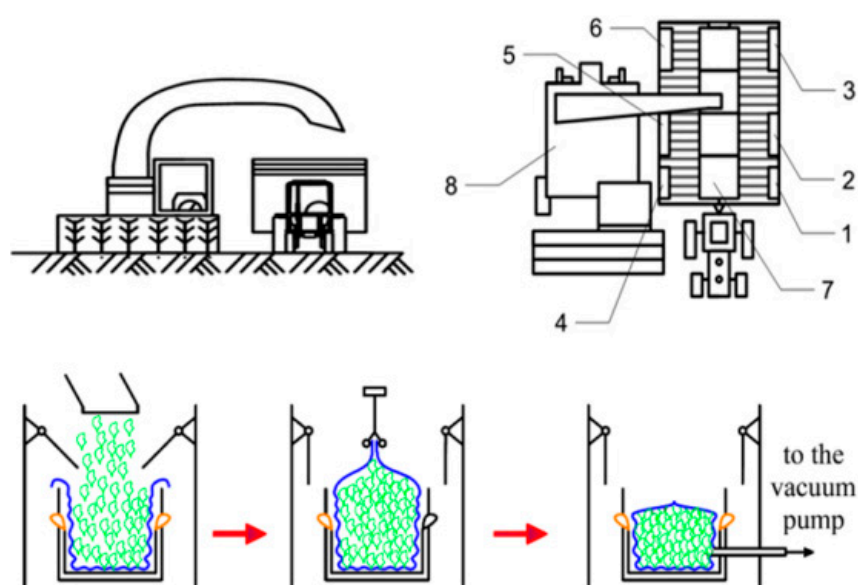


**Fig. 1** Scheme of technological process for silage preparation

1 – generator; 2 – compressor; 3 – tank with compressed air; 4 – vacuum pump; 5 – continuous heat sealers; 6 – tank; 7 – matrix for a flexible container; 8 – forage harvester

existing technological processes under industrial production conditions.

## Material and methods

The scheme of the technological process for preparation and storage of silage based on the proposed technology is shown in Fig. 1.

Transport and grinding of silage are performed by a combine. The ground mass is loaded into flexible containers placed on a truck cargo body. A flexible polyethylene container with a load-carrying bag is located inside a metal matrix. Matrix volume depends on the transport body size (Sagyndykova et al., 2019b; Zhukovskyy et al., 2019; Kuzmin and Sharifullina, 2014).

Silage preparation technology includes the following operations: preparation of green mass by cutting, grinding and loading into the vehicle; preparation of containers for filling with green mass, involving also insertion and hanging of intermediate bulk container in the matrix, and insertion of the airtight flexible container into the flexible intermediate bulk container; sealing of the container filler by continuous heat sealers; loading of the prepared containers into the vehicle using manipulator for transportation to storage facilities.

Compaction of silage in a soft container was presented by Nekrashevich et al. (2015, 2017, 2020).

A pycnometer method based on Archimedes Principle was used to determine the dependence of changes in volume of silage mass contained in flexible container on different vacuum pressures. A sealed mini container with silage mass was immersed in a container with water of a known volume and a volume of displaced water was measured before and after the mini container was compacted. The water level in a water-filled graduated cylinder was recorded before vacuuming the container with silage. After that, the air was pumped out of flexible container using a vacuum pump, resulting in an increase in the density of silage in container, and the water level was recorded again. Subsequently, the vacuum pressure inside the flexible mini container was increased. Each increase in vacuum pressure was repeated five times. Changes in the mini container volume were measured with each increase in the vacuum pressure. The differences in water levels in the measuring container were used to determine the silage mass volumes at each observed vacuum pressure (Sagyndykova et al., 2019a).

As a result of measuring the volumes of silage mass, different

density values were obtained at each level of vacuum pressure. The density was defined as the ratio of mass to volume, i.e.:

$$\rho = M \cdot V^{-1} \text{ or } \rho = M_m (V_2 - V_1)^{-1} \quad (1)$$

where:

- $\rho$  – density ( $\text{kg}\cdot\text{m}^{-3}$ )
- $M$  – mass (kg)
- $V$  – volume of silage mass ( $\text{m}^3$ )
- $M_m$  – mass of silage monolith (kg)
- $V_2 - V_1$  – water volume in cylinder before and after putting in the container ( $\text{m}^3$ )

The silage mass compaction factor was calculated as follows:

$$\lambda_{\gamma} = V_k \cdot V^{-1} = \gamma \cdot \rho^{-1} \quad (2)$$

where:

- $V$  and  $V_k$  – volume of silage before and after compaction ( $\text{m}^3$ )
- $\rho$  and  $\gamma$  – density of compacted and noncompacted silage ( $\text{kg}\cdot\text{m}^{-3}$ )

Based on the results of laboratory experiments, graphs of changes in the volume and density of silage depending on the vacuum pressure were obtained.

For the purposes of field experiments, the flexible container was made of flexible polyethylene hoses (PE-115) with a diameter of 1.6 m and a height of 3.8 m. The thickness of polyethylene plastic hoses was 200 microns. The lower side of flexible container was sealed by continuous heat welding. On one side of the flexible container, a check valve was installed for the purposes of pumping the air from a flexible container (Patent RK 33425).

A matrix for placing a Big-Bag and flexible container was made of steel in a shape of square truncated pyramid (lower  $1.0 \times 1.0$  m, upper  $1.2 \times 1.2$  m). The matrix height is 1.7 m. The dimensions of Big-Bag were selected from the standard sizes based on the possibility of using mechanized lifting devices (up to 1 ton) at farm facilities. The matrix was mounted on a plain surface. Subsequently, the Big-Bag was inserted inside the matrix until it reached the flat bottom. Lifting loops (in the upper corners) of the Big-Bag were attached to the matrix corners (in the upper part). A flexible container was placed inside the Big-Bag, reaching the flat bottom as well. The container filler was fastened along the perimeter of upper cassette base (Fig. 2).

Ground green mass was loaded into flexible containers up to the top matrix level. The neck surface of soft container was welded after cleaning the impurities. Subsequently, the air was pumped out of a flexible container through the check valve using the vacuum pump. Vacuum pressure was controlled by a vacuum gauge in the vacuum line. External structural dimensions of the container with silage mass were determined using a tape measure. The mass of the container with silage was determined using pre-calibrated dynamometric scales. The determination of parameters of vacuumed container was replicated five times.

For the purposes of biochemical analysis, the silage samples (Federal Standard R55986-2014) were taken from a silo trench and from flexible vacuum containers. Thirty flexible vacuum containers have been stored under the same conditions since September 2018 and located near the silo trench. The first flexible vacuum containers were opened in March 2019, the second in July 2019, and the last in September 2019. All silage samples came from the same corn variety and field, were transported during the same period, and had the same physical and mechanical

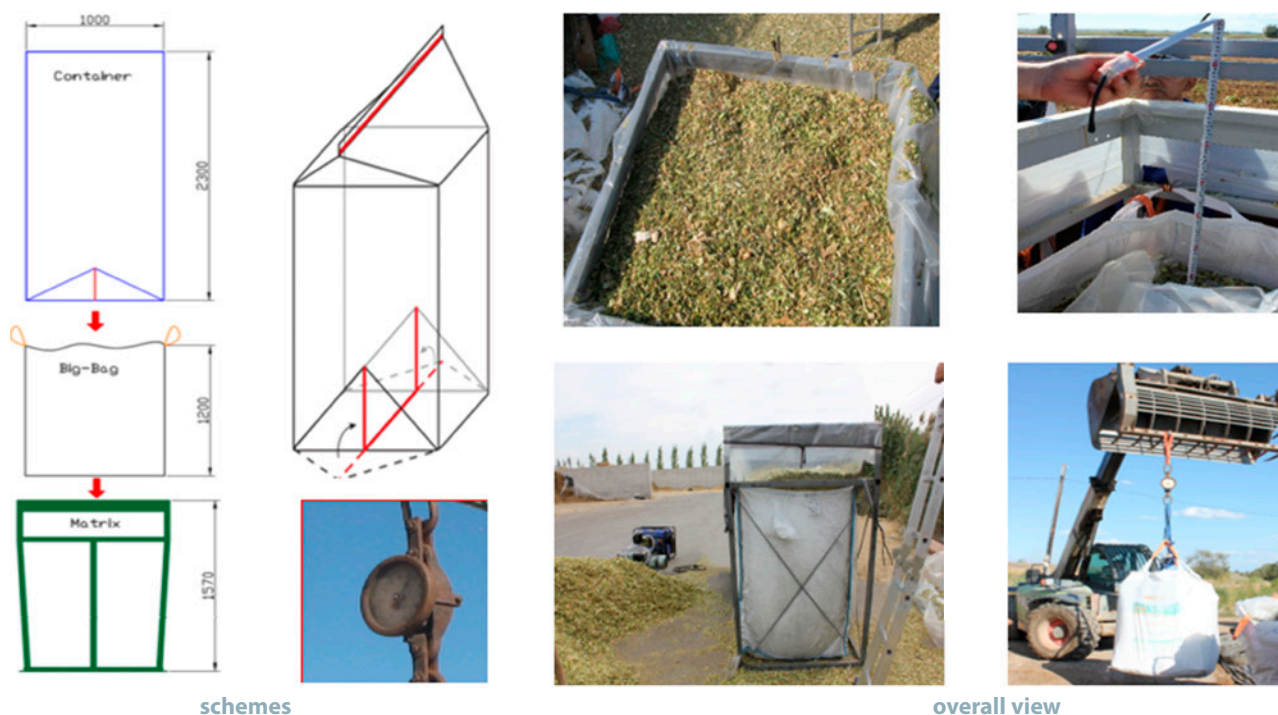


**Fig. 2** Scheme and general view of flexible container "Big-Bag" and flexible plastic container in the matrix for field test

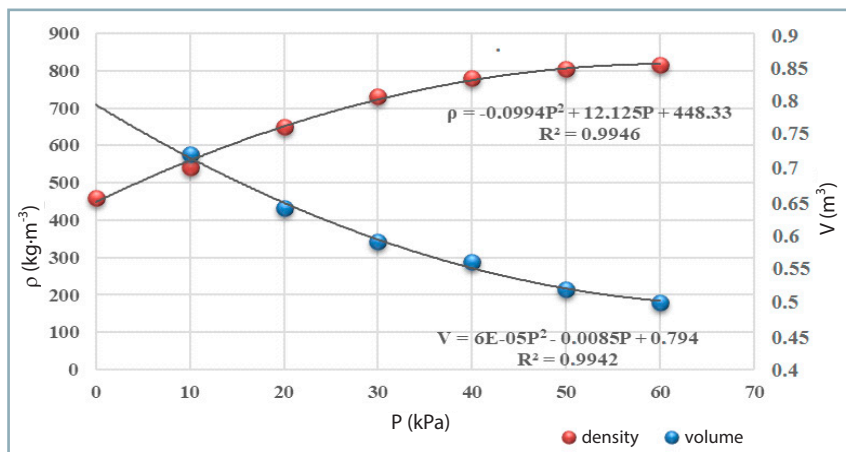


**Fig. 3** Changes in density and volume of silage in a flexible plastic container depending on vacuum pressure

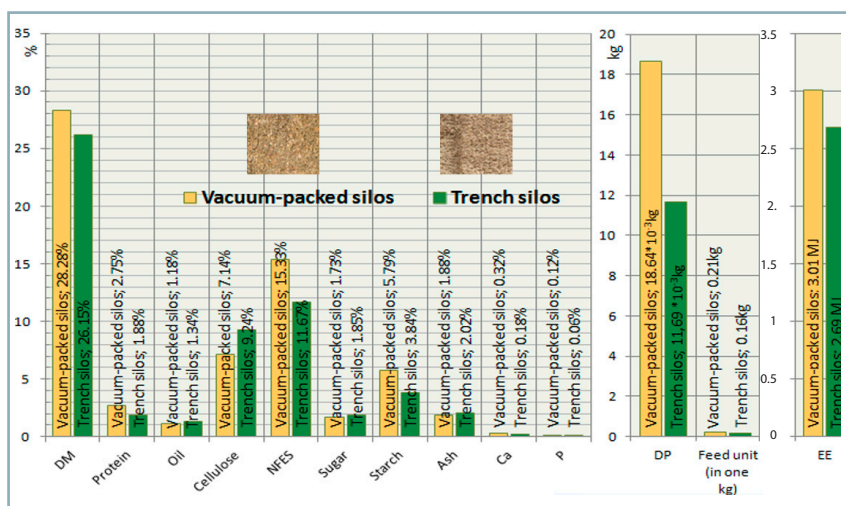


**Fig. 4** Results of forage chemical analysis in terms of natural moisture (%)

properties. Assessment methods of silage quality were carried out according to the requirements of Federal Standards RF 23638-90 and 53903-2010.

### Results and discussion

A graphical dependence of the density and volume of silage mass on the compacting pressure obtained by vacuuming the container is presented in Fig. 3. The density curve in a range

of vacuum pressure of 0 to 60 kPa increases from 460 to 820 kg·m<sup>-3</sup>. Reaching the pressure of 50 kPa, there is a stop to density increasing, which can be explained by the fact that the green mass acquires almost the density of corn stalk (approx. 850 kg·m<sup>-3</sup>). Further compaction causes the succus to flow out. Usually, the silage density in silo trenches does not exceed the value of 650 kg·m<sup>-3</sup>. Therefore, the silage density in flexible plastic containers will be ranging from 650 to 800 kg·m<sup>-3</sup>. Further compaction would result in

increased energy costs and packing time, which is unreasonable.

The change in silage volume due to compaction pressure is presented in a form of curve with decreasing tendency with increasing pressure. The ordinate report starts at 10 kPa, which is due to the fact that, after welding the neck of container with silage, a certain amount of air remains inside the folds. Therefore, for the purposes of experiment reliability, a calculation was performed for range 10–60 kPa of vacuum. Based on the curve obtained, the decrease in silage mass volume at 60 kPa was approx. 37%, which is why the container for field test was taller than the Big-Bag by 30–40%. This approach takes into account the silage mass compaction according to the theoretical calculations and the compaction will occur along the height of the flexible container to a greater extent (due to the self-weight mass of silage). The compaction coefficient λ<sub>y</sub> was employed for the purposes of practical control of mass compaction in field. It characterizes the ratio of residual volume to initial volume. A sufficient compaction value λ<sub>y</sub> equals to 0.7, which represents a decrease in volume by 30% (Fig. 3). By vacuuming the flexible container with silage in the field, the compacted mass acquired the shape of Big-Bag in the form of a rectangular prism and the dimensions decreased in comparison to original size (Table 1).

The field test showed that dimensions reduced by 9–10% in length and width, and by 40% in height. A significant change in height is related to the fact that there acts the silage weight itself besides the vacuum pressure in the vertical direction. This change was assumed in the theoretical description (Nekrashevich et al., 2020). Furthermore, this test also showed that the average density of silage in containers was 850 kg·m<sup>-3</sup> (at vacuum

**Table 1** Indicators of the geometric dimensions of the container before and after vacuuming

Items (metrics)	Height (m)	Width (m)	Length (m)
Before vacuuming	1.60	1.05	1.05
After vacuuming	0.90	0.85	0.85
After repeated vacuuming after 2 days	0.90	0.85	0.85

**Table 2** Statistical analysis of silage quality indicators

Repetitions	Indicators											
	DM	protein	oil	cellulose	NFES	sugar	starch	ash	Ca	P	DP	EE
1	27.5	2.89	1.1	7.47	13.93	1.95	6.08	1.82	0.39	0.15	17.91	2.94
2	29.11	3.2	1.13	7.49	15.32	0.97	5.3	1.97	0.31	0.13	19.82	3.09
3	28.65	2.34	1.08	6.94	16.9	1.82	6.94	1.39	0.28	0.09	17.54	3.13
4	27.13	1.9	1.35	7.79	14.19	2.08	5.3	1.9	0.23	0.09	16.81	2.8
5	29.01	3.41	0.94	6.03	16.29	1.66	5.34	2.31	0.38	0.16	21.12	3.07
<b>Totality</b>	141.4	13.74	5.9	35.72	76.63	8.64	28.96	9.39	1.59	0.62	93.2	15.03
<b>Average readings</b>	28.28	2.748	1.18	7.144	15.326	1.73	5.79	1.878	0.318	0.124	18.64	3.006
<b>Root mean square deviation</b>	0.811	0.556	0.172	0.620	1.152	0.41	0.65	0.295	0.060	0.029	1.59	0.121

pressure of 60 kPa), which is higher by 30% in contrast to the silage density in trench.

The quality indicators of silage obtained by two technologies (vacuum and trench) are shown in Fig. 4, depicting each quality indicator in pairs (the left is for silage from vacuumized container; the right is for silage from trench) for visual comparison.

According to the analysis results, the nutrient and estimated metabolizable energy (ME) composition in each vacuum-packed sample compared to a trench sample exceeded: dry materials (DM) by 2.05%; protein more than by a factor of 1.47; nitrogen-free extractive substances (NFES) more than by 1.37; starch by 1.56; Ca by 1.83%; P more than by 2. Considering the other indicators which were not determined in percentage terms: digestible protein (DP) was increased by a factor of 1.24; feed unit by 1.31; exchange energy (EE) by 1.16. Furthermore, there were indicators that showed decrements: fat was decreased by a factor of 1.16; fibre by 1.21; sugar by 1.18; ash by 0.14%.

The reliability of silage quality study was achieved by conducting five repetitions for each analysis throughout the year. The error deviation was estimated by statistical analysis in order to ensure that the indicators of deviations are in confidence interval (Table 2). Furthermore, these results were supported by analysis of variance of data.

Vacuum-packed silage showed good sensory properties, such as yellow-green colour and the odour showed a clear gentle linear pattern of change like pickled vegetables. Considering the visual comparison (Fig. 4), the silage extracted from the flexible plastic container showed a brighter colour than the silage from trench, which was much darker. The indicators relevant for chemical analysis of the vacuum-packed silage suggest a good quality, which was achieved thanks to good sealing of the container for storage period and storing of the succus (juice) released during the compression process together with the silage mass inside the container. Silage succus in the silo trench flows out, resulting in the loss of valuable nutrients and deterioration of storage environment. The excess of DM by 2.05% in a flexible container is due to the fact that, in case of flexible container, sampling is performed in the middle part and moisture accumulates in the lower part of the

container; in case of trenches, the sampling is conducted in the lower part with high residual moisture. In addition to this, the DM values in the container and trenches are in accordance with the requirements given by the standard. Loss of dry matter in silage depends on quality of grinding; quality of compaction; sugar content, etc. Thanks to the high-quality compaction in the flexible container, the succus does not flow out. In a trench, the silage mass is squeezed and the succus leaks out into the ground, taking numerous components with it. Therefore, the indices of individual substances, such as protein, NFES, starch, Ca and P in a soft container turned out to be underestimated due to the succus preservation. However, DM values in container and trench are in accordance with the standards (Gerlach et al., 2013; Kristensen, 2010). The research results prove the benefits of silage preparation in a soft container with the possibility of transportation and storage (without the necessity of special structures) with a guarantee of its quality preservation. From an environmental point of view, silage storage in a soft container is also a way to avoid the loss of silage (due to decomposition after opening the traditional storage facility) and succus leakage into the ground.

### Conclusion

The research results for the technology of preparation and storage of silage in flexible containers using vacuuming showed that its utilization eliminates the majority of disadvantages typical for the classic methods (silage trench, etc.). The construction of special facilities and storage places is not required for its use. Compaction of the silage mass in flexible containers via vacuuming at a pressure of 60 kPa resulted in a density of 800–850 kg·m<sup>-3</sup>. This value is higher by 30% in contrast to the silage density prepared using the traditional method.

Comparative study of the quality indicators of silage obtained by the vacuuming technology and traditional method made it possible to establish an improvement in indicators in favour of the proposed method: dry matter was increased by 2.05%; ash by 0.14%; protein by a factor of 1.47, nitrogenous substances by 1.37; starch by 1.56; calcium by 1.83; phosphorus by 2; digestible protein by 1.24; fodder units by 1.31; exchange energy by 1.16.

After opening the container, its content with an average volume of 1 m<sup>3</sup> was fully used as animal feed (no losses from oxidation). After opening the trench, the free space in the silo caused oxidation in the surface, making the silage unusable. The method proposed showed the advantages of storing all silage volumes (30 m<sup>3</sup>) in separate containers for 2 years during the research.

## References

- ASPLUND, J. M. 1994. Principles of Protein Nutrition of Ruminants. Boca Raton, FL: CRC Press.
- BOYARSKY, L. G. 2001a. Feed Technology and Full-Fledged Feeding of Farm Animals. Series: Veterinary and Animal Husbandry. Rostov-on-Don: Phoenix. (In Russian: Tekhnologiya kormov i polnotsennoe kormlenie sel'skokhozyaistvennykh zivotnykh).
- BOYARSKY, L. G. 2001b. Feed Technology and Full-Fledged Feeding of Farm Animals. Rostov-on-Don: Phoenix. (In Russian: Kormovaya tekhnika i polnotsennoe kormlenie sel'skokhozyaistvennykh zivotnykh).
- ERDMAN, R. 1993. Silage fermentation characteristics affecting feed intake. In Proceedings of the National Silage Production Conference. Syracuse, New York, pp. 210–219.
- FEDERAL STANDARD R55986-2014. 2014. Silage from Green Plants. Technical conditions. Moscow: Standards. (In Russian: GOST R 55986-2014 Silos iz kormovykh rastenii. Obshchie tekhnicheskie usloviya).
- FEDERAL STANDARD RF53903-2010. 2010. Feed Corn. Specifications. (In Russian: GOST RF53903-2010 Kukuruza kormovaja. Tekhnicheskie usloviya).
- FEDERAL STANDARD RF23638-1990. 1990. Green plants silage. Specifications. (In Russian: GOST RF23638-1990 Silos iz zelenykh rastenij. Tekhnicheskie usloviya).
- FERRARETTO, L. F. – SHAVER, R. D. – LUCK, B. D. 2018. Silage review: Recent advances and future technologies for whole-plant and fractionated corn silage harvesting. In Journal of Dairy Science, vol. 101, no. 5, pp. 3937–3951.
- GERLACH, K. – ROß, F. – WEIß, K. – BÜSCHER, W. – SÜDEKUM, K. H. 2013. Changes in maize silage fermentation products during aerobic deterioration and effects on dry matter intake by goats. In Agricultural Food Science, vol. 22, no. 1, pp. 168–181.
- HARRISON, J. H. – BLAUWIEKEL, R. – STOKES, M. R. 1994. Fermentation and utilization of grass silage. In Journal of Dairy Science, vol. 77, no. 10, pp. 3209–3235.
- HOLMES, B. J. – MUCK, R. E. 2000. Preventing silage storage losses. Available at: <https://fyi.extension.wisc.edu/forage/files/2014/01/prevent-silage-storage7.pdf>
- JOHNSON, H. E. – MERRY, R. J. – DAVIES, D. R. – KELL, D. B. – THEODOROU, M. K. – GRIFFITH, G. W. 2005. Vacuum packing: model system for laboratory-scale silage fermentations. In Journal of Applied Microbiology, vol. 98, no. 1, pp. 106–113.
- JONES, R. 1998. Bridging the protein gap: Potential of forage crops for UK livestock production. In LYONS, T. P. – JACQUES, K. A. eds. Biotechnology in the Feed Industry. Nottingham, UK: Nottingham University Press, pp. 119–134.
- KALASHNIKOV, A. P. 2003. Norms and Diets for Feeding Farm Animals: A Reference Guide. Moscow: Nauka. (In Russian: Normy i ratsiony kormleniya sel'skokhozyaistvennykh zivotnykh: spravochnoe rukovodstvo).
- KARPENKO, V. D. 1974. Compaction of silage mass by tractors. In Mechanization and Electrification of Social Agriculture, no. 7, pp. 11–12. (In Russian: Uplotnenie silosuemoi massy traktorami).
- KAŽIMÍROVÁ, V. – KUBÍK, L. – MIHINA, Š. 2020. Evaluation of properties of pellets made of swine manure. In Acta Technologica Agriculturae, vol. 23, no. 3, pp. 137–143.
- KELLER, T. – NONN, H. – JEROCH, H. 1998. The effect of sealing and of additives on the fermentation characteristics and mould and yeast counts in stretch film wrapped big-bale lucerne silage. In Journal Archiv für Tierernaehrung, vol. 51, no. 1, pp. 63–75.
- KHAZIMOV, M. Zh. – KHAZIMOV, K. M. – URMASHEV, B. A. – TAZHIBAYEV, T. S. – SAGYNDYKOVA, Zh. B. 2018a. Intensification of the plant products drying process by improving solar dryer design. In Journal of Engineering Thermophysics, vol. 27, no. 4, pp. 580–592.
- KHAZIMOV, Z. M. – BORA, G. C. – KHAZIMOV, K. M. – KHAZIMOV, M. Z. – ULTANOVA, I. B. – NIYAZBAYEV, A. K. 2018b. Development of a dual action planting and mulching machine for vegetable seedlings. In Engineering in Agriculture, Environment and Food, vol. 11, no. 2, pp. 74–78.
- KHAZIMOV, M. Z. – KHAZIMOV, K. M. – BAZARBAYEVA, T. – URYMBAYEVA, A. A. – BORA, G. C. – NIYAZBAYEV, A. K. 2019. Mechanization of removal of the mulching film and flexible irrigation tape from the surface of the fields. In Eurasian Journal of BioSciences, vol. 13, no. 2 pp. 1251–1261.
- KHOKHRIN, S. N. 2002. Feeds and Feeding Animals. St. Petersburg: Lan. (In Russian: Korma i kormlenie zivotnykh).
- KOROTKEVICH, A. V. 1990. Technologies and Machines for Forage Preparation from Grasses and Silage Crops. Minsk: Urajay. (In Russian: Tekhnologii i mashiny dlya zagotovki kormov iz trav i silosnykh kul'tur).
- KRISTENSEN, N. B. – SLOTH, K. H. – HØJBERG, O. – SPLIID, N. H. – JENSEN, C. – THØGERSEN, R. 2010. Effects of microbial inoculants on corn silage fermentation, microbial contents, aerobic stability, and milk production under field conditions. In Journal of Dairy Science, vol. 93, no. 8, pp. 3764–3774.
- KUZMIN, P. A. – SHARIFULLINA, A. M. 2014. Ecological and physiological reaction of fibre flax on vegetation. In Life Science Journal, vol. 11, spec. no. 8, pp. 377–379.
- LIMIN KUNG, Jr. – SHAVER, R. D. – GRANT, R. J. – SCHMIDT, R. J. 2018. Silage review: Interpretation of chemical, microbial, and organoleptic components of silages. In Journal of Dairy Science, vol. 101, no. 5, pp. 4020–4033.
- MALAREV, V. – BOGDANOV, I. – SENCHILO, N. 2020. Algorithm for automatic compensation of voltage dips in power supply of industrial facilities. In Journal of Applied Engineering Science, vol. 18, no. 2, pp. 173–180.
- MCALLISTER, T. A. – HRISTOV, A. N. 1995. The basics of manufacturing high-quality silo. Available at: <https://www.yumpu.com/en/document/read/49887728/the-fundamentals-of-making-good-quality-silage>
- NEKRASHEVICH, V. F. – REVICH, Ya. L. – ANTONENKO, N. A. – NEKRASHEVICH, K. S. 2015. Block-vacuum compaction and storage of silo in soft evacuated blocks of synthetic films. In Bulletin of the Ryazan State Agrotechnological University named after P.A. Kostychev, no. 2, pp. 65–68. (In Russian: Blochno-vakuumnoe uplotnenie i khranenie silosa v myagkikh vakuumirovannykh blokakh iz sinteticheskikh plenok).
- NEKRASEVICH, V. F. – POPOV, A. S. – AFANASIEVA, K. S. 2017. The use of vacuum when compacting the silage mass in containers made of airtight film. In Bulletin of the Ulyanovsk Agricultural Academy, no. 3, pp. 159–162. (In Russian: Ispol'zovanie vakuuma pri uplotnenii silosuemoi massy v konteinerakh iz vozdukhonepronitsaemoi plenki).
- NEKRASHEVICH, V. – MAMONOV, R. – TORZHENOVA, T. – VOROBYOVA, I. – KHAZIMOV, M. 2020. Theory and practice of feed silage in containers made of airtight film. In BIO Web of Conferences, vol. 17.

- ORSIK, L. S. – REVYAKIN, E. L. 2008. Innovative technologies and complexes of machines for feed preparation and storage. Recommendations – M.: FGNU Rosinformagrotekh, 140 pp. (In Russian: Innovatsionnye tekhnologii i komplekсы mashin dlya zagotovki i khraneniya kormov).
- PATENT RU 193970, MPK A01F25/14: February 14, 2019. Container for Preparation and Storage of Ensilage Fodder.
- PATENT RU 2625480, MPK A23K3/02: October 5, 2016. Method of Preparation and Storage of Ensilage Fodder
- PATENT RK 33415, MPK A01F25/14: June 21, 2017. Package Set for Loading, Transporting, Vacuuming, Ensilage and Silo Storage.
- PATENT RK 33425, MPK F16K15/00: September 18, 2017. Valve for a Container Used in the Ensiling of Forages.
- RALH, T. W. – ONDARZA, M. B. 2008. Fermentation Analysis of Silage: Use and Interpretation. Forage Analysis as a Diagnostic Tool. Available at: <https://www.foragelab.com/Media/Fermentation-Silage-NFMP-Oct-2008.pdf>
- REVICH, Ya. L. – NEKRASEVICH, V. F. 2013. Ecological aspects of modern construction and operation of trench silos. In Materials of the International Scientific and Practical Conference. Moscow: FSBEI HPE MSUEM, pp. 262–270. (In Russian: Ekologicheskie aspekty sovremennogo stroitel'stva i ekspluatatsii transheinykh silosokhranilishch).
- SAGYNDYKOVA, Zh. B. – NEKRASHEVICH, V. F. – KHAZIMOV, M. Zh. – KHAZIMOV K. M. 2019a. Research of the polyethylene film of silo container under the influence of vacuum pressure. In Food, Ecology, Quality, vol. 2, pp. 158–161. (In Russian: Issledovanie polietilenovoi plenki konteynera dlya silosa pod deistviem vakuumetricheskogo davleniya).
- SAGYNDYKOVA, Zh. B. – NEKRASHEVICH, V. F. – KHAZIMOV, M. Zh. – KHAZIMOV K. M. 2019b. Chemical composition and nutritional value of silo vacuumized flexible container. In Industry and Agriculture, pp. 5–11. (In Russian: Khimicheskii sostav i pitatel'naya tsennost' silosa vakuumirovannogo v myagkom konteynere).
- TOKOVÁ, L. – IGÁZ, D. – AYDIN, E. – ČIMO, J. – HORÁK, J. 2020. The effect of fertilization on time domain reflectometry probe measurement accuracy in the field experiment in Slovakia. In Acta Technologica Agriculturae, vol. 23, no. 3, pp. 144–149.
- WARD, R. T. – ONDARZA, M. B. 2009. Fermentation Analysis of Silage: Use and Interpretation. Available at: <https://www.foragelab.com/Media/Fermentation-Silage-NFMP-Oct-2008.pdf>
- WOOLFORD, M. K. 1989. Microbiological Screening of Food Preservatives, Cold Sterilants and Specific Antimicrobial Agents as Potential Silage Additives. Series B. 14. New York: Marseille Dekker.
- YEMELYANOV, V. A. – NEDELKIN, A. A. – OLENEV, L. A. 2019. An object-oriented design of expert system software for evaluating the maintenance of lined equipment. Paper presented at the 2019 International Multi-Conference on Industrial Engineering and Modern Technologies, FarEastCon 2019.
- ZHUKOVSKYY, V. – ZHUKOVSKA, N. – VLASYUK, A. – SAFONYK, A. 2019. Method of forensic analysis for compromising carrier-lock algorithm on 3G modem firmware. Paper presented at the 2019 IEEE 2<sup>nd</sup> Ukraine Conference on Electrical and Computer Engineering, UKRCON 2019 – Proceedings, pp. 1179–1182.



Acta Technologica Agriculturae 2  
Nitra, Slovaca Universitas Agriculturae Nitriae, 2021, pp. 79–83

## COMPARISON OF ASH CONTENT IN VINEYARD PRUNING RESIDUES FROM MORAVIAN REGION

Martin ŠOTNAR<sup>1</sup>, Ivan VITÁZEK<sup>2\*</sup>, Jan MAREČEK<sup>1</sup>, Patrik BURG<sup>1</sup>, Eva KRČÁLOVÁ<sup>1</sup>,  
Kristína DARNADYOVÁ<sup>3</sup>, Vladimír MAŠÁN<sup>1</sup>

<sup>1</sup>Mendel University in Brno, Czech Republic

<sup>2</sup>Slovak University of Agriculture in Nitra, Slovak Republic

<sup>3</sup>Central Control and Testing Institute in Agriculture, Košice, Slovak Republic

This study presents the thermogravimetric analysis results of various samples of vineyard pruning residues from Rakvice Stand in the Moravian viticultural region. The samples of Welschreising, Grüner Veltliner, Gewürztraminer, and Palava were investigated in several heating-isotherm steps. Based on the results, three of these samples were found to not meet the conditions for the B category ( $\leq 3\%$ ) according to the EN ISO 17225 in terms of ash content. Only the Palava sample showed 2.76% of ash content in dry matter, which makes it suitable for technological applications, such as combustion in small residential biomass boilers. Considering the other samples, the results indicate that it is more appropriate to combust them as a part of mixture with added content of different wood biomasses.

**Keywords:** thermogravimetry; grapes; biomass; decomposition

Energy consumption is increasing worldwide, with estimated 30% increase in consumption by 2040 (IEA, 2017). For this reason and issues associated to it, the European Union Renewable Energy Directive (RED) 2009/28/EC was established, obliging the EU to increase the share of renewable energy in gross final energy consumption from 8.5% to 20% by 2030 (Gerritsen, 2015).

Utilization of targeted biomass (SRCs – short rotation crops, maize monocultures, etc.) brings significant environmental impacts, such as biodiversity change, land-use change, food availability, etc. (Gallagher, 2008; Popp et al., 2014; Genbach et al., 2018). A more suitable approach would be to utilize the secondary products from agriculture, forestry, and other activities as renewable energy sources. Such exploitation of these residue materials can bring environmental, economic and energy benefits (Spöttle et al., 2013; Dhaundiyal and Hanon, 2018). Furthermore, the costs arising due to processing of these residues can be compensated by the profit from the energy obtained. Pruning vineyard residues can be considered such a source. In addition to this, grapes are also profitable crops in the country (Alves et al., 2019). The residues of agricultural products, especially biomass by-products from vineyards, are used as a strategic fuel source of in many European countries (Beccali et al., 2009; Velazquez-Marti et al., 2011; Scarlat et al., 2011).

Burning of plant residue of this nature in an open fire is a worldwide and long-term bad practice. This is a fast and cheap method of processing large volumes of material residue, yet it is not environmentally friendly (Alves et al.,

2019); moreover, the emissions from this type of burning have negative impacts on air quality, human health, and environment (Chen et al., 2017; Zhao et al., 2017; Liu et al., 2018; Malaťák et al., 2020). Therefore, it is advisable to carry out the burning under controlled conditions in boilers. In order to facilitate the feeding of these materials prior combustion in boilers, they can be either pelletized or chipped (Holubčík et al., 2018; Hamedani et al., 2019).

The relatively high ash and moisture contents can cause issues to small residential biomass boilers (Zanetti et al., 2017). The yield of vineyard pruning residue material can reach up to approx.  $1 \text{ t} \cdot \text{ha}^{-1}$ , making it suitable for application in boilers under domestic conditions. However, Zanetti et al. (2017) measured ash content of vineyard pruning residues (3.3–5.5%) and compared it with biomass wood ash content (0.4%), coming to conclusion that these values can represent a limiting factor to proper operation of these types of boilers. Nevertheless, according to Spinelli et al. (2012), these materials can still be exploited under industrial conditions despite their high ash contents.

The aim of this study is to determine the contents of ash, moisture, and volatiles. These results, especially the ash content result, can be used in further development of the efficient technology for the purposes of combustion.

### Material and methods

For this study, the samples of vineyard pruning residues from Rakvice Stand in the Moravian viticultural region were used.

**Contact address:** Ivan Vitázek, Slovak University of Agriculture in Nitra, Faculty of Engineering, Department of Transport and Handling, Tr. Andreja Hlinku 2, 949 76 Nitra, Slovak Republic; e-mail: [ivan.vitazek@uniag.sk](mailto:ivan.vitazek@uniag.sk)



**Fig. 1** Apparatus for thermogravimetric experiments

Four different vine varieties were utilized for this experiment: Welschreising, Grüner Veltliner, Gewürztraminer, Palava; these samples were collected in area with average annual temperature of 9–10 °C. These samples were ground in the cutting mill Retsch SM 100 in order to obtain the sample particle size less than 1 mm.

For the purposes of thermogravimetric experiments, furnace Nabertherm L9/11/SW/P330 with Kern digital scales were used (Fig. 1). The measurements were carried out under the static air atmosphere conditions using the samples with mass ~10 g. For each sample, three or more experiments were performed, according to the reproducibility of the obtained results.

The experiments were performed in accordance with the STN ISO 1171. Table 1 shows the parameters during thermogravimetric measurement. These intervals allow the determination of moisture content, combustibility, and ash content.

Firstly, the samples were heated to 105 °C and dried for 120 min. in order to remove the moisture. Subsequently, the samples were heated to 500 °C, where the mass loss contributes to combustible volatiles. The last step was to heat the samples to 815 °C – after subjection to this

temperature for 60 min., the residues correspond to ash content. The proportions of particular components are calculated according to the following equations:

$$w = \frac{m_1 - m_2}{m_1} \cdot 100 \quad (1)$$

where:

$w$  – moisture content

$m_1$  – original sample weight

$m_2$  – dry matter weight

$$A' = \frac{m_3}{m_1} \cdot 100 \quad (2)$$

where:

$A'$  – sample ash content

$m_3$  – ash weight

$$p_{ps} = \frac{m_3}{m_2} \cdot 100 \quad (3)$$

where:

$p_{ps}$  – ash content in dry matter

$$h' = \frac{m_4}{m_1} \cdot 100 \quad (4)$$

where:

$h'$  – combustible content in the sample

$m_4$  – weight of combustible content

$$p_{hs} = \frac{m_4}{m_2} \cdot 100 \quad (5)$$

where:

$p_{hs}$  – weight of combustible content in dry matter

In order to determine these variables, the following standards were utilized: STN EN 15148; STN EN 14775; and STN ISO 1171.

## Results and discussion

The thermogravimetric analysis results (Fig. 2) show different behaviour of used biomasses from vineyards during heating, especially in the first phase, which corresponds to the release of moisture and adsorbed water. The mass loss during 175 and 250 minute of measurement corresponds to the main phase of decomposition (Ondro et al., 2018; Vitázek et al., 2019).

In certain cases, the main phase of decomposition is shifted to lower temperatures. This can be caused by the

**Table 1** Parameters obtained in thermogravimetric measurement

Interval	1	2	3	4	5	6
Time (min)	60	120	60	60	60	60
Temperature (°C)	20–105	105	105–500	500	500–815	815

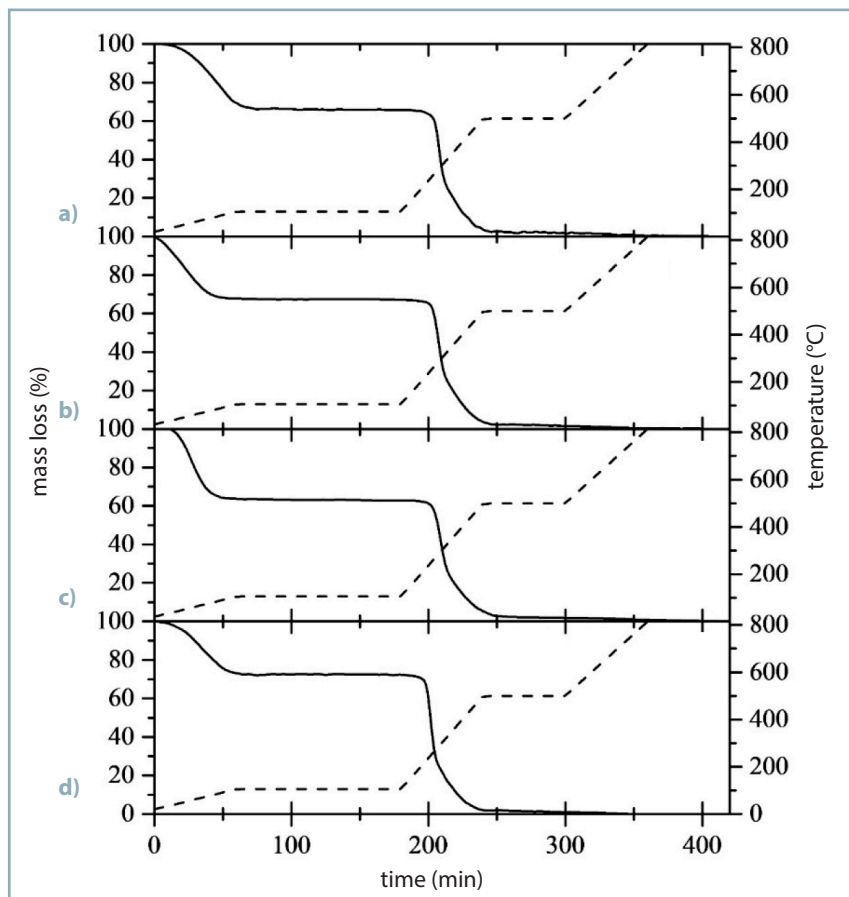


**Fig. 2** Thermogravimetric curves (solid lines) of used different grape varieties a) Palava, b) Welschreisling, c) Gewürztraminer, d) Grüner Veltliner (dashed lines characterize the temperature program)

weakest bond sites of hemicelluloses, since bond power and degradation rate may vary (Melcer et al., 1990). Considering the Grüner Veltliner sample, the concentration of weaker bonds was probably higher, which led to occurrence of thermal decomposition at lower temperatures in contrast to the other vineyard pruning residue samples. After the isotherm at 500 °C, there was no other process phase that could cause another mass loss of the sample.

On the basis of these thermogravimetric measurements, the moisture, combustible, and ash

contents were calculated according to Eqs 1–5, and the obtained values are listed in Table 2.

Table 2 provides the basic characteristics of pruning residues from vineyards. The moisture content ranged from 27.84% to 37.48%, the ash content ranged from 1.80% to 2.61%, the combustible matter content ranged from 60.25% to 69.55%, the ash content in the dry matter ranged from 2.76% to 3.62%, and the content of combustible matter in dry matter ranged from 96.37% to 97.24%.

Calorific value types of woody biomass have been studied often,

e.g. the articles by Burg et al. (2017) and Manzone et al. (2016), who presented 14 years of observational data, report the calorific values (Lower Heating Values, LHVs) of various samples of vineyard pruning residue of 18.2 MJ·kg<sup>-1</sup> and 17.96 MJ·kg<sup>-1</sup>, respectively. However, the ash content is also important due to the well-known fact that the energy content is inversely proportional to ash content (Picchi et al., 2018).

This value is important, because the EN ISO 17225 divides the solid fuels (wood chips) into various groups on the basis of this data. Parameters determined in thermogravimetric measurements (Table 1) show that there is no significant difference between the ash contents of individual samples. However, the Palava sample was the only sample that met prerequisites for inclusion to the B category. On the other hand, based on the measurements, the ash content in the rest of samples was higher than the limit for this category. Therefore, it can be concluded that the samples of Welschreisling, Grüner Veltliner, and Gewürztraminer can be mixed with other types of woody biomass in order to achieve the lower ash content in dry matter. On the contrary, Giorio et al. (2019) reported the ash content of 3.07–3.10%; however, this value strictly depends on grape variety. Consequently, for the technological purposes, it is better to combust the mixtures of different types of wood biomass.

It is well-known that the methods of processing vineyard pruning residues include composting and thermal composition. If the material is to be for combustion (e.g. as a mixture with another wood biomass), it is better to dry it before storage, since it was observed that it takes approx. two

**Table 2** Thermogravimetric measurement results

Biofuel	Parameter				
	$W$	$A'$	$h'$	$p_{ps}$	$p_{hs}$
<b>Welschreisling</b>	33.27 ± 1.40	2.045 ± 0.073	64.70 ± 1.47	3.0502 ± 0.18	96.95 ± 0.18
<b>Grüner Veltliner</b>	27.84 ± 1.49	2.61 ± 0.084	69.55 ± 1.41	3.62 ± 0.044	96.38 ± 0.044
<b>Gewürztraminer</b>	37.48 ± 1.76	2.27 ± 0.0012	60.25 ± 1.76	3.63 ± 0.11	96.37 ± 0.11
<b>Palava</b>	35.012 ± 0.12	1.80 ± 0.10	63.19 ± 0.24	2.76 ± 0.14	97.24 ± 0.14

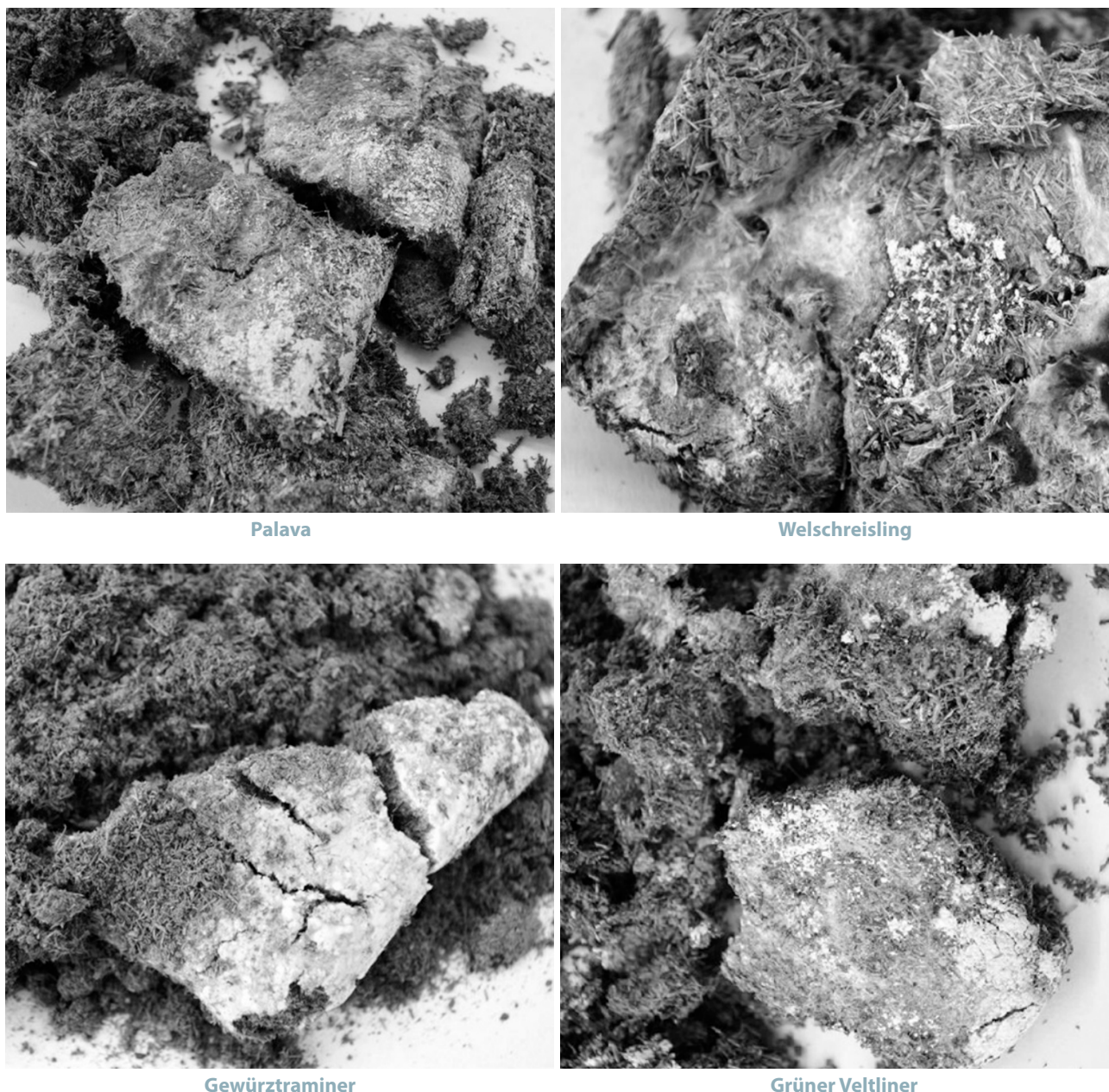


**Fig. 3** Mould on the ground samples of Palava, Welschreisling, Gewürztraminer and Grüner Veltliner after two weeks

weeks to form the mould on ground samples of vineyard pruning residues (Fig. 3).

### Conclusion

Majority of scientific studies are aimed to determine the calorific value of different types of vineyard pruning residues. However, considering the technological point of view, the ash content also represents a significant factor and it is important to take into account its potential negative impacts on small boilers. For this very reason, this study observes ash content and the parameters associated with it of various vineyard pruning residues by means of thermogravimetric analysis under static air atmosphere condition. The main results can be summarized as follows:

- The main thermal decomposition of samples occurs approximately in the same temperature range. However, this range was markedly shifted to the lower temperature in case of Grüner Veltliner sample, which is caused by the weaker bond sites of hemicelluloses.
- Considering all the samples of vineyard pruning residues from Rakvice Stand in the Moravian viticultural region, the lowest ash content in dry matter was observed in the Palava sample.
- The other samples did not meet the requirements for the B category determined by the EN ISO 17225.
- Based on the results, it can be concluded that it is better to combust the mixtures of different types of wood biomass for technological applications.

## References

- ALVES, C. A. – VICENTE, E. D. – EVTYUGINA, M. – VICENTE, A. – PIO, C. – AMADO, M. F. – MAHÍA, P. L. 2019. Gaseous and special particulate emissions from the open burning of wastes from tree pruning. In *Atmospheric Research*, vol. 226, pp. 110–121.
- BECCALI, M. – COLUMBA, P. – D'ALBERTI, V. – FRANZITA, V. 2009. Assessment of bioenergy potential in Sicily: A GIS-based support methodology. In *Biomass & Bioenergy*, vol. 33, pp. 79–87.
- BURG, P. – MAŠÁN, V. – ZEMÁNEK, P. – RUTKOWSKI, K. 2017. Review of energy potential of the wood biomass of orchards and vineyards in the Czech Republic. In *Research in Agricultural Engineering*, vol. 63, pp. 1–7.
- CHEN, J. – LI, C. – RISTOVSKI, Z. – MILIC, A. – GU, Y. – ISLAM, M. S. – WANG, S. – HAO, J. – ZHANG, H. – HE, C. – GUO, H. – FU, H. – MILJEVIC, B. – MORAWSKA, L. – THAI, P. – LAM, Y. F. – PEREIRA, G. – DING, A. – HUANG, X. – DUMKA, U. C. 2017. A review of biomass burning: emissions and impacts on air quality, health and climate in China. In *Science of the Total Environment*, vol. 579, pp. 1000–1034.
- DHAUNDIYAL, A. – HANON, M. M. 2018. Calculation of kinetic parameters of the thermal decomposition of residual waste of coniferous species: *Cedrus deodara*. In *Acta Technologica Agriculturae*, vol. 21, no. 2, pp. 75–80.
- EN ISO 17225: 2014 Solid biofuels – Fuel specifications and classes.
- GALLAGHER, E. 2008. The Gallagher Review of the Indirect Effects of Biofuels Production. Renew. Fuels Agency, London, UK, July.
- GENBACH, A. – JAMANKULOVA, N. – BELOEV, H. – LLIEV, L. 2018. Energy divider with insert for heating protection of fruit trees. In *Acta Technologica Agriculturae*, vol. 21, no. 1, pp. 8–13.
- GERRITSEN, M. 2015. Renewable energy policy in the European Union. Is there a firm foundation for the EU's 2030 renewable energy targets? In *European Policy Review*, vol. 1, pp. 3–30.
- GIORIO, Ch. – PIZZINI, S. – MARCHIORI, E. – PIAZZA, R. – GRIGOLATO, S. – ZANETTI, M. – CAVALLI, R. – SIMONCIN, M. – SOLDÀ, L. – BADOCCO, D. – TAPPARO, A. 2019. Sustainability of using vineyard pruning residues as an energy source: Combustion performances and environmental impact. In *Fuel*, vol. 243, pp. 371–380.
- HAMEDANI, S. R. – COLANTONI, A. – GALLUCCI, F. – SALERNO, M. – SILVESTRI, C. – VILLARINI, M. 2019. Comparative energy and environmental analysis of agro-pellet production from orchard woody biomass. In *Biomass & Bioenergy*, vol. 129, pp. 105334.
- HOLUBČÍK, M. – JANDAČKA, J. – KANTOVÁ, N. 2018. Impact of the wood geometric parameters on the particulate matter production in small heat source. In *AIP Conference Proceedings*, 2018–08–07, 2000 pp. ISSN 0094243X.
- INTERNATIONAL ENERGY AGENCY (IEA). 2017. World Energy Outlook 2017: A world in transformation. Available at: <http://www.iea.org/weo2017/> (accessed 27 February 2020).
- LIU, T. – MARLIER, M. E. – DEFRIES, R. S. – WESTERVELT, D. M. – XIA, K. R. – FIORE, A. M. – MICKLEY, L. J. – CUSWORTH, D. H. – MILLY, G. 2018. Seasonal impact of regional outdoor biomass burning on air pollution in three Indian cities: Delhi, Bengaluru, and Pune. In *Atmospheric Environment*, vol. 72, pp. 83–92.
- MALATÁK, J. – VELEBIL, J. – GENDEK, A. – TAMELOVÁ, B. 2020. Evaluation of CO and NO<sub>x</sub> emissions in real-life operating conditions of herbaceous biomass briquettes combustion. In *Acta Technologica Agriculturae*, vol. 23, no. 2, pp. 53–59.
- MANZONE, M. – PARAVIDINO, E. – BONIFACINO, G. – BALSARI, P. 2016. Biomass availability and quality produced by vineyard management during a period of 15 years. In *Renewable Energy*, vol. 99, pp. 465–471.
- MELCER, I. – MELCEROVÁ, A. – VOZÁR, M. 1990. Chemistry of Wood. Vysoká škola lesnícka a drevárska vo Zvolene, 220 pp. (In Slovak: *Chémia dreva*).
- ONDRO, T. – VITÁZEK, I. – HÚLAN, T. – LAWSON, M. K. – CSÁKI, Š. 2018. Non-isothermal kinetic analysis of the thermal decomposition of spruce wood in air atmosphere. In *Research in Agricultural Engineering*, vol. 64, no. 1, pp. 41–46.
- PICCHI, G. – LOMBARDINI, C. – PARI, L. – SPINELLI, R. 2018. Physical and chemical characteristics of renewable fuel obtained from pruning residues. In *Journal of Cleaner Production*, vol. 171, pp. 457–463.
- POPP, J. – LAKNER, Z. – HARANGIO-RÁKOS, M. – FÁRI, M. 2014. The effect of bioenergy expansion: food, energy, and environment. In *Renewable & Sustainable Energy Reviews*, vol. 32, pp. 559–578.
- SCARLAT, N. – BLUKDEA, V. – DALLEMAND J. F. 2011. Assessment of the availability of agricultural and forest residues for bioenergy production in Romania. In *Biomass & Bioenergy*, vol. 35, pp. 1995–2005.
- SPINELLI, R. – NATI, C. – PARI, L. – MESCALCHIN, E. – MAGAGNOTTI, N. 2012. Production and quality of biomass fuels from mechanized collection and processing of vineyard pruning residues. In *Applied Energy*, vol. 89, no. 1, pp. 374–379.
- SPÖTTLE, M. – ALBERICI, S. – TOOP, G. – PETERS, D. – GAMBA, L. – PING, S. – STEEN, H. – BELLEFLEUR, D. 2013. Low ILUC Potential of Wastes and Residues for Biofuels: Straw, Forestry Residues, UCO, Corn Cobs. *Ecofys: Utrecht, The Netherlands*, 168 pp.
- STN EN 14775: 2010. Solid biofuels. Determination of ash content.
- STN EN 15148: 2010. Solid biofuels. Determination of the content of volatile matter.
- STN ISO 1171: 2003. Solid mineral fuels. Determination of ash.
- VELAZQUEZ-MARTI, B. – FERNANDEZ-GONZALES, E. – LOPEZ-CORTEZ, I. – SALAZAR-HERNANDEZ, D. M. 2011. Quantification of the residual biomass obtained from pruning of trees in Mediterranean olive groves. In *Biomass & Bioenergy*, vol. 35, pp. 3208–3217.
- VITÁZEK, I. – ONDRO, T. – SUNITROVÁ, I. – MAJDAN, R. – ŠOTNAR, M. 2019. Thermoanalytical investigation of selected fuel during isothermal heating. In *Agronomy Research*, vol. 17, no. 6, pp. 2455–2459.
- ZANETTI, M. – BRANDELET, B. – MARINI, D. – SGARBOSSA, A. – GIORIO, Ch. – BADOCCO, D. – TAPPARO, A. – GRIGOLATO, S. – ROGAUME, C. – ROGAUME, Y. – CAVALLI, R. 2017. Vineyard pruning residues pellets for use in domestic appliances: a quality assessment according to the EN ISO 17225. In *Journal of Agricultural Engineering*, vol. 48, pp. 99–108.
- ZHAO, H. – ZHANG, X. – ZHANG, S. – CHEN, W. – TONG, D. Q. – XIU, A. 2017. Effects of agricultural biomass burning on regional haze in China: a review. In *Atmosphere*, vol. 8, pp. 88.



Acta Technologica Agriculturae 2  
Nitra, Slovaca Universitas Agriculturae Nitriae, 2021, pp. 84–91

## PERFORMANCE FEATURES OF TOOTH GEARING IN GEAR HYDRAULIC MACHINES

Yuri V. KULESHKOV<sup>1</sup>, Timofey V. RUDENKO<sup>1</sup>, Mikhailo V. KRASOTA<sup>1</sup>,  
Miroslav BOŠANSKÝ<sup>2\*</sup>, František TÓTH<sup>3</sup>

<sup>1</sup>Central Ukrainian National Technical University, Kropyvnytskyi, Ukraine

<sup>2</sup>Slovak University of Technology in Bratislava, Slovakia

<sup>3</sup>Slovak University of Agriculture in Nitra, Slovakia

The paper presented determines that the rotation velocities of gears and radii connecting the axes of rotation of the gears with the point of their teeth gearing are not equal with each other. It is explained by the relative slip of involute gear profiles during their rolling. This phenomenon will become a prerequisite for further development of creation of mathematical models in the context of theory of gear hydraulic machines. The models can explain a number of specific phenomena in the operation of gear hydraulic machines, such as pressure and input pulsations, dynamics of hydraulic oil in the cut-off plane, combined torque pulsations in gear hydraulic motors and others.

**Keywords:** gear hydraulic motor; involute tooth gearing; gearing ratio; slip of involute surfaces

Widespread application of gear hydraulic machines in hydraulic systems is a result of simplicity and compactness of their design, reliability, low work content and low manufacturing costs, ease of maintenance, and the possibility of their direct connection to drive mechanisms (Tulík et al., 2017; Kučera and Aleš, 2017; Tkáč et al., 2017). Despite the long history of the development of gear hydraulic machines and a great number of publications in relation to this issue (Casoli et al., 2008; Huang and Chen, 2008), certain features of their operation remain unexplained, indicating that there is still scientific space for further theoretical and experimental studies in order to improve their technical parameters. For example, Wang et al. (2011) addressed the issue of reducing the gear noise and increasing the mechanical efficiency by optimizing their design. Stryczek et al. (2019) investigated the possibilities of application of trochoidal gearing and solved the issue of reducing the contact pressures by optimizing their geometric parameters. Furthermore, Gamez-Montero et al. (2018) developed a method aimed at creating the basic rules in design of trochoidal gear pumps. Ivanovic et al. (2012) built a mathematical model determining the minimum backlash in gearing in relation to the instantaneous gear ratio and examining the influence of geometric parameters of gearing in order to achieve quiet and accurate operation. Zhou et al. (2017) addressed the issue of bearing optimization. Considering the aforementioned, it is clear that gear pumps are still the subject of research by scientists around the world. Researchers are still unable to explain and determine the causal relationship of multiple operation features of gear hydraulic machines, including formation of and changes in the geometric parameters of the cut-off

plane, decrease in the displacement in contrast to expected value, the causes of the inlet pulsation and pressure, and the pulsating change in the gear hydraulic motor torque.

Presented paper describes a theoretical contribution aiming to further develop the mathematical models of movement of hydraulic oils in the pump body in relation to the pulsation of pressure and oil supply, and changes in bearing load.

### Material and methods

The research results presented can become the basis for further development of the theory of gear hydraulic machines. The main directions of these theoretical studies are as follows:

- study of the input nature taking into account the aforementioned features in the operation of gear hydraulic machines;
- study of the features of changes in the cut-off plane and hydrodynamic processes occurring in it;
- study of the inlet pulsation and pressure;
- study of the load dynamics in pump bearings and motor;
- study of the dynamics of torque developed by a gear hydraulic motor;
- study of the dynamics of power developed by a gear hydraulic motor.

The research objectives include:

- establishing the relationship between the pivot angle of driving gear  $\phi_1$  and rotation angles  $\chi_1, \chi_2$  of radii  $\rho_1, \rho_2$  connecting the axes of rotation of gears  $O_1$  and  $O_2$  with

**Contact address:** Miroslav Bošanský, Slovak University of Technology in Bratislava, Faculty of Mechanical Engineering, Institute of Transport Technology and Designing, Námestie Slobody 17, 812 31, Bratislava 1, Slovakia; e-mail: [miroslav.bosansky@stuba.sk](mailto:miroslav.bosansky@stuba.sk)

gearing point  $T$ , taking into account the slip of involute teeth profiles of the gears, which are relative to each other;

- identification of the patterns of change in the lengths of radii  $\rho_1, \rho_2$  from the parameter  $\phi_1$ .

### Results and discussion

As a geometric interpretation of tooth gearing, the gear teeth are visualized in a form of system of plates  $O_1A_1, O_2A_2, O_1T$  and  $O_2T$  (Figs 1–4). This method was also used by other researchers (Kuleshkov et al., 2010). However, an approach to describe the hydraulic oil flow dependence on the geometric parameters and movement features of gears is used for the first time.

Fig. 1 presents tooth-gearing diagram of a gear hydraulic machine when a new pair of teeth comes into gearing. Fig. 2 presents a gearing diagram at the current moment of time. Fig. 3 shows the gearing diagram when the teeth are in the contact point, and Fig. 4 depicts the gearing diagram when the first pair of teeth comes out of gearing.

While developing the suggested mathematical model, for the reference point purposes, the radius  $OM$  was selected to determine the pivot angles of the driving gear elements and the radius  $ON$  of the driven gear.

For the driving gear, the point  $O_1$  is the centre of its rotation. At the same time, for a positive direction, the rotation of the radius is clockwise.

For the driven gear, the point  $O_2$  is the centre of its rotation; for the positive direction, the rotation of the radius is taken counter-clockwise.

The reference system is selected in such a way that the pivot angles of the driving and driven gears  $\phi_1$  and  $\phi_2$  from the beginning to the end of the tooth gearing (Figs 1–4) will be positive despite the fact that the gears rotate in opposite directions. This is because the volume of hydraulic oil is a scalar quantity and can only be positive.

Here is the description of the proposed geometric model of tooth gearing of a gear hydraulic machine.

In Figs 1–4, the following gear elements and their relationships are presented:  $MN$  – teeth gearing line;  $P$  – contact point;  $\alpha_w$  – gearing angle;  $r_{a1}$  – addendum circle radius;  $\rho_1,$

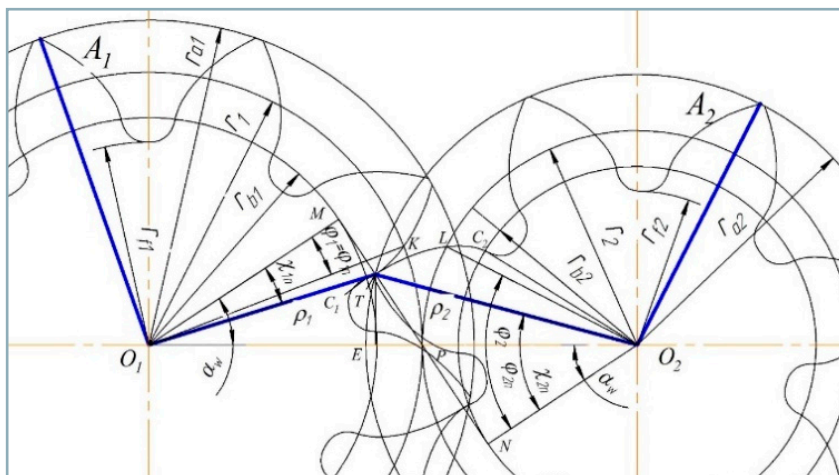


Fig. 1 Diagram at instance of new pair of teeth coming into gearing

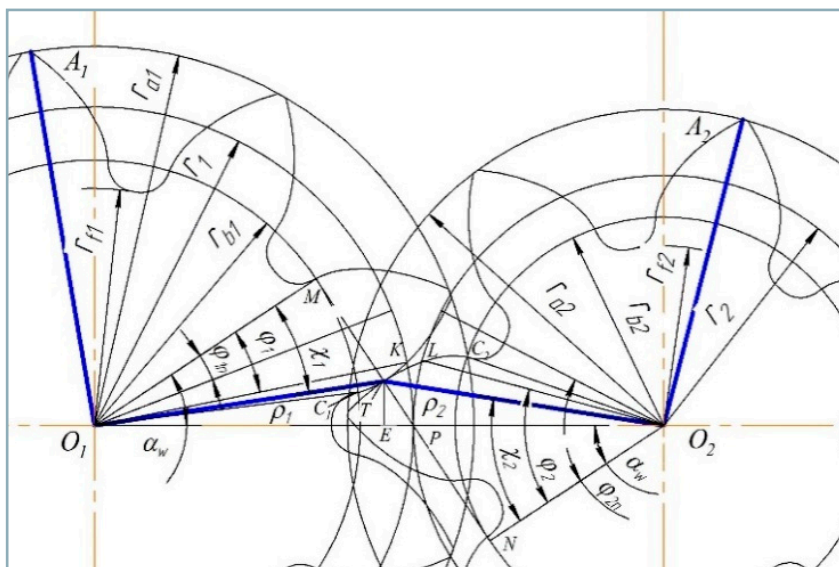


Fig. 2 Diagram of gearing elements position in real time

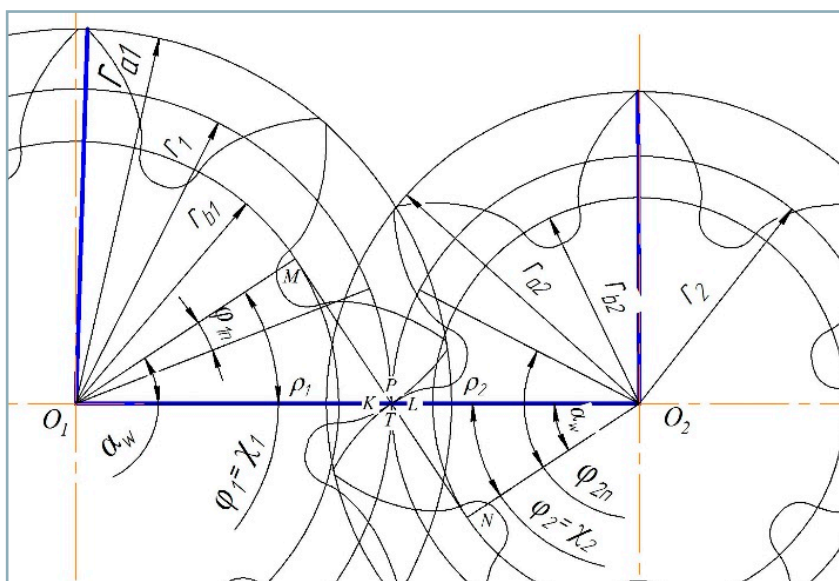


Fig. 3 Diagram of teeth position at contact point

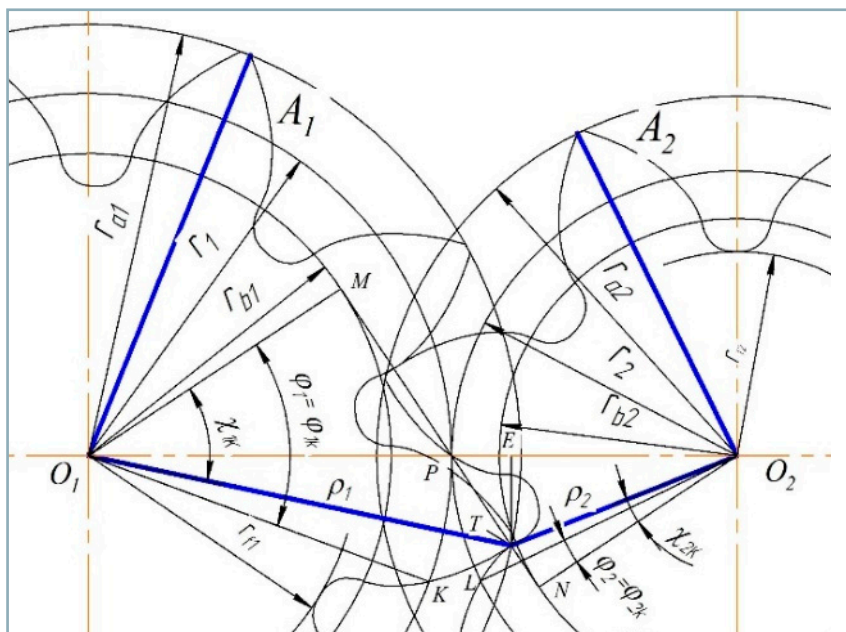


Fig. 4 Diagram at the instance when the first pair of teeth are coming out of gearing

Further rotation observation of these radii in Fig. 2 indicates that the differences in angles  $\chi_1 - \phi_1$  and  $\chi_2 - \phi_2$  decreased. Fig. 3 depicts the instance when the points  $K$ , and  $T$  and  $L$  and  $T$  simultaneously reach the gearing point  $P$ . In this case, the radii  $O_1K$  and  $\rho_1$ , and the radii  $O_2L$  and  $\rho_2$  coincide and lie on the centre line, and the differences in angles are  $\chi_1 - \phi_1 = 0$  and  $\chi_2 - \phi_2 = 0$ . This suggests that the angular rotation velocity of radii  $O_1K$  and  $O_2L$  is higher than the angular rotation velocity of radii  $\rho_1$  and  $\rho_2$ , which can be explained by the slip of involute profiles of gear teeth. With further rotation of gears, this trend continues (Fig. 4).

In this context, the aforementioned feature of gear operation of a gear hydraulic machine was not reflected in scientific works (Vacca and Guidetti, 2011). It should be noted that similar approach for developing a mathematical model for the input in gear pump was taken by other researchers. However, the initial assumptions associated with the fact that the angle of rotation of the radii  $\rho_1$  and  $\rho_2$  is rigidly connected to the angle of rotation of the driving gear  $\phi_1$  and the driven gear  $\phi_2$  are erroneous.

There is a relationship between the angle of rotation of the driving gear  $\phi_1$  and the angles of rotation of the radii  $\rho_1$  and  $\rho_2$ . Such a relationship can be obtained based on the definition of involute (Artobolevsky, 1988).

Based on the diagrams (Figs 1–4), for the driving gear, it is possible to give the expression taking into account the concept of the angle involute as follows (Artobolevsky, 1988):

$$\chi_1 = \phi_1 + inv \alpha_w - inv \chi_1 \quad (2)$$

After definition of involute  $inv x = \text{tg } x - x$ , after adjusting:

$$\chi_1 = \text{arctg} (\phi_1 + \text{tg } \alpha_w - \alpha_w) \quad (3)$$

Alternatively:

$$\phi_1 = \text{tg } \chi_1 - \text{tg } \alpha_w + \alpha_w \quad (4)$$

Similarly, the dependence between angles  $\chi_2$  and  $\phi_2$  is created:

$$\chi_2 = \phi_2 - inv \chi_2 + inv \alpha_w \quad (5)$$

$\rho_2$  – radii from the centres of rotation of gears  $O_1$  and  $O_2$  to the current point  $T$  of the gearing of involute profiles on the gearing line  $MN$ ;  $x$  – distance from the contact point  $P$  to the gearing point of teeth  $T$ ;  $O_1C_1$ ;  $O_2C_2$  – radii from the centre of rotation of gears to the intersection points of base circles with involute profiles;  $TE$  – height of the triangle  $O_1O_2T$ ;  $r_{b1}$ ,  $r_{b2}$  – radii of base circles;  $r_1$ ,  $r_2$  – radii of pitch circles;  $r_{f1}$ ,  $r_{f2}$  – radii of dedendum circles;  $O_1K = r_1$ ,  $O_2L = r_2$  – radii from the rotation centres of gears rolling over each other;  $\phi_1$ ,  $\phi_2$  – current pivot angles of the driving and driven gears at measuring reference point from the radii  $OM$  for the driving gear and from the radii  $ON$  for the driven gear.

There is a dependence between the increase in pivot angle of the driving gear  $\Delta\phi_1$  and increase in pivot angle of the driven gear  $\Delta\phi_2$ :

$$\Delta\phi_2 = \Delta\phi_1 / i \quad (1)$$

where:

$i$  – gear ratio

$i = z_2/z_1 = r_2/r_1 = \omega_1/\omega_2 = n_1/n_2$

$z_1, z_2$  – number of teeth of the driving and driven gears

$\phi_{1n}$ ,  $\phi_{2n}$  and  $\phi_{1k}$ ,  $\phi_{2k}$  – start and end pivot angles of the driving and driven gears at the beginning and end of tooth gearing by counting from radii  $OM$  for the driving gear and from radii  $ON$  for the driven gear

$\chi_{1n}$ ,  $\chi_{2n}$  and  $\chi_{1k}$ ,  $\chi_{2k}$  – start and end pivot angles of the radii  $\rho_1$ ,  $\rho_2$

It should be taken into account that the driven gear rotates in the opposite direction relative to the driving gear and the angular coordinates of turning of the driven and driving gears have different reference points. This will be taken into consideration later.

Using gearing diagrams presented in Figs 1–4, it is possible to demonstrate the differences in rotational motion of the radii  $O_1K$  and  $O_2L$ , and the radii  $\rho_1$  and  $\rho_2$ . As it can be seen in Figs 1–4, the radii  $O_1K$  and  $O_2L$  are directly related to the pitch circle and move together with the gears without slip. The radii  $\rho_1$  and  $\rho_2$  related to the gearing point also participate in the rotational motion with the slip of involute gear profiles. This is the difference in motion of these radii.

Fig. 1 shows the gearing beginning; the radius  $O_1K$  is rotated relative to the radius  $O_1M$  by angle  $\phi_{1n}$ , and the radius  $\rho_1$  is rotated by the angle  $\chi_{1n}$ . Accordingly, for the driven gear, the radius  $O_2L$  is rotated relative to the radius  $O_1N$  by angle  $\phi_{2n}$ , and the radius  $\rho_2$  is rotated by angle  $\chi_{2n}$ . In its rotation, the radius  $\rho_1$  is ahead of the radius  $O_1K$  and the difference in the angles of their rotation is  $\chi_{1n} - \phi_{1n}$ . Similarly, the radius  $\rho_2$  is ahead of the radius  $O_2L$  in its rotation and the difference in the angles of rotation is  $\chi_{2n} - \phi_{2n}$ .

$$\chi_2 = \arctg(\phi_2 + \operatorname{tg} \alpha_w - \alpha_w) \text{ or } \chi_2 = \arctg(\phi_2 + \operatorname{inv} \alpha_w) \quad (6)$$

$$\phi_2 = \operatorname{tg} \chi_2 - \operatorname{tg} \alpha_w + \alpha_w \text{ or } \phi_2 = \operatorname{tg} \chi_2 - \operatorname{inv} \alpha_w \quad (7)$$

Dependence of the angle  $\chi_2$  (4) on the variable  $\phi_2$  was obtained, which is inconvenient. Let us get the dependence of angle  $\chi_2$  on the variable  $\phi_1$ , i.e., the dependence  $\chi_2(\phi_1)$ . It is possible to use the concept of gearing ratio. Using Eq. (1) and Figs 1 – 4, one can see that:

$$\angle LO_2P = \angle KO_1P/i \quad (8)$$

$$\angle KO_1P = \alpha_w - \phi_1 \quad (9)$$

$$\phi_2 = \alpha_w + \angle LO_2P \quad (10)$$

Subsequently, taking into account Eqs (8) and (9), one gets:

$$\phi_2(\phi_1) = \alpha_w + (\alpha_w - \phi_1)/i \quad (11)$$

for the gearing with the same number of teeth ( $i = 1$ ), leading to:

$$\phi_2(\phi_1) = 2\alpha_w - \phi_1 \quad (12)$$

Then, the dependence in Eq. (6) can be presented in the following way:

$$\chi_2(\phi_1) = \arctg[(\alpha_w - \phi_1)/i + \operatorname{tg} \alpha_w]$$

$$\chi_2(\phi_1) = \arctg[\alpha_w + (\alpha_w - \phi_1)/i + \operatorname{inv} \alpha_w] \quad (13)$$

For the gears with the same number of teeth  $i = 1$  and the dependence (13), one gets:

$$\chi_2(\phi_1) = \arctg(\alpha_w - \phi_1 + \operatorname{tg} \alpha_w)$$

$$\text{or } \chi_2(\phi_1) = \arctg[2\alpha_w - \phi_1 + \operatorname{inv} \alpha_w] \quad (14)$$

The dependences of pivot angles  $\chi_1, \chi_2$  of the radii  $\rho_1, \rho_2$  on the position of gearing point  $T$  on the gearing line  $MN$  can be useful. This is determined by the distance  $x$  of point  $T$  from the gearing point  $P$ . From orthographic  $\triangle MO_1T$  in Figs 1 and 2, it is possible to write:

$$\chi_1 = \arctg(MT/r_{b1}) \quad (15)$$

On the other hand, from orthographic  $\triangle MO_1P$  (Figs 1 and 2), it is also possible to write:

$$MT = r_{b1} \operatorname{tg} \alpha_w - TP = r_{b1} \operatorname{tg} \alpha_w - x \quad (16)$$

By substituting the value  $MT$  from Eq. (16) in Eq. (15), one gets the expression for the angle  $\chi_1$  from  $x$ :

$$\chi_1 = \arctg((r_{b1} \operatorname{tg} \alpha_w - x)/r_{b1}) \quad (17)$$

By substituting Eq. (17) in Eq. (4), one gets the dependence of angle  $\phi_1$  on  $x$ :

$$\phi_1 = \alpha_w - x/r_{b1} \quad (18)$$

Furthermore, it is possible to get the dependence of the driven gear pivot angle  $\phi_2$  on  $x$ .

From orthographic  $\triangle NO_2T$  (Fig. 1, 2), it is possible to write  $NT = r_{b2} \operatorname{tg} \alpha_w + x$  and:

$$\operatorname{tg} \chi_2 = NT/r_{b2} \quad (19)$$

By applying Eq. (19), one gets:

$$\chi_2 = \arctg(NT/r_{b2}) \quad (20)$$

After adjustments, there is:

$$\chi_2 = \arctg((r_{b2} \operatorname{tg} \alpha_w + x)/r_{b2}) \quad (21)$$

By substituting Eq. (21) in Eq. (6), one gets the driven gear pivot angle dependence on  $x$ :

$$\phi_2 = \alpha_w + x/r_{b2} \quad (22)$$

It is possible to get inverse dependences from Eqs (18) and (21):

$$x = r_{b1}(\alpha_w - \phi_1) \quad (23)$$

$$x = r_{b2}(\phi_2 - \alpha_w) \quad (24)$$

Dependence (24) with the help of  $\phi_1$ :

$$x = r_{b2}(\alpha_w - \phi_1)/i \quad (25)$$

The graphs of the studied dependencies were plotted for gears with various parameters and calculated on the basis of pumps NSH-32 UK, which is the most mass-manufactured type in Ukraine. The parameters of the studied NSH-32 UK gearing are presented in Table 1.

Next, the range of argument  $\phi_1$  was defined. Based on the geometric model of hydraulic oil input shown (Figs 1–4), it can be argued that the variation range of the argument  $\phi_1$  for the gearing cycle of one pair of teeth can be defined as:

$$\phi_1 = [(\alpha_w - \pi \cdot \varepsilon/z_1); (\alpha_w + \pi \cdot \varepsilon/z_1)] \quad (26)$$

$$\phi_2 = [(\alpha_w + \pi \cdot \varepsilon/z_2); (\alpha_w - \pi \cdot \varepsilon/z_2)] \quad (27)$$

where:

$\varepsilon$  – coefficient of teeth overlaps in gearing

The limits of the changes in pivot angles of the driving and driven gears for tooth gearing with different parameters are presented in Table 2.

The pivot angles of driving and driven gears relative to the radii  $O_1M$  and  $O_2N$ , and alternatively, (Figs 1–4) will have the following form:

$$\phi_{1n} = \alpha_w - \pi \cdot \varepsilon/z_1 \quad (28)$$

$$\phi_{1k} = \alpha_w + \pi \cdot \varepsilon/z_1 \quad (29)$$

**Table 1** Technical parameters of tooth gearing in the pumps of NSH-32 UK type

Parameters	Parameter values for the number of teeth				
	$z_1 = z_2 = 8$	$z_1 = 9$	$z_2 = 7$	$z_1 = 7$	$z_2 = 9$
Number of gear teeth $z$	8	$z_1 = 9$	$z_2 = 7$	$z_1 = 7$	$z_2 = 9$
Gearing module $m$ (mm)	5				
Angle of base profile $\alpha$	20°				
Diameter of base circle $d_b$ (mm)	37.588	$db_1 = 42.3$	$db_2 = 32.8$	$db_1 = 32.38$	$db_2 = 42.49$
Addendum diameter $d_a$ (mm)	55.0	$d_{a1} = 60$	$d_{a1} = 50$	$d_{a1} = 50$	$d_{a2} = 60$
Angle of tooth gearing $\alpha_w$	33.355°				
Centre distance $\alpha_w$ (mm)	45.0				
Width of tooth $S_a$ (mm)	1.0				
Length of the bigger axis of the gear pump $G$ (mm)	100.0				
Overlap coefficient of tooth gearing $\varepsilon$	1.044	1.030		1.032	

**Table 2** Intervals of pivot angle changes of the driving and driven gears and the radii

Gearing parameters	Interval of angle changes	
	driving and driven gears	radii $\rho_1$ and $\rho_2$
$z_{1,2} = 8, \varepsilon = 1.044$	$\phi_1 \in [9.86^\circ; 56.84^\circ]$ $\phi_2 \in [56.84^\circ; 9.86^\circ]$	$\chi_1 \in [13.936^\circ; 46.886^\circ]$ $\chi_2 \in [46.886^\circ; 13.936^\circ]$
$z_1 = 9, z_1 = 7, \varepsilon = 1.030$	$\phi_1 \in [12.75^\circ; 53.95^\circ]$ $\phi_2 \in [59.836^\circ; 6.864^\circ]$	$\chi_1 \in [16.695^\circ; 45.502^\circ]$ $\chi_2 \in [48.25^\circ; 11.082^\circ]$
$z_1 = 7, z_2 = 9, \varepsilon = 1.032$	$\phi_1 \in [6.813^\circ; 59.887^\circ]$ $\phi_2 \in [53.99^\circ; 12.71^\circ]$	$\chi_1 \in [11.032^\circ; 48.272^\circ]$ $\chi_2 \in [45.521^\circ; 16.588^\circ]$

$$\phi_{2n} = \alpha_w + \pi \cdot \varepsilon / z_2 \quad (30)$$

$$\phi_{2k} = \alpha_w - \pi \cdot \varepsilon / z_2 \quad (31)$$

Alternatively:

$$\chi_{1n} = \arctg(\tg \alpha_w - \pi \cdot \varepsilon / z_1) \quad (32)$$

$$\chi_{1k} = \arctg(\tg \alpha_w + \pi \cdot \varepsilon / z_1) \quad (33)$$

$$\chi_{2n} = \arctg(\tg \alpha_w + \pi \cdot \varepsilon / z_2) \quad (34)$$

$$\chi_{2k} = \arctg(\tg \alpha_w - \pi \cdot \varepsilon / z_2) \quad (35)$$

Next, the length dependences of radii  $\rho_1$  and  $\rho_2$  on the gearing point position on the gearing line  $MN$  and on the driving gear rotation angle  $\phi$  were found. This position can be determined by the linear coordinate on the gearing line  $MN$  (Kuleshkov et al., 2010; Kuleshkov et al., 2009).

Using Figs 1–4, the Pythagorean theorem is applied:

$$\rho_{1,2}^2 = (r_{b1,2} \tg \alpha_w - x)^2 + r_{b1,2}^2 \quad (36)$$

After certain adjustments, one gets:

$$\rho_1^2 = (r_{b1} \tg \alpha_w - r_{b1} (\alpha_w - \phi_1))^2 + r_{b1}^2 \quad (37)$$

Similarly, in Figs 1–4, it is possible to see that:

$$\rho_2^2 = (r_{b2} \tg \alpha_w + r_{b2} (\phi_2 - \alpha_w))^2 + r_{b2}^2 \quad (38)$$

Alternatively:

$$\rho_1 = r_{b1} \sqrt{(\tg \alpha_w - \alpha_w + \phi_1)^2 + 1} \quad (39)$$

$$\rho_2 = r_{b2} \sqrt{(\tg \alpha_w + \phi_2 - \alpha_w)^2 + 1} \quad (40)$$

Eq. (40) can be re-written in relation to  $\phi_1$  taking into account Eq. (14) in the following form:

$$\rho_2 = r_{b2} \sqrt{(\tg \alpha_w + (\alpha_w - \phi_1) / i)^2 + 1} \quad (41)$$

Ultimately, dependences for determining the radii  $\rho_1$  and  $\rho_2$  and their rotation angles  $\chi_1$  and  $\chi_2$  were obtained. It is often necessary to have dependencies that would reflect the relationship between the radii  $\rho_1$  and  $\rho_2$  and the angles of their rotation  $\chi_1$  and  $\chi_2$ . For these purposes, these dependencies were obtained in a different form.

From the right triangle  $\triangle O_1MT$  and triangle  $\triangle O_2NT$ , one gets:

$$\rho_{1,2} = r_{b1,2} / \cos \chi_{1,2} \quad (42)$$

Next, it was necessary to define a different form of expressions for the lengths and angles of rotation  $\chi_1$  and  $\chi_2$  of the radii  $\rho_1$  and  $\rho_2$ . Furthermore, by determining the length of the radii  $\rho_1$  and  $\rho_2$ , it is possible to find the angles of their rotation  $\chi_1$  and  $\chi_2$  in the form:

$$\chi_{1,2} = \arccos (r_{b1,2}/\rho_{1,2}) \tag{43}$$

The obtained expressions for tooth gearings were indicated with the number of teeth  $z_{1,2} = 8; z_1 = 9, z_2 = 7;$  and  $z_1 = 7, z_2 = 9.$

In certain cases, it is more convenient to use a different reference system, i.e., from the longitudinal axis of the gear

hydraulic machine  $O_1O_2$ . In this case, when the driving gear is rotated clockwise, the angle  $\phi_1$  will take negative values in the direction from the axis  $O_1O_2$  up, and it will take positive values in the direction from the axis down. The dependences of the angles  $\chi_1$  and  $\chi_2$  on the parameter  $\phi_1$  take the following form:

$$\chi_1 = \alpha_w - \arctg (\tg \alpha_w - \phi_1) \tag{44}$$

$$\chi_2 = \arctg (\phi_1/i + \tg \alpha_w) - \alpha_w \tag{45}$$

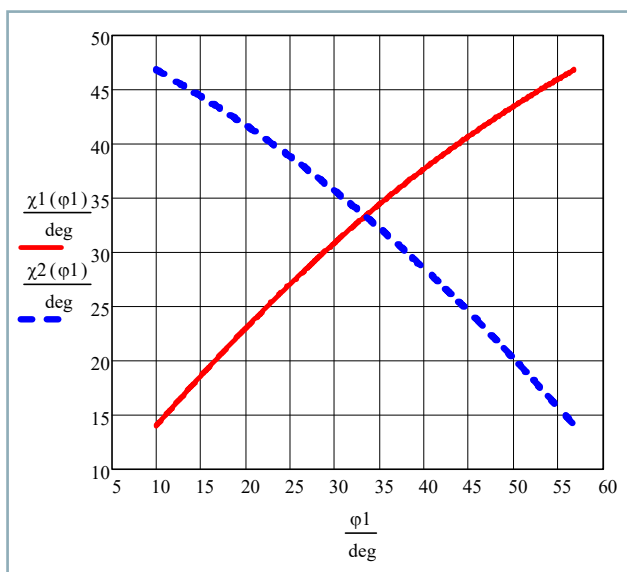


**Fig. 5** Dependences of the angles  $\chi_{1,2}(\phi)$  of the radius  $\rho_{1,2}$  on the driving gear rotation angle  $\phi_1$  with teeth number  $z_1 = z_2 = 8$

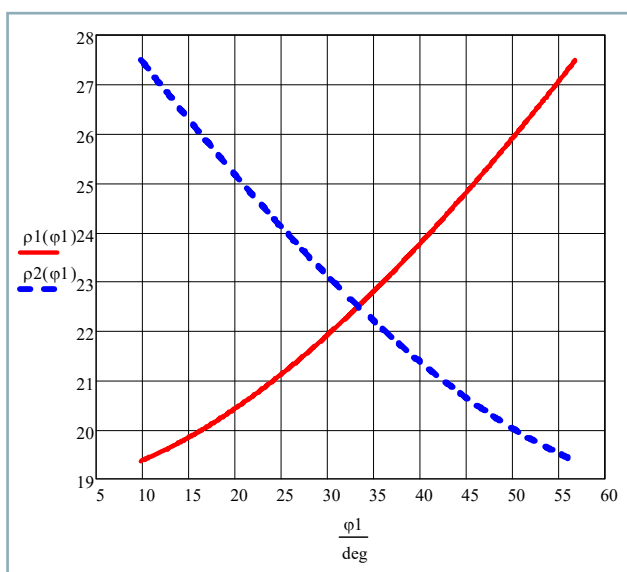


**Fig. 6** Dependences of the lengths of radii  $\rho_1$  and  $\rho_2$  on the driving gear rotation angle  $\phi_1$  with the teeth number  $z_1 = z_2 = 8$

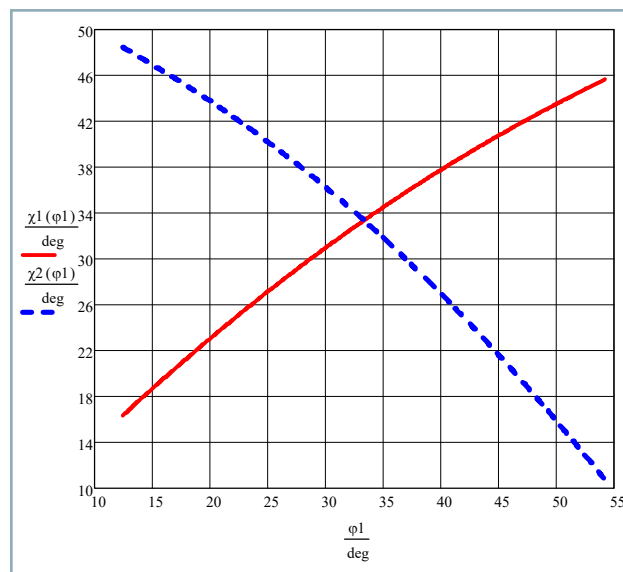


**Fig. 7** Dependences of the rotation angles  $\chi_{1,2}(\phi)$  of radius  $\rho_{1,2}$  on the driving gear rotation angle  $\phi_1$  with teeth number  $z_1 = 9, z_2 = 7$

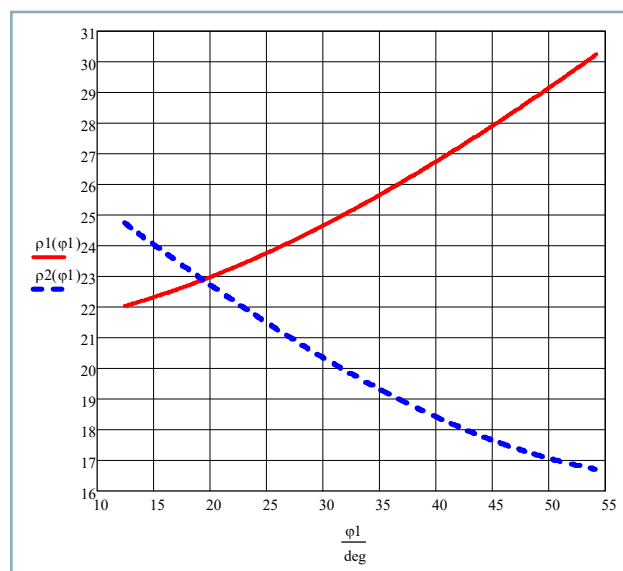


**Fig. 8** Dependences of the lengths of radii  $\rho_{1,2}$  on the driving gear rotation angle  $\phi_1$  with teeth number  $z_1 = 9, z_2 = 7$

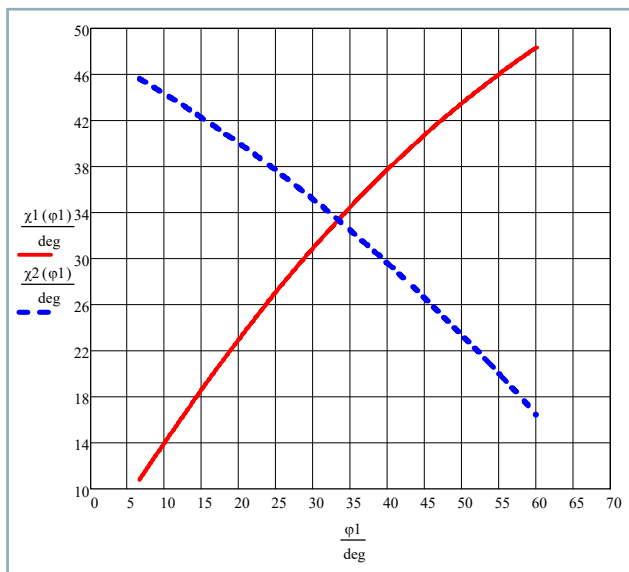


**Fig. 9** Dependences of the rotation angles  $\chi_{1,2}(\phi)$  of radius  $\rho_{1,2}$  of the driving gear  $\phi_1$  with teeth number  $z_1 = 7, z_2 = 9$

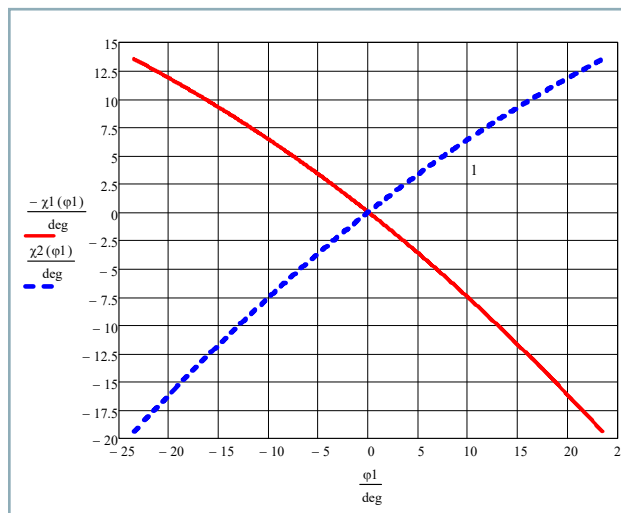


**Fig. 11** Dependences of the rotation angles  $\chi_{1,2}(\phi)$  of the radius  $\rho_{1,2}$  on the driving gear rotation angle  $\phi_1$  with teeth number  $z_{1,2} = 8$  in the reference system from the axis  $O_1O_2$

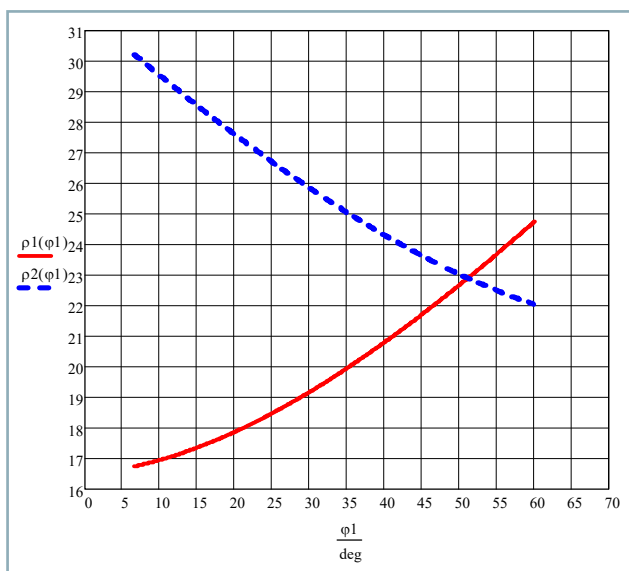


**Fig. 10** Dependences of the lengths of radii  $\rho_{1,2}$  on the driving gear rotation angle  $\phi_1$  with teeth number  $z_1 = 7, z_2 = 9$

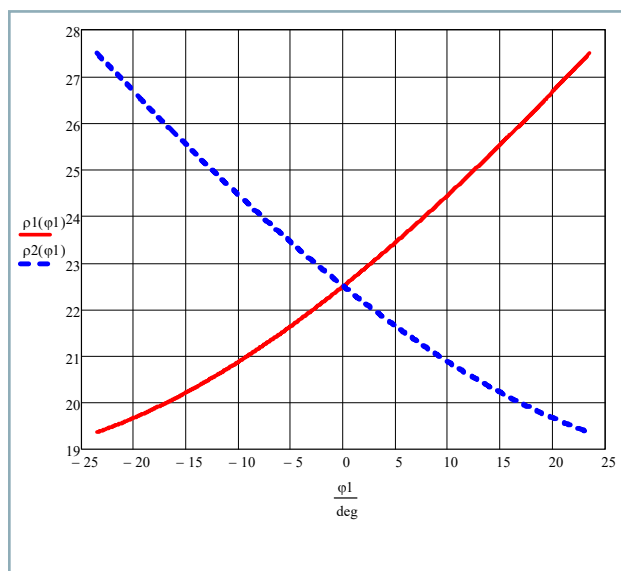


**Fig. 12** Dependences of the lengths of radii  $\rho_{1,2}$  on the driving gear rotation angle  $\phi_1$  with teeth number  $z_{1,2} = 8$  in the reference system from the axis  $O_1O_2$

Subsequently, for the dependences of the lengths of the radii  $\rho_{1,2}$  on the parameter  $\phi_1$ :

$$\rho_1 = r_{b1} \sqrt{(\text{tg}\alpha_w + \phi_1)^2 + 1} \tag{46}$$

$$\rho_2 = r_{b2} \sqrt{(\text{tg}\alpha_w - \phi_1 / i)^2 + 1} \tag{47}$$

Corresponding graphical dependences will have the same form, but the gearing point will be at the point with coordinate 0 (Figs 11, 12).

**Conclusion**

1. The source analysis of scientific and technical findings showed that, in the existing models of gear hydraulic

machine working process, the feature of involute gearing is not taken into account. The feature lies in a fact that involute tooth profiles in their movement mutually slip along each other.

2. To study this feature, the task was set and successfully solved to determine the dependences of rotation angles  $\chi_1$  and  $\chi_2$  of radii  $\rho_1$  and  $\rho_2$  connecting the rotation axes of gears with the gearing point  $T$  at the driving gear rotation angle  $\phi_1$  or the position coordinates of teeth gearing point  $T$  on the gearing line. At the same time, the slip of involute gear tooth profiles has been taken into account.
3. The dependences of lengths of radii  $\rho_1$  and  $\rho_2$  connecting the rotation axes of gears with the gearing point  $T$  at the

driving gear rotation angle  $\phi_1$  or the position coordinates of teeth gearing point  $T$  on the gearing line were found.

4. The expressions obtained will improve the existing mathematical models of the hydraulic oil movement in gear hydraulic machines, allowing to study a number of processes in hydraulic machines, namely:

- input nature with taking into account the new features in work of gear hydraulic machines;
- features of changes in the cut-off cavity and hydrodynamic processes occurring in it;
- pressure pulsation and hydraulic oil input;
- nature of change in the load on bearings of pump and motor;
- nature of change in combined torque developed by the gear motor;
- nature of change in power developed by the gear hydraulic motor.

## References

- ARTOBOLEVSKY, I. I. 1988. Theory of Mechanisms and Machines. Moscow: Nauka Publ., 640 pp. ISBN 978-5020138100. (In Russian: Teoriya mehanizmov i mashin).
- CASOLI, P. – VACCA, A. – BERTA, G. L. 2008. Optimization of relevant design parameters of external gear pumps. In Proceedings of the 7th JFPS International Symposium on Fluid Power. Toyama, Japan, Sept. 15–18, 2008. ISBN 4-931070-07-X.
- GAMEZ-MONTERO, P. J. – CASTILLA, R. – CODINA, E. 2018. Methodology based on best practice rules to design a new-born trochoidal gear pump. In Proceedings of the Institution of Mechanical Engineers, Part C: Journal of Mechanical Engineering Science, vol. 232, no. 6, pp. 1057–1068.
- HUANG, K. J. – CHEN, CH. 2008. Kinematic displacement optimization of external helical gear pumps. In Chung Hua Journal of Science and Engineering, vol. 6, no. 2, pp. 23–28.
- IVANOVIC, L. – DEVEDZIC, G. – CUKOVIC, S. – MIRIC, N. 2012. Modeling of the meshing of trochoidal profiles with clearances. In Journal of Mechanical Design, vol. 134, no. 4, pp. 041003-1–041003-9.
- KUČERA, M. – ALEŠ, Z. 2017. Morphology analysis of friction particles generated in tractor transmission oils. In Acta Technologica Agriculturae, vol. 20, no. 3, pp. 57–62.
- KULESHKOV, Yu. V. – CHERNOVOL, M. I. – RUDENKO, T. V. – GUTSUL, V. I. – OSIN, R. A. 2010. Investigation of the behavior of mathematical model of the specific displacement of a gear pump of NSH type from the gearing parameters. In Agricultural Engineering, Industry Engineering, Automation. Collection of scientific works of Kirovohrad National Technical University 2010. Kirovohrad: Kirovohrad National Technical University, pp. 278–290. ISSN 2409-9392.
- KULESHKOV, Yu. V. – CHERNOVOL, M. I. – BEZ, O. V. – TITOV, Yu. A. 2009. Gear Pumps with Asymmetric Gearing Line. Theory, Design and Calculation. Monography. Kirovohrad: KOD, 243 pp. ISBN 978-966-1508-19-3.
- STRYCZEK, J. – BEDNARCZYK, S. – CODINA, E. – GAMEZ-MONTERO, P. J. – IVANOVIC, L. – MATEJIC, M. 2019. Gears or rotors – three approaches to design of working units of hydraulic machines. In IOP Conference Series: Materials Science and Engineering, vol. 959, pp. 1–13. ISSN 1757-8981.
- TKÁČ, Z. – ČORŇÁK, Š. – CVIKLOVIČ, V. – KOSIBA, J. – GLOS, J. – JABLONICKÝ, J. – BERNÁT, R. 2017. Research of biodegradable fluid impacts on operation of tractor hydraulic system. In Acta Technologica Agriculturae, vol. 20, no. 2, pp. 42–45.
- TULÍK, J. – HUJO, Ľ. – KOSIBA, J. – JABLONICKÝ J. – JÁNOŠOVÁ, M. 2017. Evaluation of new biodegradable fluid on the basis of accelerated durability test, FTIR and ICP spectroscopy. In Research in Agricultural Engineering, vol. 63, no. 1, pp. 1–9.
- VACCA, A. – GUIDETTI, M. 2011. Modelling and experimental validation of external spur gear machines for fluid power applications. In Simulation Modelling Practice and Theory, vol. 19, no. 9, pp. 2007–2031.
- WANG, S. – SAKURAI, H. – KASAREKAR, A. 2011. The optimal design in external gear pump and motors. In IEEE/ASME Transactions on Mechatronics, vol. 16, no. 6, pp. 945–952.
- ZHOU, H. – DU, R. – XIE, A. – YANG, H. 2017. Investigations of the micro surface shape for the gear shaft/journal – bearing interface in water hydraulic internal gear pumps. In Advances in Mechanical Engineering, vol. 9, no. 11.



Acta Technologica Agriculturae 2  
Nitra, Slovaca Universitas Agriculturae Nitriae, 2021, pp. 92–96

## SPRAY COVERAGE AND BIOLOGICAL EFFICACY OF SINGLE, TWIN SYMMETRICAL, AND TWIN ASYMMETRICAL FLAT FAN NOZZLES

Akbar ALIVERDI\*, Masoud BORGHEI

Bu-Ali Sina University, Hamedan, I.R. Iran

Proper selection of nozzle type and spray volume is essential to optimize herbicide dose, reducing its adverse environmental effects. It has not been sufficiently evaluated which nozzle type (twin symmetrical flat fan nozzle or the twin asymmetrical one) is more efficient and whether pinoxaden application is more efficient at a low or high spray volume. The spray coverage of a single, twin symmetrical, and twin asymmetrical flat fan nozzles, each in the sizes of 110015, 11002, 110025, 11003, 11004, and 11005 on the moisture-sensitive papers (MSPs) was investigated. The biological efficacy of treatments using pinoxaden against wild oat was investigated. Unlike other nozzle types, the single flat fan nozzle could not cover MSP placed vertically behind the nozzle trajectory. Except for the latter, each nozzle type could cover the MSPs more efficiently with increase in nozzle size. Generally, the nozzles' performance was twin symmetrical > single = twin asymmetrical flat fan nozzles. A larger nozzle size improved the coverage of MSPs but increased the effective dose ( $ED_{50}$ ; dose that gives a 50% reduction in dry weight), indicating a decrease in the efficacy of pinoxaden. Among all treatments, the lowest  $ED_{50}$  value was obtained by the twin symmetrical flat fan nozzle 110015 (5.2 g a.i.  $ha^{-1}$ ). The smaller, more concentrated droplets are required to achieve optimal pinoxaden efficacy against wild oat, which can be provided by a twin symmetrical flat fan nozzle with a smaller size.

**Keywords:** graminicide; nozzle type; nozzle size; wild oat

The efficacy of many herbicides, including acetyl CoA carboxylase (ACCCase) inhibitors, can be affected by spray volume (Knoche, 1994). Therefore, selecting a proper spray volume is considered a simple method to optimize the herbicide dose (Aliverdi and Zarei, 2020), reducing its adverse environmental effects (Shahgholi et al., 2015). The ACCCase inhibitors have shown different behaviour with changing spray volume. In clodinafop-propargyl (Gauvrit and Lamrani, 2008; Naser and Aliverdi, 2020) and sethoxydim (McMullan, 1995), the efficacy increased as spray volume reduced. In fenoxaprop-P-ethyl (Gauvrit and Lamrani, 2008) and fluazifop-p-butyl (Creech et al., 2015a,b), spray volume does not affect the efficacy. In quizalofop-p-ethyl (Sikkema et al., 2008) and cycloxydim (Aliverdi and Karami, 2019), the efficacy increased as spray volume increased. In haloxyfop-R-methyl (Buhler and Burnside, 1984), the effect of spray volume on the efficacy depended on species against which it was applied: against *Sorghum bicolor*, the efficacy increased as spray volume reduced, however, against *Setaria lutescens*, spray volume did not affect the efficacy. There are two possible methods for adjusting the spray volume – changing either the sprayer driving speed or nozzle size. If either a very low or high spray volume is required to achieve optimal herbicide efficacy, the first method's applicability is problematic. For this reason, the second method always seems to be more feasible (Knoche, 1994; Pourdarbani, 2019).

Grassy species, including winter wild oat (*Avena sterilis* ssp. *ludoviciana*), should usually be treated with ACCCase

inhibitors, including pinoxaden, at the three- to four-leaf stage. At such a growth stage, their leaves are almost perpendicular to the ground. When a single flat fan nozzle is used to spray ACCCase inhibitors, the spray droplets, which move perpendicular to the ground, impact the leaf surface non-vertically. Hence, it is likely that a large proportion of them will bounce off the leaf surface to the soil surface and be wasted. Moreover, the faster the sprayer driving speed, the more the spray droplets bounce off (Jensen et al., 2001; Jensen, 2012). For this reason, if low spray volume is required, it is necessary to use a small orifice nozzle. Previous research has shown that changing the spray direction from vertical to non-vertical significantly improves the efficacy of haloxyfop-ethoxyethyl (Jensen et al., 2001), clodinafop-propargyl, fluazifop-P-butyl (Jensen, 2012), sethoxydim (Aliverdi, 2018; Aliverdi and Zarei, 2020), cycloxydim, and sethoxydim (Aliverdi and Zarei, 2020). Non-vertical spray can decrease the non-vertical spray droplet impact to the leaf surface (Jensen, 2012). Twin flat fan nozzles create two non-vertical sprays (flat fans), and the angle between them can be symmetrical or asymmetrical. Therefore, they can also decrease the non-vertical spray droplet impact to the leaf surface. There has been already reported better performance for twin flat fan nozzle in contrast to single flat fan nozzle (Nordbo et al., 1995; Combella et al., 1996; Vallet and Tinnet, 2013; Aliverdi, 2018; Aliverdi and Zarei, 2020). They are recommended for application of low spray volumes at high driving speeds (Vallet and Tinnet, 2013).

**Contact address:** Akbar Aliverdi, Bu-Ali Sina University, Faculty of Agriculture, Department of Agronomy and Plant Breeding, Hamedan, I.R. Iran; e-mail: [a.aliverdi@basu.ac.ir](mailto:a.aliverdi@basu.ac.ir)

Although a proper selection of nozzle type and spray volume is essential to optimize the herbicide dose, reducing its adverse environmental effects, the comparative performance assessment of twin symmetrical and twin asymmetrical flat fan nozzles has not been carried out. Furthermore, there is a lack of information on whether the pinoxaden is more effective if applied at a low or high spray volume. Hence, this study intends to fill the gaps mentioned.

## Material and methods

### Dose-response study

The winter wild oat seeds, from which lemma and palea had been removed, were treated using the same method as described by Aliverdi and Zarei (2020). When the coleoptile of seedlings reached 1 cm, they were planted at 1 cm depth (five seedlings in each 2-l pot  $\sim 195$  plant $\cdot$ m $^{-2}$ ). The pots were filled with a sandy loam soil with 1.1% organic matter and a pH of 7.6. The pots were placed in the Research Greenhouse of Bu-Ali Sina University, Hamadan, Iran, and irrigated once every five days. The greenhouse temperature was within the range of 17–26 °C during the day and 12–15 °C during the night with a natural photoperiod of 11–13 h.

The experiment was performed as a factorial ( $6 \times 3 \times 6$ ) in a completely randomized design with four replications. Treatments included six doses of pinoxaden (0, 3.75, 7.5, 15, 30, and 60 g a.i. ha $^{-1}$ ), which were sprayed using three nozzle types (single, twin symmetrical, and twin asymmetrical flat fan nozzles) of six sizes (110015, 11002, 110025, 11003, 11004, and 11005; which provide 120, 160, 200, 240, 320, and 400 l $\cdot$ ha $^{-1}$  spray volume, respectively) at the three-leaf stage of winter wild oat. A 20° forward angled spray and a 20° rearward angled spray can be provided by twin symmetrical flat fan nozzle, the angle between which is 40°. A 70° forward angled spray and a 30° rearward angled spray can be provided by twin asymmetrical flat fan nozzle, the angle between which is 100°. The spray patterns of

nozzle types used in the study are illustrated in Fig. 1. At constant pressure of 300 kPa attaining with CFValve™ (Gate Co., USA) assembled between sprayer lance and nozzle, the range of volume median diameter was 61–105  $\mu$ m for twin symmetrical and twin asymmetrical flat fan nozzles 110015, 236–340  $\mu$ m for single flat fan nozzle 11005, and 106–235  $\mu$ m for other nozzles (MagnoJet, 2020). The treatments were applied with a hand compressor sprayer in the open air outside the greenhouse. Air temperature ranged from 15 °C to 18 °C, relative humidity ranged from 48% to 59%, and wind speed ranged from 0.2 m $\cdot$ s $^{-1}$  to 0.5 m $\cdot$ s $^{-1}$ . The pots were placed again in the greenhouse after treatment.

Four weeks after treatment, the plants were harvested 1 cm above the soil surface, oven-dried at 70 °C for two days, then weighed to obtain dry weight. The data were analysed by non-linear regression analysis using R software (Ritz et al., 2015). According to Lack-of-fit test ( $p$ -value  $> 0.05$ ), a logarithmic four-parameter model was identified as a suitable one:

$$Y = C + \{D - C / 1 + \exp [B(\log X - \log ED_z)]\} \quad 1)$$

where:

$Y$  – dry weight

$D$  and  $C$  – upper and lower limits for  $Y$ , respectively

$X$  – dose of pinoxaden

$ED_z$  – effective dose (g a.i. ha $^{-1}$ ) required to reduce the dry weight of winter wild oat by  $z$  % as compared to the control treatment

### Spray deposition study

This study was performed simultaneously with the dose-response study when 60 g a.i. ha $^{-1}$  was being sprayed to investigate the coverage percentage of moisture-sensitive papers (MSP; 26  $\times$  76 mm) from the treatments. The MSPs were placed in three positions (Fig. 2): horizontally on the ground (MSP $_1$ ), vertically in front of the nozzle trajectory

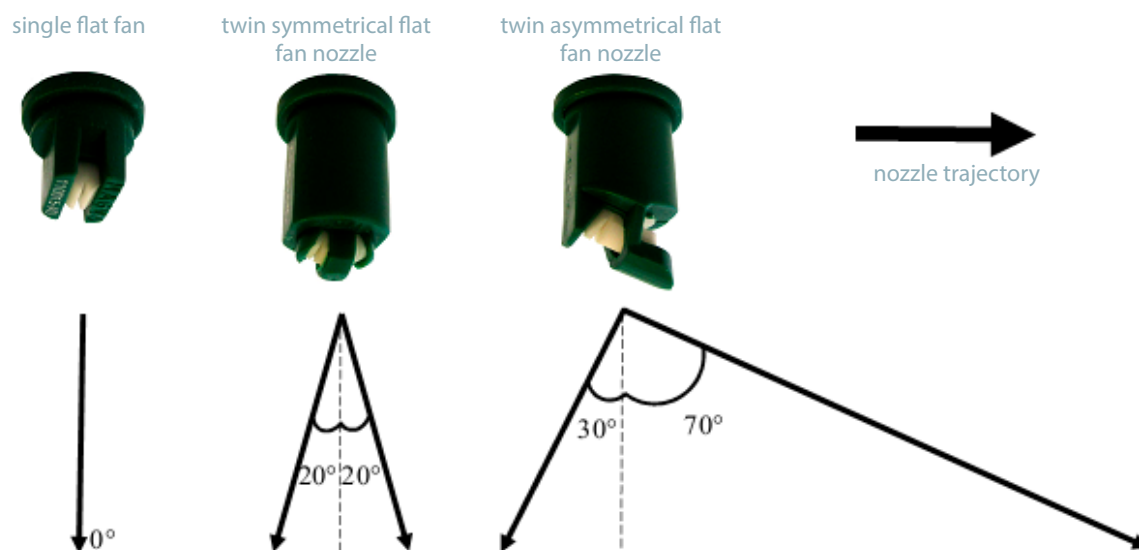


Fig. 1 Spray pattern of nozzle types used in the study

(MSP<sub>2</sub>), and vertically behind the nozzle trajectory (MSP<sub>3</sub>). For each position, the experiment was performed as a factorial experiment (3 × 6) in a completely randomized design with three replications; the factor of

nozzle type in three levels (single, twin symmetrical, and twin asymmetrical flat fan nozzles) and the factor of nozzle size in six levels (110015, 11002, 110025, 11003, 11004, and 11005).

The MSPs were scanned and image-processed in Image J software version 1.48. to detect the spray coverage (%). A normal distribution of data was stabilized (Shapiro-Wilk test >0.91). The data were subjected to analysis of variance using SAS software version 4.9. The means were compared using Duncan’s test at the level of 5% probability.

### Results and discussion

The coverage of all MSPs was significantly affected by nozzle type and size. There was an interaction effect between simple effects (*p*-value <0.01).

The MSP<sub>1</sub> was entirely covered by single and twin symmetrical flat fan nozzles in sizes 11003, 11004, and 11005 (Table 1). The MSP<sub>1</sub> was covered minimally (12.5%) when the spray solution was applied using the twin asymmetrical flat fan nozzle 110015. Considering all the nozzle sizes, the MSP<sub>1</sub> was covered the least using asymmetrical flat fan nozzle in contrast to other nozzle types. Theoretically, the droplets from the 70° forward angled spray of asymmetrical flat fan nozzle will have to pass a distance of 146.2 cm to the MSP<sub>1</sub> when the height of the nozzle is 50 cm (distance = 50/cos 70°). With such a distance, the droplets spend more time in space to the target, causing them most likely to drift.

The MSP<sub>2</sub> was entirely covered using the single and twin symmetrical flat fan nozzles in sizes 11003, 11004, and 11005 (Table 1). The MSP<sub>2</sub> was covered minimally (21.5%) when the spray solution was applied by the single flat fan nozzle 11002. In general, the twin flat fan nozzles were more successful in covering the MSP<sub>2</sub> than the single flat fan nozzles. Using the single flat fan nozzle, the droplets move vertically from the nozzle to the ground. Therefore, the droplets cannot have an effective impact on the MSP<sub>2</sub>. Conversely, by the twin flat fan nozzles, the forward angled spray can direct the droplets towards the MSP<sub>2</sub>, resulting in better coverage. The MSP<sub>3</sub> was entirely covered using the twin symmetrical and asymmetrical flat fan nozzles in sizes 11004 and 11005 (Table 1). The performance of the twin symmetrical flat fan nozzle in covering

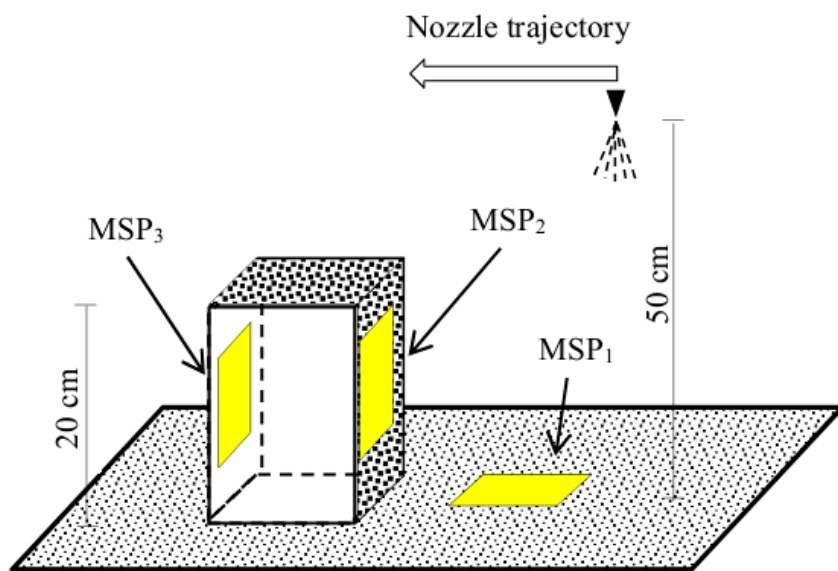


Fig. 2 Position of moisture-sensitive papers (MSP) relative to the nozzle trajectory

Table 1 Effect of nozzle type and size on the coverage of moisture-sensitive papers (MSP) placed in the positions shown in Fig. 2

Nozzle type	Nozzle size	MSP <sub>1</sub> (%)	MSP <sub>2</sub> (%)	MSP <sub>3</sub> (%)
Single flat fan	110015	24.3 g	29.1 f	0.0 g
	11002	69.2 de	21.5 g	0.3 g
	110025	76.7 c	42.7 de	0.3 g
	11003	100 a	40.0 ef	0.0 g
	11004	100 a	73.6 b	0.0 g
	11005	100 a	79.2 b	0.0 g
Twin symmetrical flat fan	110015	24.6 g	34.3 ef	12.2 f
	11002	72.3 cd	62.1 c	30.1 e
	110025	88.1 b	72.9 b	72.5 c
	11003	100 a	100 a	97.5 a
	11004	100 a	100 a	100 a
	11005	100 a	100 a	100 a
Twin asymmetrical flat fan	110015	12.5 h	32.6 f	10.3 f
	11002	23.9 g	49.3 d	13.2 f
	110025	36.4 fg	49.7 d	38.2 d
	11003	35.4 fg	100 a	88.6 b
	11004	40.9 f	100 a	100 a
	11005	63.4 e	100 a	100 a

In each MSP, the means with a common letter are not statistically different based on Duncan test at the 0.05 probability level

MSP<sub>3</sub> was better than that of the twin asymmetrical flat fan nozzle. The single flat fan nozzle could not wet MSP<sub>3</sub> at all. Except for the latter, all nozzle types showed better coverage of all MSPs with increasing nozzle size. A similar result was reported by Hunter et al. (2019) with the single flat fan nozzle and Naser and Aliverdi (2020) with the single and twin symmetrical flat fan nozzles.

Among all treatments, the lowest values of ED<sub>50</sub> and ED<sub>90</sub> were observed with the twin symmetrical flat fan nozzle 110015 (5.2 and 21.2 g a.i. ha<sup>-1</sup>, respectively). The highest values of ED<sub>50</sub> and ED<sub>90</sub> were observed with the single flat fan nozzle 11005 (39.2 and 91.9 g a.i. ha<sup>-1</sup>, respectively) (Table 2). In other words, the performance of the twin symmetrical flat fan nozzle 110015 was 5.2 times higher based on ED<sub>50</sub> and 4.3 times higher based on ED<sub>90</sub> than that of the single flat fan nozzle 11005. In all nozzle types, the ED<sub>50</sub> and ED<sub>90</sub> values increased significantly with increasing the nozzle size (spray volume). Therefore, there was found a negative relationship

between spray volume and the efficacy of pinoxaden against winter wild oat. Moreover, this relationship was more negative when the single fan nozzle was used. A 65% and a 64% increase in the ED<sub>50</sub> and ED<sub>90</sub> values, respectively, occurred when the size of the single fan nozzle increased from 110015 to 11005. A 49% and a 59% increase in the ED<sub>50</sub> and ED<sub>90</sub> values, respectively, occurred when the size of the twin symmetrical fan nozzle increased from 110015 to 11005. A 57% and a 62% increase in the ED<sub>50</sub> and ED<sub>90</sub> values, respectively, occurred when the size of the twin asymmetrical fan nozzle increased from 110015 to 11005. As mentioned above, previous studies have reported a positive, neutral, or negative relationship between spray volume and the efficacy of ACCase inhibitors. In case of pinoxaden, the results showed that a larger nozzle size could improve the coverage of MSPs (Table 1), but it decreased the efficacy (Table 2). Increased efficacy of pinoxaden when spray volume was reduced can be due to certain reasons. The smaller the size nozzle,

the smaller the droplet size. Smaller droplets may deposit better over the leaf surface, resulting in improved herbicide efficacy (Butts et al., 2018). The lower the spray volume, the higher the concentration of herbicide. More concentrated herbicide may create a greater concentration gradient for herbicide between the spray solution and leaf, increasing the diffusion of herbicide into leaf, resulting in improved herbicide efficacy (Buhler and Burnside, 1984). Therefore, the smaller, more concentrated droplets can improve the efficacy of pinoxaden against winter wild oat than the larger, more diluted ones.

When averaged over the six nozzle sizes, the ED<sub>50</sub> values for single, twin symmetrical, and twin asymmetrical flat fan nozzles were 16.42, 9.15, and 16.68 g a.i. ha<sup>-1</sup>, respectively; and the ED<sub>90</sub> values were 51.59, 39.43, and 50.90 g a.i. ha<sup>-1</sup>, respectively. These results showed that the nozzles' performance was twin symmetrical > single = twin asymmetrical flat fan nozzles. The lower performance of single flat fan nozzle in contrast to twin symmetrical flat fan nozzle can be due to various reasons, e.g. the former creates one vertical spray and leaves of grassy species are relatively perpendicularly oriented to the ground.

Therefore, the impact angle of droplets on the leaves is most likely low. Hence, it is likely that a large number of them will bounce off the leaf surface to the soil surface and be wasted. Simultaneously, the latter creates two non-vertical sprays, which leads to a situation when the impact angle of droplets on the leaves is most likely high, reducing the number of the droplets bounced off (Jensen et al., 2001; Dorr et al., 2015). At the same size as the latter, the former will always show smaller droplet size due to atomizing through two orifices. This is true even for sizes 11002, 110025, 11003, and 11004. Although the former is provided with a similar spray classification as the latter (MagnoJet, 2020), we know that the latter has to have a smaller average droplet size. As mentioned above, smaller droplets may deposit better over the leaf surface, resulting in improved herbicide efficacy (Butts et al. 2018). In our previous study, an increased number of flat fans (single, twin symmetrical, and

**Table 2** Effective dose (ED) of pinoxaden required to reduce the dry weight of wild oat by 50% and 90% compared to control treatment

Nozzle type	Nozzle size	ED <sub>50</sub> (g a.i. ha <sup>-1</sup> )	ED <sub>90</sub> (g a.i. ha <sup>-1</sup> )
Single flat fan	110015	8.8 (0.1) c	33.9 (1.6) cd
	11002	11.3 (0.8) e	35.6 (0.9) d
	110025	11.0 (0.6) e	41.5 (0.8) f
	11003	17.7 (0.9) g	47.0 (2.0) g
	11004	22.4 (0.9) i	59.6 (0.7) i
	11005	27.2 (1.1) j	91.9 (3.1) k
Twin symmetrical flat fan	110015	5.2 (0.3) a	21.2 (0.5) a
	11002	7.7 (0.3) b	24.2 (1.9) b
	110025	8.9 (0.5) c	41.7 (1.2) f
	11003	10.4 (0.5) de	39.9 (0.4) e
	11004	12.6 (0.8) ef	55.5 (0.9) h
	11005	10.2 (0.9) de	54.0 (2.7) h
Twin asymmetrical flat fan	110015	9.8 (0.3) d	25.4 (1.5) b
	11002	12.6 (0.4) f	30.6 (2.3) c
	110025	13.7 (0.7) f	48.8 (0.9) g
	11003	19.3 (1.3) h	61.7 (1.7) i
	11004	22.0 (1.3) i	70.8 (1.6) j
	11005	22.7 (1.8) i	68.1 (2.4) j

Standard errors are in parentheses. In each ED, the values with the same letter are not different ( $p < 0.05$ )

triplet-orifice flat fan nozzles) reduced the values of ED<sub>50</sub> for cycloxydim against wild barley (Aliverdi and Karami, 2019). In the current study, however, the performance of twin fan asymmetrical flat fan nozzle was equal to that of the single flat fan nozzle. This weakness can be due to the fact that the droplets produced by the 70° forward angled spray of twin fan asymmetrical nozzle are driftable (Table 1).

### Conclusion

Based on the literature review, the efficacy of herbicides is correlated with spray volume, which can be identified only by experiment. Current results accepted this theory found in the literature. In all nozzle types, the efficacy of pinoxaden against winter wild oat increased with decreasing the nozzle size (spray volume), indicating a requirement for the smaller, more concentrated droplets to achieve the optimal pinoxaden efficacy. Using low spray volume not only improves the efficacy of pinoxaden but is also economically advantageous in terms of water-saving. Regardless of the type of nozzle, such droplets can be produced with the nozzle size of 110015. Based on the results of spray deposition study, it seems that the front of plant was weakly covered using the twin asymmetrical flat fan nozzle and the back of plant cannot be wetted using the single flat fan nozzle at all. The twin symmetrical flat fan nozzle showed none of these weaknesses. As a result, regardless of the nozzle size, the highest pinoxaden efficacy was observed using the twin symmetrical flat fan nozzle. Current results suggest that the twin symmetrical flat fan nozzle of size 110015 can be selected as a proper nozzle type for producing the appropriate spray volume for pinoxaden application against winter wild oat.

### Acknowledgements

This work was funded by Bu-Ali Sina University. No conflicts of interest have been declared.

### References

- ALIVERDI, A. 2018. The selection of proper nozzle for spraying sethoxydim at two wind speeds to control winter wild oat (*Avena sterilis* ssp. *ludoviciana*). In *Journal of Plant Protection*, vol. 32 no. 2, pp. 299–306.
- ALIVERDI, A. – KARAMI, S. 2019. The effect of type and size of single, twin, and triplet flat fan nozzles on the activity of cycloxydim against wild barley (*Hordeum spontaneum* Koch.). In *Journal of Plant Protection*, vol. 33, no. 3, pp. 465–474.
- ALIVERDI, A. – ZAREI, M. 2020. Forward angled spray: a method for improving the efficacy of herbicides. In *Journal of Plant Protection Research*, vol. 60, no. 3, pp. 275–283.
- BUHLER, D. D. – BURNSIDE O. C. 1984. Effect of application factors on postemergence phytotoxicity of fluzifop-butyl, haloxyfop-methyl, and sethoxydim. In *Weed Science*, vol. 32, no. 5, pp. 574–583.
- BUTTS, T. R. – SAMPLES, C. A. – FRANCA, L. X. – DODDS, D. M. – REYNOLDS, D. B. – ADAMS, J. W. – ZOLLINGER, R. K. – HOWATT, K. A. – FRITZ, B. K. – CLINT, H. W. – KRUGER, G. R. 2018. Spray droplet size and carrier volume effect on dicamba and glufosinate efficacy. In *Pest Management Science*, vol. 74, no. 9, pp. 2020–2029.
- COMBELLACK, J. H. – WESTERN, N. M. – RICHARDSON, R. G. 1996. A comparison of the drift potential of a novel twin fluid nozzle with conventional low volume flat fan nozzles when using a range of adjuvants. In *Crop Protection*, vol. 15, no. 2, pp. 147–152.
- CREECH, C. F. – HENRY, R. S. – FRITZ, B. K. – KRUGER, G. R. 2015a. Influence of herbicide active ingredient, nozzle type, orifice size, spray pressure, and carrier volume rate on spray droplet size characteristics. In *Weed Technology*, vol. 29, no. 2, pp. 298–310.
- CREECH, C. F. – HENRY, R. S. – WERLE, R. – SANDELL, L. D. – HEWITT, A. J. – KRUGER, G. R. 2015b. Performance of post-emergent herbicides applied at different carrier volume rates. In *Weed Technology*, vol. 29, no. 3, pp. 611–624.
- DORR, G. J. – WANG, S. – MAYO, L. C. – MCCUE, S. W. – FORSTER, W. A. – HANAN, J. – HE, X. 2015. Impaction of spray droplets on leaves: influence of formulation and leaf character on shatter, bounce and adhesion. In *Experiments in Fluids*, vol. 56, no. 143.
- GAUVRIT, C. – LAMRANI, T. 2008. Influence of application volume on the efficacy of clodinafop-propargyl and fenoxaprop-P-ethyl on oats. In *Weed Research*, vol. 48, no. 1, pp. 78–84.
- HUNTER, J. E. – GANNON, T. W. – RICHARDSON, R. J. – YELVERTON, F. H. – LEON, R. G. 2019. Coverage and drift potential associated with nozzle and speed selection for herbicide applications using an unmanned aerial sprayer. In *Weed Technology*, vol. 34, no. 2, pp. 235–240.
- JENSEN, P. K. 2012. Increasing efficacy of graminicides with a forward angled spray. In *Crop Protection*, vol. 32, pp. 17–23.
- JENSEN, P. K. – JORGENSEN, L. N. – KIRKKNEL, E. 2001. Biological efficacy of herbicides and fungicides applied with low-drift and twin-fluid nozzles. In *Crop Protection*, vol. 20, no. 1, pp. 57–64.
- KNOCHÉ, M. 1994. Effect of droplet size and carrier volume on performance of foliage-applied herbicides. In *Crop Protection*, vol. 13, no. 3, pp. 163–178.
- MAGNOJET. 2020. Product Catalogue. Available at: <http://www.magnojet.com.br/produtos>
- MCMULLAN, P. M. 1995. Effect of spray volume, spray pressure and adjuvant volume on efficacy of sethoxydim and fenoxaprop-p-ethyl. In *Crop Protection*, vol. 14, no. 7, pp. 549–554.
- NASER, N. – ALIVERDI, A. 2020. Effect of nozzle type and spray volume on clodinafop-propargyl efficacy in winter wild oat (*Avena sterilis* subsp. *ludoviciana* Durieu.) control. In *Iranian Journal of Weed Science*, vol. 16, no. 1, pp. 37–48.
- NORDBO, E. – STEERMEN, J. K. – KITKNELT, E. 1995. Deposition and efficiency of herbicide sprays in sugar beet with twin-fluid, low-drift and conventional hydraulic nozzles. In *Crop Protection*, vol. 14, no. 3, pp. 237–240.
- POURDARBANI, R. 2019. Choosing a proper maintenance and repair strategy for tractors (in Urmia). In *Acta Technologica Agriculturae*, vol. 22, no. 1, pp. 12–16.
- RITZ, C. – BATY, F. – STREIBIG, J. C. – GERHARD, D. 2015. Dose-response analysis using R. In *PLoS One*, vol. 10, no. 12, pp. e0146021.
- SHAHGHOLO, H. – MAKARIAN, H. – SHOKATI, B. – TALAEI, G. H. – ASGHARIPUR, M. R. 2015. Do tillage methods affect germination and species similarity of soil weed seeds bank? In *Acta Technologica Agriculturae*, vol. 18, no. 4, pp. 97–101
- SIKKEMA, P. H. – BROWN, L. – SHROPSHIRE, C. – SPIESER, H. – SOLTANI, N. 2008. Flat fan and air induction nozzles affect soybean herbicide efficacy. In *Weed Biology and Management*, vol. 8, no. 1, pp. 31–38.
- VALLET, A. – TINET, C. 2013. Characteristics of droplets from single and twin jet air induction nozzles: A preliminary investigation. In *Crop Protection*, vol. 48, pp. 63–68.



Acta Technologica Agriculturae 2  
Nitra, Slovaca Universitas Agriculturae Nitriae, 2021, pp. 97–102

## INVESTIGATION OF THE INFLUENCE OF PERMANENT TRAFFIC LANE PROPERTIES ON ROLLING OF BRIDGE AGRICULTURAL EQUIPMENT WHEELS

Volodymyr BULGAKOV<sup>1\*</sup>, Semjons IVANOV<sup>2</sup>, Volodymyr KUVACHOV<sup>3</sup>, Dmytro PRYSIAZHNIUK<sup>4</sup>

<sup>1</sup>National University of Life and Environmental Sciences of Ukraine, Kyiv, Ukraine

<sup>2</sup>Latvia University of Life Sciences and Technologies, Jelgava, Latvia

<sup>3</sup>Dmytro Motornyi Tavria State Agrotechnological University, Melitopol, Ukraine

<sup>4</sup>Ladyzhyn College of Vinnitsa National Agrarian University, Vinnica, Ukraine

Movement of bridge agricultural equipment along the permanent traffic lanes is characterised by significant energy costs for overcoming the rolling resistance forces. Until now, the movement process of bridge agricultural equipment wheels along the compacted soil of permanent traffic lanes has been paid only a little attention. It has been established that the physical and mechanical properties of soil lanes significantly affect the energy consumption necessary for overcoming the rolling resistance of forces of bridge agricultural equipment wheels. Considering the range of possible changes in these properties, the coefficient of rolling resistance of equipment wheels varies from 0.06 to 0.1, which is 66%. In order to reduce the rolling resistance coefficient of equipment wheels when moving along the permanent traffic lanes, the surface needs to be undeformable. When moving along such a solid and dense supporting surface, the wheel rolling resistance is lowest.

**Keywords:** traffic lanes; resistance; movement; soil; physical and mechanical properties of soil

When using agricultural machinery with different working widths, majority of fertile soil (approx. 75%) is subjected to unfavourable impacts of the tractor and machinery wheels (Barwicki et al., 2012; Chen et al., 2010; Isbister et al. 2013; Galambošová et al., 2020). Controlled traffic farming confines all machinery loads to the least possible area of permanent traffic lanes. Moreover, it provides a wide range of benefits, e.g. greater rainfall infiltration rates, increased available water capacity, etc. (Tullberg et al., 2018). It represents an efficient way for managing the soil compaction by confining all load-bearing wheels to the least possible area of permanent traffic lanes (Galambošová et al., 2017).

The tractor theory informs that rolling of a wheel with an elastic rim along a deformable surface is characterised by energy consumption for overcoming the rolling resistance forces (Simikič et al., 2014; Kutkov, 2014). In this case, the main research tasks of tractor wheel rolling are: identification of a correlation of parameters and conditions of its rolling; search for criteria for evaluating the wheel rolling process; and determination of the ways how to reduce the rolling resistance (Kutkov, 2014). It should be noted that the dependence of rolling resistance coefficient of tractor wheels on the physical and mechanical properties of soil surface (especially the moisture, density and hardness) along which the wheels move has not been sufficiently considered and studied. The process of rolling of bridge agricultural equipment wheels along the compacted soil of permanent lanes practically remains unstudied although its energy costs are lower.

The very appearance of controlled traffic farming (Antille et al., 2015; Bulgakov et al., 2017; Gasso et al., 2013; Bulgakov et al., 2018) makes it possible to solve a fundamental contradiction in the “driver–soil” system. Essentially, if the energy tool is to achieve the high traction and hitching properties, its drivers must encounter dry, levelled, and solid supporting surface. However, plant cultivation requires fluffy-structured environment with optimal density and moisture. In practice, such requirements can be satisfied only when the movement zones of energy tools (the technological zone of field) and the zones of plant growth (the agrotechnical zone of field) are clearly differentiated (Chamen, 2015; Kingwelland Fuchsichler, 2011; Onal, 2012.). In this system, the agricultural bridge represents permanent traffic lanes; permissible boundaries for performing technological operations can vary significantly. Furthermore, optimal working conditions for the bridge agricultural equipment can differ significantly from the ideal conditions for the growth and development of cultivated plants. Issue of studying the impact dependences of physico-mechanical properties of the soil of permanent traffic lanes on the rolling resistance of bridge agricultural equipment wheels when moving along them becomes relevant.

In tractor theory, the coefficient of rolling resistance  $f_k$  is a dimensionless criterion for the wheel rolling evaluation, which takes into account the tangential force and resistance (Kutkov, 2014). It is calculated as the ratio of rolling resistance

$P_f$  to normal vertical load acting upon the wheel  $f_k$  (Kutkov, 2014):

$$f_k = \frac{D_f}{G_N} \quad (1)$$

There are many scientifically substantiated expressions for the calculation of rolling resistance coefficient  $f_k$  of a tractor wheel. The most frequently used is the Granvuane-Goryachkin dependence:

$$f_k = 0.86 \left[ \frac{G_N}{k_r \cdot b_0 \cdot D_0^2} \right]^{\frac{1}{3}} \quad (2)$$

where:  
 $k_r$  – volumetric crushing coefficient of soil (N·m<sup>-3</sup>)  
 $D_0, b_0$  – static diameter and the tire width of wheel, respectively (m)

The impacts of tire design, air pressure, movement speed, vertical load, etc. on the resistance coefficient of its rolling has been studied in sufficient detail (Panchenko and Kyurchev, 2008; Nadykto et al., 2015; Nadykto and Velichko, 2015; Nadykto et al., 2019). In practice, the rolling resistance coefficient value of tractor wheel is not calculated, but it is selected from the reference tables depending on the soil structure or road type. Moreover, the rolling resistance coefficients of propulsors of different machines differ significantly when driving under the same conditions. However, the wheel performance of agricultural bridge equipment while moving along the permanent traffic lanes has not been sufficiently studied. The rolling process of bridge agricultural equipment wheels along compacted soil of permanent traffic lanes remains practically unstudied.

This investigation strives to establish relationships between the impacts of physico-mechanical properties of soil tracks of permanent traffic lanes and the rolling resistance of agricultural bridge equipment wheels.



**Fig. 1** Experimental agricultural bridge equipment during a laboratory research of its rolling resistance along the permanent traffic lanes

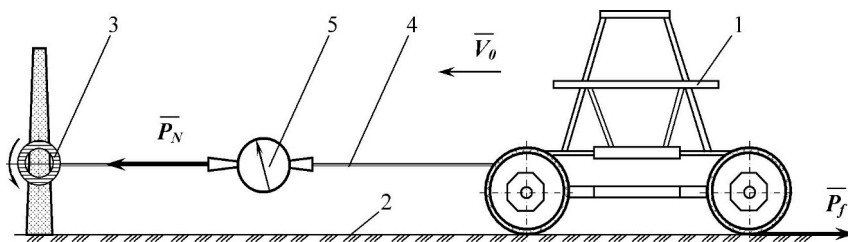


**Fig. 2** Laboratory complex for the rolling resistance force determination of agricultural bridge equipment along the tracks of permanent traffic lanes



**Fig. 3** Devices for determination of physical and mechanical properties of the soil in tracks of permanent traffic lanes  
 1 – Revyakín hardness tester; 2 – MG-44 hygrometer; 3 – densitometer

### Material and methods

The physical object of experimental research was a bridge agricultural equipment (Fig. 1) that was developed by Bulgakov et al. (2019). Equipment undercarriage is a trolley and the wheels with pneumatic tires of a standard size 9.5R32 are attached to its frame by four axles.

When considering the rolling process of bridge agricultural equipment wheels along the soil tracks of permanent traffic lanes, the general factors accompanying the operation of wheels were excluded: uneven movement, ascent or descent, the bearing resistance in the wheel hub, and air resistance. This research is based on the assumption that the bridge agricultural equipment wheels with constant air pressure in their tires roll along the tracks of horizontal section of permanent traffic lanes at a uniform speed.

The rolling resistance force of bridge agricultural equipment wheels along the tracks of permanent traffic lanes was determined by the principle

of its "free" movement along the supporting surface. The indicated "free movement" of agricultural bridge equipment along the tracks of permanent traffic lanes was carried out by its forced movement (Fig. 2).

The laboratory complex (Fig. 2) consisted of agricultural bridge equipment [1], wheels rolling freely along the formed tracks [2] of permanent traffic lanes. The free movement of agricultural bridge equipment [1] along the tracks [2] was effectuated by means of a traction mechanism [3], which was attached to it by the cable [4]. The effort necessary for free movement of the equipment [1] along the tracks [2] was recorded using dynamometer [5].

The basis for laboratory determination of the rolling resistance force of agricultural bridge equipment along the tracks of permanent traffic lanes is the equality of its rolling resistance force  $P_f$  and the force  $P_N$  at which it was rolling according to the dynamometric device (Fig. 2).

Physico-mechanical properties of the soil tracks of permanent traffic lanes were measured in a depth of 0–5 cm. For the purposes of soil hardness determination, Revyakin hardness tester was used (Fig. 3).

The soil density in the tracks was measured by a densitometer of own design (Fig. 3). The soil moisture was measured by MG-44 moisture meter (Fig. 3).

The standard Revyakin hardness tester (Fig. 3) consisted of a guide rod with a relatively small support surface, and a telescopic rod with a tip (a flat plunger with a working surface of 1 cm<sup>2</sup>), which was used for soil penetration to a depth of 5 cm. Tester telescopic rod was connected to the handle by a spring. When pressure is applied to the handle, the spring is compressed. Its deformations are recorded by a recording device through a special transmission mechanism. The tip was plunged through the compacted soil layers of the tracks in a slow manner and with a uniform force. On a millimetre paper, the hardness tester recorded a hardness diagram with continuous distribution of hardness value by depth. Ultimately, the hardness  $H$  (Pa) was determined as follows:

$$H = \frac{h_a \cdot q}{s} \quad (3)$$

where:

- $h_a$  – average ordinate value of the hardness diagram (cm)
- $q$  – instrument calibre (hardness of the hardener spring) (N·cm<sup>-1</sup>)
- $s$  – cross-sectional area of the hardness tester piston (cm<sup>2</sup>)

The MG-44 on-board electronic digital moisture meter (Fig. 3) is designed to measure the relative soil moisture using a sensitive radio frequency sensor with the range of 1–100%. The unit measurement time is max. 3 s. It is powered by an internal DC power supply unit. The measured relative humidity is counted from the liquid crystal indicator located on the front panel of indicator device. When measuring the soil track moisture, the electrode of MG-44 device was plunged into the soil to the depth of 0–5 cm. The sensor emits directed electromagnetic wave of high frequency, the part of which is absorbed by water molecules, and part is reflected in the sensor direction. By measuring the reflection coefficient of wave from a substance, which is directly

proportional to the moisture content, the relative moisture value is shown on the device display.

A specially developed densitometer (Fig. 3) based on the "cutting cylinder" principle was used to measure the soil track density in permanent traffic lanes. It is a metal base with a handle, which has three cutting cylinders attached to it (to determine the average sample value). To take soil samples from the top layer (0–5 cm) of tracks, a densitometer with cutting cylinders is put into soil by hitting the device's back part with a hammer. After filling the cutting cylinders with soil, the density value  $\rho$  (g·cm<sup>-3</sup>) can be calculated as follows:

$$\rho = \frac{m_t - m_0}{3 \cdot v_c} \quad (4)$$

where:

- $m_t, m_0$  – weight of suspended densitometer with and without soil (g)
- $v_c$  – single cutter cylinder volume (cm<sup>3</sup>)

Measurement of each parameter was repeated 10 times with their uniform placement along the entire length of pilot section of permanent traffic lanes. The measurement results were averaged. Statistical characteristics of measurements were calculated using the Microsoft Office Excel software. The error of direct experimental measurements of parameters using the devices shown in Fig. 3 did not exceed 2%.

In addition to mathematical calculations, statistical analysis of data was performed using the Microsoft Office Excel software. To establish the functional dependence between measured parameters, the standard procedure of statistical analysis using the "Trend Line" function was used in Microsoft Office Excel software. The functional dependence accuracy was estimated by determining the coefficient of ( $R^2$ ) reliability (correlation) of model, the best value of which is 1. For these purposes, the additional settings were adjusted in the Microsoft Office Excel software. The closer the obtained value to 1, the higher the model reliability.

Based on the measurement results, the following statistical characteristics were determined:

1. Average value  $Y$ :

$$Y = \frac{\sum y_i}{n} \quad (5)$$

where:

- $y_i$  – parameter value in  $i$  measurement
- $n$  – measurement quantity

2. Average quadratic deviation (standard)  $\sigma$ :

$$\sigma = \sqrt{\frac{\sum (y_i - Y)^2}{n}} \quad (6)$$

3. Coefficient of variation  $K$  (%):

$$K = \frac{100 \cdot \sigma}{Y} \quad (7)$$

Variability of the index measurement process was considered insignificant if the coefficient of variation  $K$  did

not exceed 10%. If its value is higher than 10%, but less than 20% – the variability was considered average. If  $K > 20\%$ , then the variability was considered significant. In this case, the reasons for obtaining such measurement results were studied, and the method of their determination was corrected and repeated.

### Results and discussion

The results showed that there is a sufficiently strong correlation between impacts of physical and mechanical properties of soil of permanent traffic lanes on the rolling resistance coefficient of agricultural bridge equipment wheels. The impact of soil moisture in tracks of permanent traffic lanes on the rolling resistance coefficient of equipment wheels is shown in Fig. 4. Here, the columns show the average quadratic deviation of this indicator. Analysis shows that an increase in soil moisture in tracks leads to an increase in the rolling resistance coefficient as well. Based on Fig. 4, the coefficient of variation of rolling

resistance did not exceed 10%, which indicates a slight variability (variability) in the definition of this indicator.

When the soil track moisture content increases from 10% to 45%, the rolling resistance coefficient of wheels increases from 0.06 to 0.1, which is 66% in percentage terms. However, in order to overcome the rolling resistance of agricultural bridge equipment wheels, the engine power consumption is proportional to value of  $f_k$  during the movement, resulting in increasing of energy consumption by the same percentage. The nature of relationship between the indicators shown in Fig. 4 can be explained by the fact that, with an increase in the moisture content of soil tracks, the losses due to soil compaction increase when the agricultural bridge equipment moves along the lanes. The indicated losses grow larger through the increase in the contact area of wheel tire with the supporting surface, and the increase in track depth produced by the wheels pressing on the soil. As a result, the rolling resistance coefficient of wheels increases while moving along the tracks. Ultimately,

in this case, the energy consumption for soil deformation significantly exceeds the energy consumption for tire deformation of agricultural bridge equipment wheels (Bulgakov et al., 2019).

The dependence between the rolling resistance coefficient  $f_k$  and the soil moisture is sufficiently exactly approximated as follows:

$$f_k = 4 \cdot 10^{-5} W^2 - 5 \cdot 10^{-4} W + 0.0562 \quad (8)$$

where:

$W$  – soil moisture in tracks of permanent traffic lanes (%)

The accuracy of obtained analytical expression (Eq. 8) can be estimated by the value of correlation coefficient, the square value of which is  $R^2 = 0.8767$  in relation to experimental data. The high value of the latter indicates potential practical use of the analytical dependence obtained (Eq. 8) in assessing the energy losses due to the movement of agricultural bridge equipment wheels along the permanent traffic lanes, taking into account the soil moisture content.

Since the soil moisture in tracks of permanent traffic lanes naturally affects hardness and density indicators, their changes are also reflected in the rolling resistance coefficient of agricultural bridge equipment wheels (Figs 5 and 6). Figs 5 and 6 show the average quadratic deviation of these indicators.

Analysis of experimentally obtained dependences (Figs 5 and 6) showed that increasing the hardness  $H$  and density  $\rho$  of the soil tracks lead to decreasing of the rolling resistance coefficient  $f_k$  of agricultural bridge equipment wheels moving along them. This decrease is of quadratic nature. The coefficient of variation of rolling resistance did not exceed 8.5%, indicating a slight variability in the definition of this indicator. Therefore, it is sufficiently accurately described as follows:

$$f_k = 0.0247H^2 - 0.2093H + 0.499 \quad (9)$$

where:

$H$  – soil hardness in tracks of permanent traffic lanes (determined by the Revyakin system) (MPa)

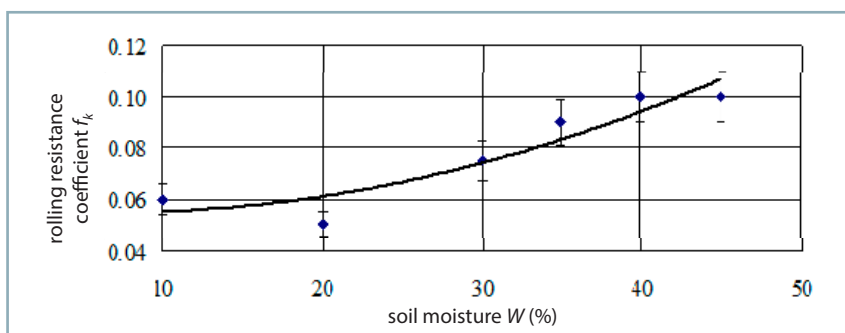


**Fig. 4** Dependence of the rolling resistance coefficient  $f_k$  of bridge agricultural equipment wheels on the moisture content  $W$  in soil tracks of permanent traffic lanes

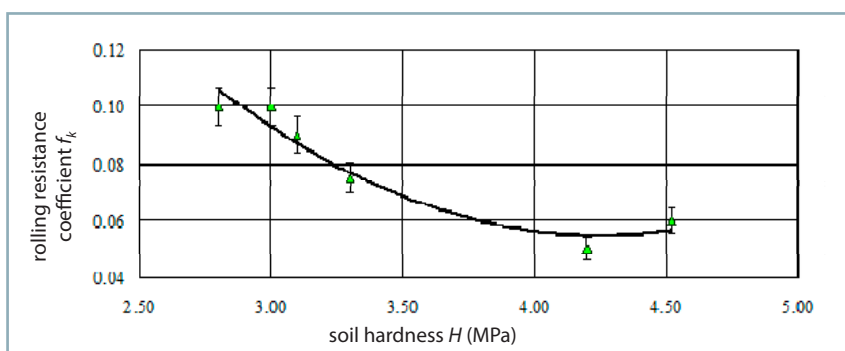


**Fig. 5** Dependence of the rolling resistance coefficient  $f_k$  of agricultural bridge equipment wheels on the hardness  $H$  of soil tracks of permanent traffic lanes

$$f_k = 0.335\rho^2 - 1.1256\rho + 0.9991 \quad (10)$$

where:

$\rho$  – soil density in tracks of permanent traffic lanes ( $\text{g}\cdot\text{cm}^{-3}$ )

It should be noted that the correlation between the hardness of soil tracks with the rolling resistance coefficient  $f_k$  (Eq. 9) is stronger than the relationship between the density of soil tracks and the rolling resistance coefficient  $f_k$  (Eq. 10). The square of correlation of  $f_k$  is  $R^2 = 0.9395$  for the hardness of soil tracks, and  $R^2 = 0.8419$  for the density of soil tracks.

The nature of experimentally obtained dependencies shown in Figs 6 and 7 can be explained by the circumstance that the increase in hardness and density of soil tracks lanes promotes reduction of the energy applied to agricultural bridge equipment wheels to perform such operations as vertical crushing of the soil and the formation of compacted tracks and friction of the tire tread upon the supporting surface in the contact area. Therefore, in order to reduce the coefficient  $f_k$  during the movement of agricultural bridge equipment along

the tracks of permanent traffic lanes, it needs to be a practically undeformable surface. When moving along such a solid and dense supporting surface, the wheel rolling resistance is minimal.

Based on the aforementioned, the rolling resistance coefficient of agricultural bridge equipment wheels moving along soil tracks of permanent traffic lanes can be sufficiently accurately estimated by the track hardness value. This allows establishing a relationship between the equipment wheel parameters and physico-mechanical properties of soil tracks with the indicators of track formation. For this, we equate dependencies (2) and (9). As a result, there is:

$$0.86 \left[ \frac{G_N}{k_r \cdot b_0 \cdot D_0^2} \right]^{\frac{1}{3}} = \quad (11)$$

$$0.0247H^2 - 0.2093H + 0.499$$

From the obtained equality (Eq. 11), it is possible to express the coefficient of volumetric crushing of soil:

$$k_r = \frac{0.636 \cdot G_N}{b_0 \cdot D_0^2 (0.0247H^2 - 0.2093H + 0.499)^3} \quad (12)$$

By substituting the 9.5R32 tire parameters  $D_0$  and  $b_0$  of agricultural bridge equipment (of own design), and the value of normal vertical load  $G_N$  acting upon the equipment wheels, an analytical dependence (Eq. 12) was obtained, which establishes a relationship between the coefficient of volumetric crushing  $k_r$  of soil in tracks of permanent traffic lanes and soil hardness  $H$  (Fig. 7).

Analysing the dependence presented in Fig. 7, with an increase of 2.5–4.0 MPa in hardness of soil tracks of permanent traffic lanes, the coefficient of volumetric crushing of soil also increases from 4 MPa to 45 MPa. Further increasing of soil hardness did not result in any significant increase in the coefficient of volumetric crushing of soil. The experimentally obtained graphical dependence (Fig. 7) is suitable for indirect estimation of the  $k_r$  value by the soil hardness indicator  $H$ , since the very methodology of determining the coefficient of volumetric crushing of soil is somewhat more complicated than determining its hardness.

The results indicate that indirect estimation of the rolling resistance coefficients of agricultural bridge equipment wheels moving along the tracks of permanent traffic lanes, and the coefficient of volumetric crushing of soil in terms of its hardness is sufficiently exact. This allows, if necessary, to determine the indicated parameters analytically from the experimentally measured values of hardness of soil tracks of permanent traffic lanes according to Eqs 9 and 12.

## Conclusions

1. When the moisture content of soil tracks of permanent traffic lanes increases from 10% to 45%, the rolling resistance coefficient of agricultural bridge equipment wheels (of own design) increases from 0.06 to 0.1, which is 66%.
2. When the hardness of soil tracks of permanent traffic lanes increases from 2.8 MPa to 4.5 MPa and its density from  $1.3 \text{ g}\cdot\text{cm}^{-3}$  to  $1.6 \text{ g}\cdot\text{cm}^{-3}$ , the rolling resistance coefficient of agricultural bridge equipment wheels moving along the lanes decreases from 0.1 to 0.06, and it is of a quadratic nature.
3. Increasing the hardness of the soil tracks from 2.5 MPa to 4.0 MPa results

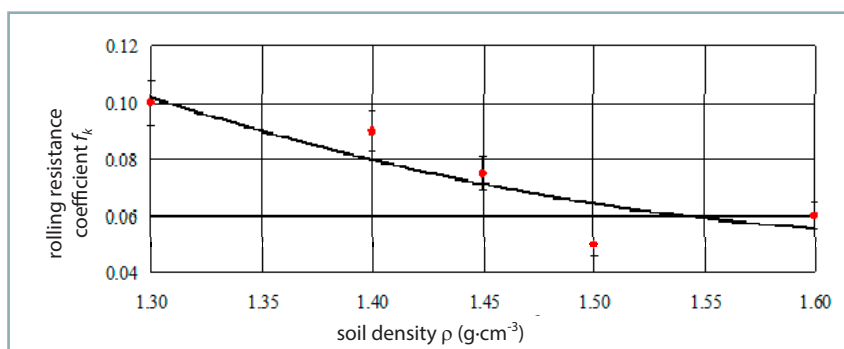


**Fig. 6** Dependence of the rolling resistance coefficient  $f_k$  of agricultural bridge equipment wheels on the density  $\rho$  of soil tracks of permanent traffic lanes

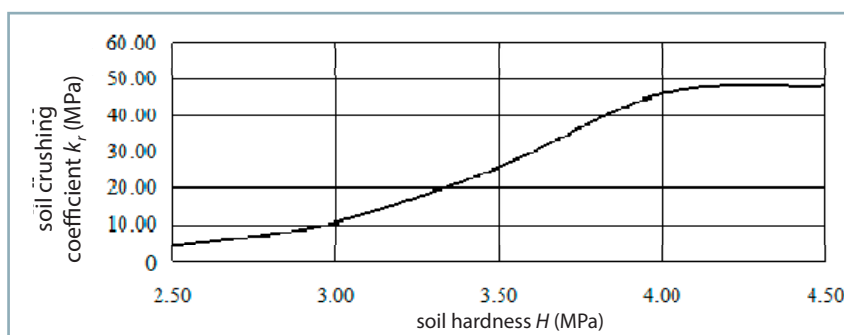


**Fig. 7** Dependence of the coefficient of volumetric crushing  $k_r$  of soil tracks on soil hardness  $H$

in intense increasing of the coefficient of volumetric crushing of soil from 4 MPa to 45 MPa. However, further increasing of hardness of soil tracks did not lead to any practical development of the coefficient of volumetric crushing of soil.

4. To reduce the rolling resistance coefficient of agricultural bridge equipment wheels moving along the soil tracks of permanent traffic lanes, the contact surface needs to be undeformable.

## References

- ANTILLE, D. L. – CHAMEN, W. C. T. – TULLBERG, J. N. – LAL, R. 2015. The potential of controlled traffic farming to mitigate greenhouse gas emissions and enhance carbon sequestration in arable land: a critical review. In *Transactions of the ASABE*, vol. 58, no. 3, pp. 707–731.
- BARWICKI, J. – GACH, S. – IVANOV, S. 2012. Proper utilization of the soil structure for the crops today and conservation for future generations. In *Engineering for Rural Development*, vol. 11, pp. 10–15.
- BULGAKOV, V. – ADAMCHUK, V. – KUVACHOV, V. – IVANOV, S. 2017. Research of possibilities for efficient use of wide span tractor (vehicle) for controlled traffic farming. In *Engineering for Rural Development: 16 International Scientific Conference, Proceedings*, vol. 16, Jelgava, Latvia, pp. 281–287.
- BULGAKOV, V. – ADAMCHUK, V. – NOZDROVICKÝ, L. – KUVAČOV, V. 2018. Study of effectiveness of controlled traffic farming system and wide span self-propelled gantry-type machine. In *Research in Agricultural Engineering*, vol. 64, no. 1, pp. 1–7.
- BULGAKOV, V. – KUVACHOV, V. – OLT, J. 2019. Theoretical study on power performance of agricultural gantry systems. In *Proceedings of the 30th International DAAAM Symposium "Intelligent Manufacturing and Automation"*, 23–26th October 2019, vol. 30, no. 1, pp. 0167–0175.
- CHAMEN, W.C.T. 2015. Controlled traffic farming – from worldwide research to adoption in Europe and its future prospects. In *Acta Technologica Agriculturae*, vol. 18, no. 3, pp. 64–73.
- CHEN, H. – WU, W. – LIU, X. – LI, H. 2010. Effect of wheel traffic on working resistance of agricultural machinery in field operation. In *Transactions of the Chinese Society of Agricultural Machinery*, vol. 41, no. 2, pp. 52–57.
- GALAMBOŠOVÁ, J. – MACÁK, M. – RATAJ, V. – ANTILLE, D. L. – GODWIN, R. J. – CHAMEN, W. C. T. – ŽITNÁK, M. – VITÁZKOVÁ, B. – ĎUŘÁK, J. – CHLPIK, J. 2017. Field evaluation of controlled traffic farming in Central Europe using commercially available machinery. In *Transactions of the ASABE*, vol. 60, no. 3, pp. 657–669.
- GALAMBOŠOVÁ, J. – MACÁK, M. – RATAJ, V. – BARÁT, M. – MISIEWICZ, P. 2020. Determining trafficked areas using soil electrical conductivity – a pilot study. In *Acta Technologica Agriculturae*, vol. 23, no. 1, pp. 1–6.
- GASSO, V. – SØRENSEN, C.A.G. – OUDSHOORN, F.W. 2013. Controlled traffic farming: A review of the environmental impacts. In *European Journal of Agronomy*, vol. 48, pp. 66–73.
- ISBISTER, B. – BLACKWELL, P. – RIETHMULLER, G. – DAVIES, S. – WHITLOCK, A. – NEALE, T. 2013. *Controlled Traffic Farming Technical Manual*. Department of Agriculture and Food, Western Australia. 78 pp.
- KUTKOV, G. 2014. *Tractors and Automobiles: the Theory and the Technological Properties*, Moscow, 506 pp. (In Russian: Tractory i avtomobili: teorija i tehnologicheskie svoistva).
- KINGWELL, R. – FUCHSBICHLER, A. 2011. The whole-farm benefits of controlled traffic farming: An Australian appraisal. In *Agricultural Systems*, vol. 104, no. 7, pp. 513–521.
- NADYKTO, V. – ARAK, M. – OLT, J. 2015. Theoretical research into the frictional slipping of wheel type undercarriage taking into account the limitation of their impact on the soil. In *Agronomy Research*, vol. 13, no. 1, pp. 148–157.
- NADYKTO, V.T. – VELYCHKO, O.V. 2015. Forecasting the development of energy ratio of agricultural tractors. In *Mechanization and Electrification of Agriculture*, vol. 1 (100), pp. 147–151.
- NADYKTO, V. – BULGAKOV, V. – KYURCHEV, S. – NESVIDOMIN, V. – IVANOV, S. – OLT, J. 2019. Theoretical background for increasing grip properties of wheeled tractors based on their rational ballasting. In *Agraarteadus*, vol. 30, no. 2, pp. 78–84.
- ONAL, I. 2012. Controlled traffic farming and wide span tractors. In *Agricultural Machinery Science*, vol. 8, no. 4, pp. 353–364.
- PANCHENKO, A. – KYURCHEV, V. 2008. A study of the draft and coupling qualities of wheeled tractors. In *Proceedings of the Tavria State Agrotechnological University*, vol. 8, no. 9, Melitopol, pp. 31–36. (In Ukrainian: Doslidzhennya tyahlovykh ta zchipnykh yakostey kolisnykh traktoriv).
- SIMIČIČ, M. – DEDOVIČ, N. – SAVIN, L. 2014. Power delivery efficiency of a wheeled tractor at oblique drawbar force. In *Soil and Tillage Research*, vol. 141, pp. 32–43.
- TULLBERG, J. – DIOGENES, L. A. – BLUETT, C. – EBERHARD, J. – SCHEER, C. 2018. Controlled traffic farming effects on soil emissions of nitrous oxide and methane. In *Soil and Tillage Research*, vol. 176, pp. 18–25.

